Free-Space Optical Communications for Resource-Limited Small Satellites

DOCTOR OF PHILOSOPHY DISSERTATION

Free-Space Optical Communications for Resource-Limited Small Satellites

資源に制約のある小型衛星における自由空間光通信に関する研究

ISHOLA, M. Femi
18595905

Supervised by
Prof. Mengu CHO

KYUSHU INSTITUTE OF TECHNOLOGY
Graduate School of Engineering
Department of Electrical & Space Systems Engineering
Laboratory of Lean Satellites Enterprises and
In-Orbit Experiments (LaSEINE)
Kitakyushu, Japan

September, 2021

Blank Page

THESIS INFORMATION

PhD Research Title:

"Free-Space Optical Communications for Resource-Limited Small Satellites"

資源に制約のある小型衛星における自由空間光通信に関する研究

Completed by:

ISHOLA, Mustapha Femi

Email: imfscience@gmail.com, ishola.mustapha-femi741@mail.kyutech.jp

Research Tenure:

October 1st 2018 to December 27th 2021

THESIS COMMITTEE:

1. Chair and Thesis Supervisor: Professor Mengu CHO
   Director, Laboratory of Lean Satellites and In-orbit Experiments, Kyushu Institute of Technology, Kitakyushu

2. Dr. Morio TOYOSHIMA
   Director-General, Wireless Networks Research Center, National Institute of Information and Communications Technology (NICT), Tokyo

3. Professor Asami KENICHI
   Faculty of Engineering, Kyushu Institute of Technology, Kitakyushu

4. Professor Kazuhiro TOYODA
   Faculty of Engineering, Kyushu Institute of Technology, Kitakyushu

ABSTRACT

Presently, the farthest CubeSats have gone into deep space was via a piggy-back ride to the orbit of planet Mars where a twin-6U CubeSats (MarCO-A & B) in formation provided X-band (8.425GHz) radio-frequency (RF) communication relay support between the Insight Lander spacecraft and the NASA Deep Space Network (DSN) receiving system on Earth at about 8Kbps data rate. Subsequent planned interplanetary CubeSat missions (such as the ESA Asteroid Impact and Deflection Assessment collaborative mission) seeks to leverage on and improve the capacity. The increasing demand for higher network bandwidth and system data-throughput has led to the utilization of higher frequency bands in the electromagnetic spectrum and increase in transmitter power for long range scenarios. Operating at higher frequencies (or shorter wavelengths) provides an expanded channel capacity and reduction in the transceiver components sizes comparable to the lower frequencies (VHF, UHF) counterparts. However, RF signals are highly susceptible to divergent spreading, atmospheric absorption and attenuation, severely limiting the communication system performance and efficiency. The RF spectrum is also fast becoming congested with severe signal interference problems especially in collocated and multi-node systems. On the contrary, the optical bands are currently underexplored, less regulated and without licensing complications.

Free-space laser communication represents a paradigm shift in modern high-rate data link and information processing capability enhancement. Laser signals have very high directivity, significantly increasing the transmitter's effective isotropic radiated power (EIRP) and improving the received signal to noise ratio in a long distance link such as direct deep-space satellite to ground communication system. Compactness of opto-electronic components is likewise attractive for very low-resource (size, weight and power) small satellite platforms, especially CubeSats. On the contrary, the suiting benefits of the narrow laser beamwidth simultaneously give rise to misalignment challenges, pointing and acquisition, tracking (PAT) problems, resulting to pointing errors between the communicating nodes. Platform disturbances and micro-vibrations from satellite onboard subsystems and deployable appendages also contribute to the laser signal pointing instability. A small satellite in deep space establishing an optical link with the ground will require a very strictly precise attitude determination and control system working together with a rapid response beam stabilization system having a high level of reliability and accuracy.

Lean or small (commonly used interchangeably) satellite philosophy is gaining prominence in defining the current and future architecture of space exploration missions. In recognition of this, the International Academy of Astronautics constituted a Study Group to define the industry standards and requirements of small satellites. The lean satellite approach seeks cheaper, quick development and delivery of small satellite missions, utilizing commercial-off-the-shelf components, smaller human resource and faster mission turn-around time. CubeSats are getting more roles and are consistently been considered for demanding tasks which were once the domain of traditional satellites. However, there exists a number of technology gaps that must be filled before the full potentials of CubeSat applications for very high throughput missions and deep space exploration can be fully harnessed. Gigabytes rate

communication transceivers, compact propulsion system, interplanetary guidance and navigation systems are a few of the current technological gaps. This research is focused on tackling the problems of laser communication adaptability on small satellites in considerable range with Earth-bound optical ground systems. To this end, the systematic design of an example theoretical mission described in this thesis adapts lean satellite initiative, use of COTS components and scalability.

A new approach of utilizing Photodiode Array (PDA) as an optical feedback sensor applicable to a MEMS Fine Steering Mirror (FSM) based laser beam fine pointing and control system is introduced in this thesis. Analyses and experiments demonstrated that the PDA have a much improved frame rate, eliminating the feedback delay experienced in the use of CCD cameras for laser beam position control. This presents a useful improvement in the performance of optical beacon tracking and fine pointing systems for laser communication modules in small satellites. Experiments on characterization of platform jitter spectrum and beam steering system mitigating the jitter effects in a 6U CubeSat platform is also presented in this thesis.

CubeSats and Unmanned Aerial Vehicles (UAV) are identical in terms of "leanness" or "scarcity" of onboard resources and are both considered as viable host platforms for laser communication devices in a ubiquitous optical communication regime. As a derivation of this research, the activities of the Japanese' National Institute of Information and Communications Technology, NICT-Kyutech collaboration on the development of a Drone 40Gbps lasercom fine pointing system is discussed. The Drone lasercom project sought to advance the state-of-the-art in UAV communication capabilities, with the agile optical coarse tracking, acquisition and fine pointing system playing a very critical role. In conclusion, the work done and reported in this thesis contributes to the advancement of free-space laser communication technology on small satellites in both near-Earth and deep space scenarios.

ACKNOWLEDGEMENTS

I wish to express my profound gratitude to my distinguished Supervisor, Professor Mengu Cho for his unreserved mentorship, guidance and high standard tutoring since the inception of my doctoral research. Thank you for your forthrightness and the wonderful recommendations which paved way for many opportunities I have enjoyed over the years. I sincerely appreciate the contributions of Professor Asami Kenichi. I am also very grateful to Professor Kazuhiro Toyoda for the many useful technical discussions and advice related to my experiments.

My utmost appreciation goes to Kyushu Institute of Technology Foundation and JASSO for the Monbukagakusho Honors Scholarship, selecting me as a beneficiary of the University scholarship fund since 2018. The tuition and monthly stipend scholarships were a great pillar of support for my finances. The scholarships allowed me to be laser-focused on my research. Part of the outcome of the dedication to work is the International Astronautical Federation (IAF) Emerging Space Leaders (ESL) Grant Award at Washington D.C., USA in 2019.

Sayo Tsukinari san, Shirakawa san, our amiable departmental Secretaries and Staffs have been quite helpful in organizing and managing the loads of documents, assisting with translations, scheduling, components purchases and deliveries. Ou san, Goto Toyomi san, Miwa Makino san and others at Daigakuin-kakari and Gakusei-kakari have been of immense support during the period of my research at the University. Keiko Matsuoka Sensei of the Kyutech Counselling Unit have been very selfless in her support to my family, especially my children. She took it upon herself to personally oversee and make sure that all medical, educational and recreational matters regarding my kids are well taken care of. She was present at the Kitakyushu Municipal Hospital child delivery room when our Son, Albert was born. She helped us with all translations, documents and countless tasks for my three kids. From immunization trips to Kindergarten enrolments, special programs and activities, Matsuoka Sensei was always there for us. Thank you for been an amazing angel!

I am greatly indebted to Dr. Morio Toyoshima, Director-General of the Wireless Networks Research Center, National Institute of Information and Communications Technology (NICT) for his benevolence and the great opportunities he facilitated to conduct research at the Space Communication Systems Laboratory through the NICT-Kyutech Drone Lasercom collaboration project. Very special thanks to Dr. Tetsuharu Fuse, Yasushi Munemasa, Alberto Carrasco, Trinh Phuc, Hideaki Kotake and other wonderful research staffs at NICT. To my friends and colleagues at Cho Lab; Muto Noruji (my very close ally), Eyoas, Hari, Ramson and many others, I say thank you!

I dedicate this thesis to my wife, Mrs. Ishola Christiana Dolapo and my wonderful children; Ishola Akinola Alexander, Ishola Adunola Angelina and Ishola Ayoola Albert. These gentle souls have been the source of my happiness, they inspired and motivated me in difficult times, and they energize me and project an assured hope of a blissful, greater future. Thank you for been there with me through the thick and thin experiences. To my parents, Chief Adekunle Ishola Ekemode and Mrs. Ishola Tawakalitu Kuku, thanks for all your care.

I am indeed very grateful for all the love and support provided by these individuals and organizations. Thank you for been a meaningful part of my success journey!

PUBLICATIONS

Some portion of this thesis are extracts from the following publications made by the thesis author during the period of this research:

- "Feasibility Analysis of Optical Communication System for a Moon Orbiting Cubesat and Earth Station"
  70th International Astronautical Congress, Washington D.C, USA.
  (2019年 10月)
  著者 F. Ishola and M. Cho

- "Experimental Study on Photodiode Array Sensor Aided MEMS Fine Steering Mirror Control for Laser Communication Platforms"
  IEEE Access Journal, vol. 9, 頁 100197-100207
  (2021年 7月)
  https://doi.org/10.1109/ACCESS.2021.3096816
  著者 F. Ishola and M. Cho

TABLE OF CONTENT

LIST OF FIGURES

LIST OF TABLES

NOMENCLATURE

SYMBOL	DESCRIPTION	Units
P_r	Total Received Laser Power	Watts, dB
P_t	Total Transmitted Laser Power	Watts, dB
G_t	Transmitter Telescope Gain	dB
G_r	Receiver Telescope Gain	dB
η_{to}	Transmitter Optics Efficiency	-
η_{ta}	Transmitter Aperture Illumination Efficiency	-
η_{ro}	Receiver Optics Collecting Efficiency	-
η_{Ω}	Spatial Filtering Efficiency at the Receiver	-
L_{tp}	Transmitter Pointing Loss	dB
L_{atm}	Atmospheric Absorption Loss	dB
L_{rp}	Receiver Pointing Loss	dB
L_{sp}	Free Space Loss	dB
EIRP	Effective Isotropic Radiated Optical Power	-
R	Link Distance	Meters (m)
λ	Laser Diode Operating Wavelength	Meters (m)
D_t	Transmitter Telescope Diameter	Meters (m)
a	Transmitter Telescope Main Aperture Radius	Meters (m)
b	Transmitter Telescope Obscuration Radius	Meters (m)
γ_t	Transmitter Telescope Obscuration Ratio	-
r	Receiver Telescope Radius	Meters (m)
γ	Receiver Telescope Obscuration Ratio	-
α_t	Transmitter Telescope Truncation Ratio	-
k	Boltzmann's Constant	Joules/Kelvin
T	System Noise Temperature	Kelvins
ϑ, ω	Beam width	rad

ϕ	Beam Divergence Angle	rad
d_f	Far Field Beam Footprint Diameter	Meters (m)
S	Strehl Ratio	-
σ^2	Wave Front Error (WFE) or Wave Front Variance	rad^2
r_0^*	Atmospheric Turbulence Strength or Fried Parameter	-
θ_e	Pointing Error	
PIF	Pointing Induced Fade	
$p(\theta_e)$	Rice Density (Probability Distribution Function for Pointing Errors)	
R_b	Data Rate	Bits/Sec (bps)
T_s	Slot Width	Seconds (s)
P_{pk}	Maximum Number of Detected Signal Photons Per Pulse	-
P_n	Noise Power	Watts, dB
P_{av}	Average Number of Detected Signal Photons Per Slot	-
λ_b	Average Number of Noise Photons Incident Per Second	-
n_b	Average Number of Detected Noise Photons Per Slot	-
n_s	Mean Number of Signal Photons Per Slot	-
E_P	Pulse Energy	Joules
PRF	Pulse Repetition Frequency	Hz
BER	Bit Error Rate	-
SER	Symbol Error Rate	-
M	Pulse Position Modulation Order	-
C(M)	Channel Capacity of M-ary Pulse Position Modulation	Bits/Seconds
SNR	Signal-to-Noise Ratio	-
η_{qd}	Quantum Efficiency of the Receiving Detector	-

R_{PPM}	Error-Control Code Rate for Pulse Position Modulation	-
R_{OOK}	Error-Control Code Rate for On-Off-Keying Modulation	-
d_t	Dead Time	Seconds
h(p)	Entropy Function	-
I_s	Optical Signal Irradiance	Watts/m^2
I_n	Optical Noise Irradiance in Receiver Aperture Plane	Watts/m^2
I_b	Background Sky Radiance	Watts/$m^2\ sr\ \mu m$
Ω	Detector Field of View	
Δ_λ	Bandwidth of Narrowband Spectral Filter	Hz
ε	Energy per Photon	Joules
h	Planck's constant $6.62607004 \times 10^{-34}$	$m^2 kg/s$
c	Speed of Light 3×10^8	m/s

ABBREVIATIONS

1U, 2U, 3U, 6U	1-Unit, 2-Units, 3-Units, 6-Units
3D	Three Dimension

A

ADCS	Attitude Determination and Control System
ADC	Analog to Digital Converter
APD	Avalanche Photodiode

B

BER	Bit Error Rate
BOL	Beginning of Life
BGA	Ball Grid Array
BERT	Bit Error Rate Tester

C

CAD	Computer Aided Design
CMD	Command
CMOS	Complementary Metallic Oxide Semiconductor
CMG	Control Moment Gyro
COTS	Commercial-off-the-shelf
CCD	Charge Coupled Devices

D

DAC	Digital to Analog Converter
DoD	Depth of Discharge
DC	Direct Current
DRM	Design Reference Mission
DSoN	Deep Space Optical Network
DWDM	Densed Wavelength Division Multiplexing

E

EMC	Electromagnetic Compatibility
EDFA	Erbium-Doped Fiber Amplifier
ESD	Electrostatic Discharge
EQM	Engineering Qualification Model
EPS	Electrical Power Subsystem
ESL	Emerging Space Leader
ETS	Engineering Test Satellite
EOL	End of Life

EIRP	Effective Isotropic Radiated Power

F

FSM	Fine Steering Mirror
FSL	Free Space Loss
FM	Flight Model
FSK	Frequency Shift Keying
FSO	Free Space Optical Communication
FPS	Fine Pointing System
FPA	Focal Plane Array
FITSAT	Fukuoka Institute of Technology Satellite
FWHM	Full Width at Half Maximum

G

GS	Ground Station
GSE	Ground Support Equipment
GEO	Geosynchronous Orbit
GPS	Global Positioning System

H

HPBW	Half Power Beamwidth

I

I/O	Input/output
IoT	Internet of Things
I2C	Inter-Integrated Circuit Protocol
ISS	International Space Station
ITU	International Telecommunication Union
IAF	International Astronautical Federation
IMU	Inertia Measurement Unit

K

Kyutech	Kyushu Institute of Technology

L

LaSEINE	Laboratory of Lean Satellite Enterprises and In-Orbit Experiments
LEO	Low Earth Orbit
LED	Light Emitting Diode
LDR	Light Dependent Resistor
Lasercom	Laser Communication
LRO	Lunar Reconnaissance Orbiter

LLCD	Lunar Laser Communication Demonstration
LADEE	Lunar Atmospheric and Dust Environment Explorer
LCRD	Laser Communication Relay Demonstration

M

MEMS	Microelectromechanical System
MOSFET	Metallic Oxide Semiconductor Field Effect Transistor
MODTRAN	Moderate Resolution Atmospheric Transmission Code
METARs	Meteorological Aerodrome Reports
MMF	Multi-Mode Fiber

N

NASA	National Aeronautics and Space Administration
NICT	National Institute of Information and Communications Technology
NEP	Noise Equivalent Power
NOAA	National Oceanic and Atmospheric Administration

O

OBC	On-board Computer
OM	Optical Module
OCSD	Optical Communication and Sensors Demonstration
O2O	Optical to Orion
OGS	Optical Ground Station

P

PAT	Pointing Acquisition and Tracking
PCB	Printed Circuit Board
PDR	Preliminary Design Review
PPM	Pulse Position Modulation
PRBS	Pseudo Random Binary Sequence
PSU	Power Supply Unit
PIN Photodiode	Positive-Intrinsic-Negative Doped Photodiode
PSD	Position Sensitive Devices
PDA	Photodiode Array

Q

QoS	Quality of Service
QD	Quadrant Photodetector

R

RF	Radio Frequency
RTC	Real Time Clock

RWA	Reaction Wheel Assembly

S

SMA	Subminiature Version A Connector
SMD	Surface Mount Devices
SOP	Standard Operating Procedures
SPI	Serial Peripheral Interface
SNR	Signal to Noise Ratio
SWaP	Size, Weight and Power
SOTA	Small Optical Transponder
SFP+	Small Form-Factor Pluggable Plus Transceiver

T

TBD	To be determined
TI	Texas Instruments
TTL	Transistor-Transistor Logic
TT&C	Telemetry, Tracking & Command
TBIRD	Terabyte Infrared Delivery
TSP	Tracking Solar Panel

U

UAV	Unmanned Aerial Vehicle
UART	Universal Asynchronous Receiver-Transmitter
UHF	Ultra-High Frequency
USB	Universal Serial Bus

V

VHF	Very High Frequency
VSOTA	Very Small Optical Transponder

1. INTRODUCTION

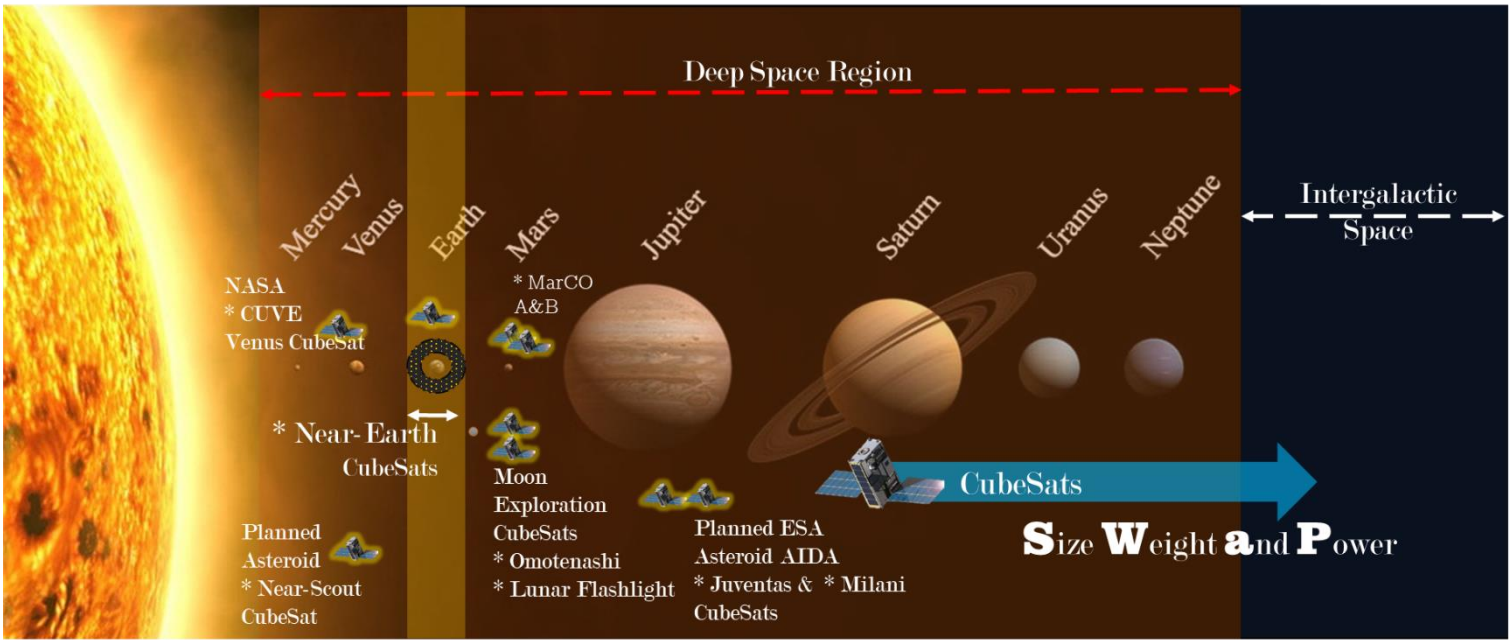

Figure 1-1: Deep Space Exploration with CubeSats

Short and Long distance communication is a vital part of human activity and societal operation. Ancient civilizations in Egypt, China, and Greece utilized a number of rudimentary means for exchange of information such as drumbeats, lighthouses, smoke signals, animal-carriage mail carts and many more [1]. Electrical wire telegraphy and Morse code system came to limelight in the 18th century, transforming the manner and speed of information exchange. The era of wired telegraph witnessed lots of innovation that sought to expand the volume of information that can be sent and received via cable networks. An even more radical development started in 1895 when the Italian inventor, Gugleilmo Marconi demonstrated the practicability of wireless telegraphy [2][3][4]. Since then, radio frequency communications has become the mainstream mode of short and long distance connectivity. Modern terrestrial-based mobile telephony systems such as 5G networks, space communication and data relay networks are all based on radio frequency waves conveying information between different nodes. Nowadays, many systems and devices contend for the same frequency use, leading to strict licensing procedures and costs. Geostationary satellites orbital positions and frequency use are tightly managed and heavily regulated. The radio frequency channel is rapidly getting congested and its capacity now approaching the critical limits [5][6]. The new era of big-data, internet of things (IoT) and growing information burst between multiple devices and platforms also poses new challenges to RF-based communication networks [7].

Optical fiber technology demonstrated the potentials of light-based communication systems, providing crucial broadband connectivity backhaul between cities and continents. However, cable transmission mediums (whether wire conductors or optical fiber) are severely limited and disadvantageous in very long range communication scenarios, especially when the communicating nodes are non-stationary. This underscores the importance of free-space optical communication technology in satellite, airborne, maritime and tactical ground systems.

Over the years, there has been a rapid increase in adoption and launch of small satellites. Particularly, CubeSats are attractive because of its low production cost, lightweight and risk tolerance. Manufacturing time is extremely short compared to bigger satellites, flexible, adaptable to most near-Earth mission and vast possess potentials. Current applications of CubeSat is quite diverse: Communications, navigation, earth/planetary observations, remote sensing and scientific missions. CubeSats constellations and crosslinks have also been considered for substantial commercial missions such as the SpaceX StarLink constellation [8].

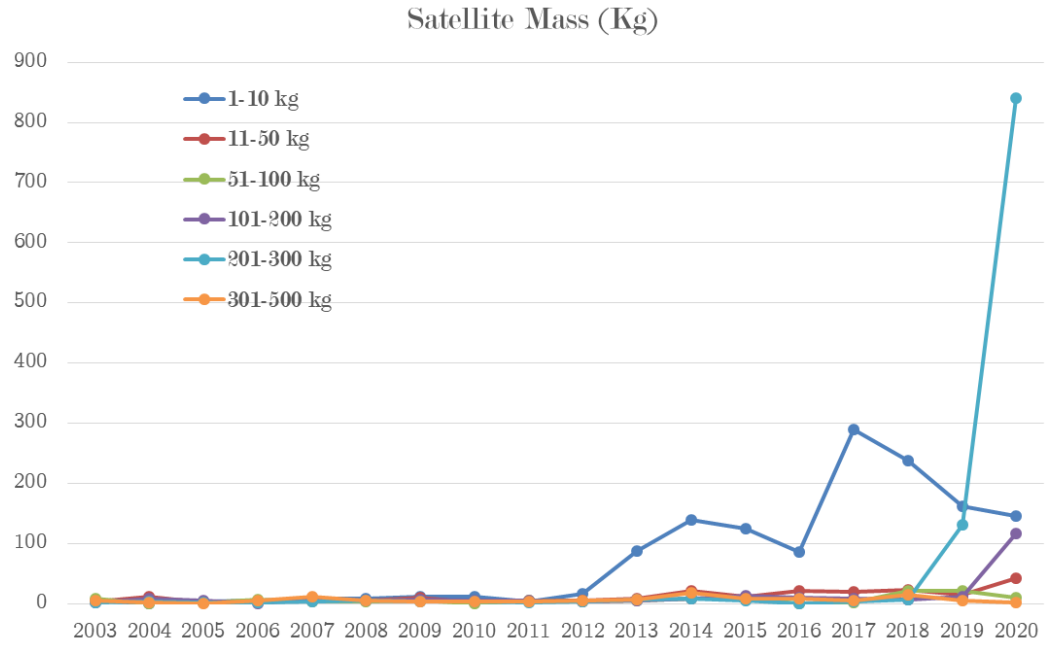

Figure 1-2: Increase in Small Satellite Launches [9].

Table 1-1: Top Data Rate CubeSats

CubeSats	*Size*	*Data Rate (Mbps)*	*Frequency (GHz)*	*Transmitter (Watts)*	*Link Range (km)*
Flock-3P	3U	200	5	1	400
Dove Pioneer	3U	200	8.22	1	280
AeroCube-7A	1.5U	40	300	6	800
Corvus-BC	6U	37	26.8	0.75	600
DemoSat-2	3U	8	2.39	3	500
MarCo A&B	6U	0.008	8.45	4	1.5e8

Nowadays, Ka and X-band communication systems are now integrated into CubeSats due to the demand of a faster link and increased data throughput [10][11][12] [13].

Table 1-2: Achievable CubeSat Ka-Band Data Rates.
The information in this table is taken from [8]

Ground Antenna	*LEO Data Rate QPSK*	*LEO Data Rate DVB-S2*	*Lunar Data Rate*

ASF 1.2m	477.5 kbps	16.943 Mbps	-
ASF 2.4m	1.574 Mbps	55.847 Mbps	-
ASF 5.4m	4.3 Mbps	153.4 Mbps	10.6 kbps
ASF 7.3m	6.6 Mbps	233.2 Mbps	16.1 kbps
ASF 11m	25.2 Mbps	892.9 Mbps	61.5 kbps
WSC 18m	257.5 Mbps	1.125 Gbps	629.5 kbps

1.1. Research Motivation

This research is focused on addressing the communication problem of small satellites in enormous (several millions of kilometers) range with Earth-bound ground systems. The problem is that as communication range increases, the free space path loss (attenuation) of electromagnetic signals becomes significant enough to limit the efficiency of the system. Often times, higher transmitter power and larger antennas are required to work around the signal-to-noise ratio (SNR) problem but this is a fundamental challenge for CubeSats given the limited power generation and small size of the platform. The wavelength of Radio Frequency (RF) transmissions is also responsible for the narrow channel bandwidth and scanty data rates at huge distances. In general, the effective isotropic radiated power (indicative of the transmission energy and directivity), SNR, data capacity and link range becomes very important parameters that determines the performance metric of a reliable satellite communication system.

Free space optical communications, involves the use of highly focused/high directivity, short-wavelength Lasers, and represents a breakthrough technology in overcoming the limits of RF communication systems. Optical communications offers the possibility to use lightweight, low power consumption optoelectronics components to make up high performance transceiver module that can be easily hosted on small satellites. Very high beam directivity translates to an increase in platform pointing requirement. In deep space cases, the attitude control accuracy of current ADCS units may be inadequate in sufficiently aligning the satellite lasercom optics to the field of view of the target receiver. Coarse tracking, link acquisition system and accurate fine pointing system for augmenting the limitation of the satellite attitude control becomes very essential.

1.2. Research Objectives

Platform pointing system capability is an important parameter of a satellite optical link budget and design. A satellite with a highly capable beam pointing doesn't necessarily require high transmitting power and can also easily support the use of smaller aperture optical ground receiving telescope. The chief purpose of this research is to improve the efficiency of coarse and fine pointing subsystem of a CubeSat Lasercom unit with the perspective of significantly reducing the resource demands and counts of optoelectronics devices required on the host platform. CubeSats are plagued by scare platform resources: available space/size, limited weight and power generation (SWaP). Broadly, the objective of this research is to develop

innovative techniques and systems development essential to foster the adaptability of laser communication transceivers on small satellites with improved performance and data throughput than comparable satellites utilizing RF communication systems. The following are the highlights of the main areas of focus:

i. Theoretical analysis and optical link budget estimation for a Lunar optical communicating CubeSat
ii. Feasibility analysis of deep space Lasercom using 6U CubeSat
iii. End-to-end system design/architecture and key components identification
iv. Lasercom Fine Pointing System (FPS) and beam steering laboratory experiments involving implementation of a feedback control for optical fine pointing system and utilizing COTS inertia and photodiode array sensors
v. CubeSat platform jitter characterization and mitigation for Lasercom
vi. Pointing, acquisition and tracking (PAT) System development for CubeSat and Drone Lasercom: NICT-Kyutech Collaboration Project

1.3. Novelty of Thesis

This thesis introduces a new mission scenario and study of a lunar orbiting CubeSat establishing direct-to-Earth laser communication link. As at the time of this thesis, there is no actual CubeSat orbiting the Moon and the planned lunar exploration missions such as Lunar Flashlight, Omotenashi and others do not contain a direct to Earth optical communication downlink as part of the mission or platform requirement. This thesis studies and confirms the feasibility of the use of CubeSat lasercom terminal in deep space and delivery of two order of magnitude increase in throughput compared to Ka or X-band counterparts.

A new optical sensor feedback approach utilizing Photodiode Array in lasercom fine pointing and control system is also presented for the first time. The PDA is a COTS device that offers the advantage of increased signal-to-noise ratio, wider field-of-view compared to commonly used components such as segmented quad detectors and lateral-effect position sensitive devices. The PDA supports significantly higher frame rate and read-out speed unlike the slow and bulky CCD cameras used in Fine Pointing Systems. The higher frame rate makes it possible to implement an active and adaptive fine steering mirror based beam position control with larger bandwidth sufficient to capture the spectrum of platform jitter or micro-vibrations generated by the reaction wheel assembly. Cost-wise and also considering the onboard computing requirements, the PDA is a much better alternative to the CCD camera option.

Nowadays, several CubeSat vendors offers complete COTS CubeSat platforms featuring compatible subsystems. In such cases, the customer is only bothered by the payload electrical and structural interface as well as integration and general system interoperability. Merely predicting the jitter model of a CubeSat platform based on a prior mission can easily turn out to be an inaccurate gamble with adverse consequences on the mission outcome. This is even more critical especially when it is hosting a laser communication terminal and imaging payloads. This thesis carried out experimental measurements of actual reaction wheel micro-vibrations and its force propagation effects on near optical instrument. These measurements

included actual optical pointing perturbations as well as jitter acceleration data generated by the reaction wheel assembly.

The NICT-Kyutech Drone-to-Ground lasercom collaboration project is the world's first UAV direct to ground link at optical C-band and 40Gbps data rate. The fine pointing system critical to the system operation is a constituent part of this thesis. The system features single mode fiber coupling using Mode-Demux at the ground station, wavelength-division-multiplexing (WDM) technique and low Bit Error Rate at 10^{-6} without forward error correction.

1.4. Thesis Organization

Chapter Two dives into the history of satellite optical communication developments, state-of-art in deep space communications and literature review on important aspects of laser communications (Lasercom) such as link design, signal modulation, coding, coarse and fine pointing systems, acquisition and tracking systems, propagation effects on beams through space environment and Earth atmosphere (turbulence, absorption, scintillation and weather induced attenuation), optical ground telescope systems, adaptive optics, photodetectors etc.

In Chapter Three, an analytical design reference mission, LaSEINE-Lunar is presented. It examines the mission scenario, hardware configurations and link analysis of a hypothetical 6U CubeSat hosting an imaging payload and 250Mbps downlink Lasercom transceiver transmitting from Moon's orbit to a compact 40cm optical ground telescope on Earth. Systematic design considerations identifying key components and link outage probability estimation during different atmospheric and weather conditions are also presented.

Chapter Four describes a new approach unique to this research, to improve the performance of laser beam feedback control system which is an essential part of a microelectromechanical (MEMS) Fine Steering Mirror (FSM) based Lasercom fine pointing system (FPS). A photodiode Array (PDA) is introduced as an optical feedback sensor in the place of CCD cameras and Position Sensitive Devices (PSD). Furthermore, the chapter describes an experimental beam steering test system designed to evaluate the performance of the PDA. The PDA offered higher speed laser beam centroid tracking than CCD cameras despite having fewer pixels count. CCD cameras are generally slow with meagre frame rates, severely limiting the operational bandwidths of line-of-sight lasercom FPS. Additional merit of the PDA is the higher field-of-regard compared to segmented Quadrant Detectors and lateral effect PSDs, reducing the optics count required in typical applications. This is a desirable advantage in CubeSats were size and weight are tightly managed and distributed. The system developed in this research is the first to utilize a PDA as a feedback device in automatic laser beam steering and control system. The PDA system is applicable for beacon tracking and overall FPS system development for a deep space bound CubeSat.

CubeSat platform jitter problems and resultant impact on Lasercom beam pointing stability are covered in Chapter Five. Analysis of CubeSat micro-vibrations generated by reaction wheel static and dynamic imbalances is presented. The chapter also illustrates laboratory experiments to measure the CubeSat jitter spectrum induced by COTS attitude

determination and Control System (ADCS) three-axis reaction wheel as well as active fine pointing control mitigation strategy.

Chapter Six describes the 40Gbps laser communication fine pointing system development for a hexacopter Drone, a collaboration project between Kyushu Institute of Technology (Kyutech) and the National Institute of Information and Communications Technology (NICT). Small satellites and airborne platforms such as a Drone share similar platform characteristic challenges. Hence, the development of workable system on the Drone can be easily translated to CubeSats. The activities of the collaboration project, an integral part of this thesis research is presented in Chapter Six.

Finally, Chapter Seven is dedicated for concluding remarks and presents recommendations for future work. Optical communication system adaptability is an essential enabler for CubeSat to thrive in deep space missions with order of magnitude increase in data throughput and satisfactory performance. Management of satellite onboard resources, end-to-end system design, mitigation of beam pointing challenges, subsystems performance optimization as presented in this thesis are cardinal to technology readiness level improvement of small satellites in deep space optical communications revolution.

2. BACKGROUND AND LITERATURE REVIEW

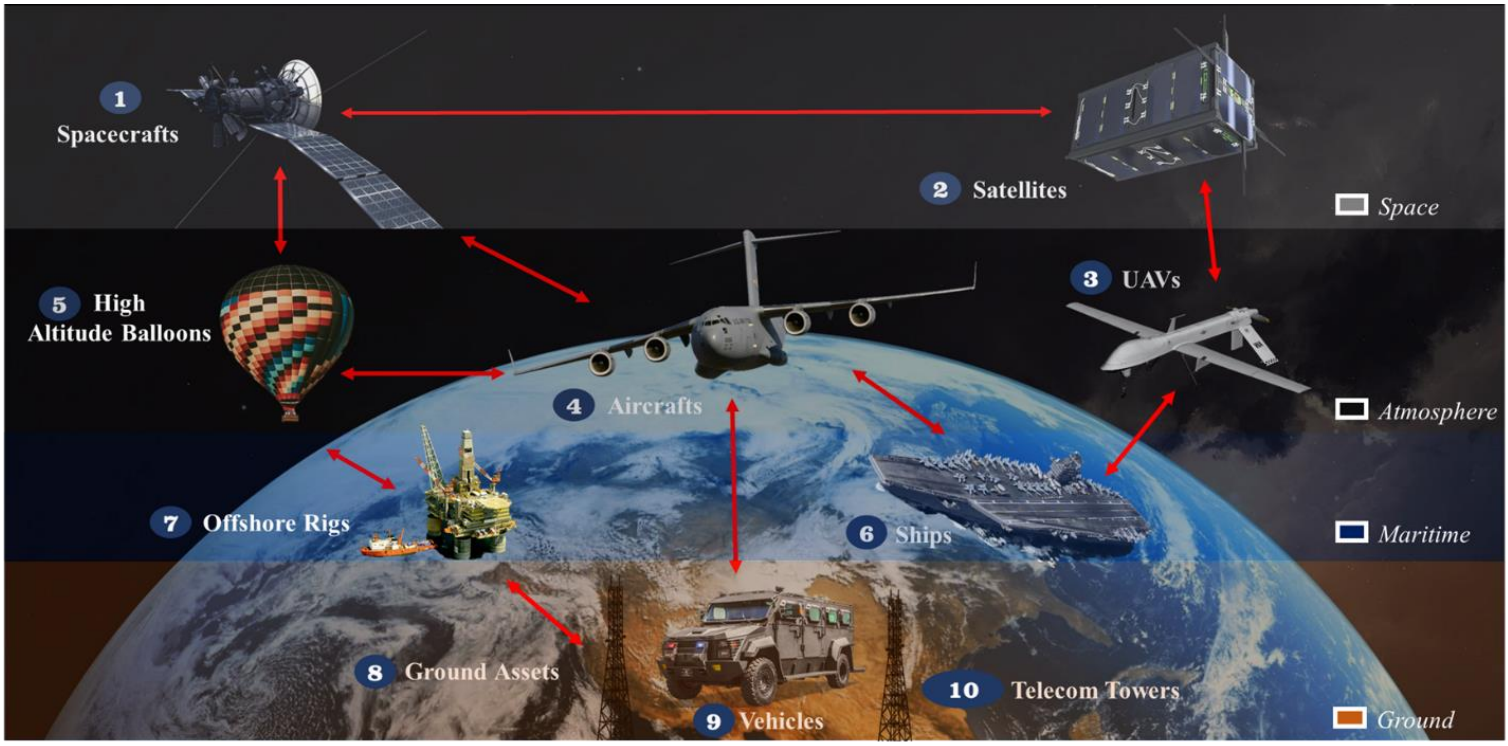

Figure 2-1: Diverse Lasercom Scenarios.

This Chapter presents the historical context of optical communication development, lean or small satellite philosophy and theoretical background of free-space optical communication.

2.1. History of Satellite Optical Communications

2.1.1. Early and Current Japanese Missions

Japan has a pioneering history of satellite optical communication technology developments. The Japanese ETS-VI (KIKU-6) [14] was the first ever satellite (2,660kg) in the world to demonstrate a space to ground laser downlink with the Laser Communication Equipment (LCE) from GEO, launched in 1994 [15]. As a result of the satellite orbital insertion circumstances and an optimal ground station linkage, Japan collaborated with NASA JPL to utilize the Table Mountain Facility, California for the Ground Orbiter Lasercom Demonstration (GOLD) Experiment [16]. Thereafter, JAXA and NICT developed the Optical Inter-orbit Communication Engineering Test Satellite (OICETS-KIRARI) which hosted the Laser Utilizing Communications Equipment (LUCE), launched in 2005 to LEO [17][18][19]. KIRARI mission featured inter-satellite optical link demonstration with the ESA ARTEMIS satellite in GEO as well as direct to ground experiment to different ground stations [20][21]. The Fukuoka Institute of Technology deployed FITSAT-1 (Nikawa) a 1-U Cubesat via ISS robotic arm in 2012 [22, p. 1]. The satellite employed LEDs array transmitter to transmit Morse-code signal to the ground. NICT also flew and demonstrated the world's smallest

Quantum Key Distribution communication transmitter "Small Optical Transponder (SOTA)'' payload [18][23][24] mounted on SOCRATES (Space Optical Communications Research Advanced Technology Satellite) a 50kg class small satellite in 2014, achieving up to 10Mbps from LEO (at about 1000km altitude) [25]. NICT continued successful demonstration of a space to ground link using the 'Very Small Optical Transponder' (VSOTA) a smaller version of SOTA hosted on RISESat [26][27][28][29]. In 2019, JAXA, NICT and Sony Corporation jointly developed the Small Optical Link for International Space Station (SOLISS) equipment which was installed on the International Space Station (ISS) exposed Japanese Experiment Module (JEM-Kibo). In 2020, a bidirectional Ethernet laser communication link was demonstrated between the ISS and NICT optical ground station in Koganei, Tokyo transmitting high-definition image [30][31][32]. Currently, NICT is developing the 10Gbps space laser communication GEO-based Engineering Test Satellite ETS-IX (HICALI) [33] and CubeSOTA, a 3-U CubeSat hosting a miniaturized laser communication terminal [34].

2.1.2. NASA Laser Communication Missions

The Lunar Laser Communication Demonstration (LLCD) mission presented an optical payload flown on NASA' Lunar Atmospheric and Dust Environment Explorer (LADEE) spacecraft. A data rate of 622 megabits per seconds direct-to-Earth downlink was established in 2013 from Moon's orbit (400,000km). This represented a major milestone achievement in direct deep-space laser links and gradual transition of space-based communications to the optical spectrum and a future Deep Space Optical Network (DSoN) [35][36][37].The optical payload mass was 30.7kg, and comparably consuming about three-quarter of power required by the Lunar Reconnaissance Orbiter (LRO) [38], LLCD demonstrated outstanding performance over the LRO which delivers only 100 megabits per seconds at Ka-band [39].The LADEE spacecraft (383kg) is regarded in the same category as small satellites (≤500kg) [40], opening up the potentials of adapting optical communication payloads on resource-limited micro-satellite platforms such as CubeSats [41].

In 2014, NASA demonstrated an optical communication downlink from the OPALS (Optical Payload for Lasercom Science) terminal hosted on the International Space Station. OPALS payload weighed 159kg and delivered 50Mbps data rate [42].

NASA is planning to launch the "Laser Communications Relay Demonstration (LCRD)" mission with a target of 1.22Gbps transmission rate, in 2021. The "ILLUMA-T (Integrated LCRD LEO User Modem and Amplifier Terminal)" to be flown on ISS is being developed by NASA and the MIT Lincoln Laboratory. The "O2O (Optical to Orion)" planned as an advanced optical communication system to support manned deep space exploration.

NASA is also planning a deep space optical communication system for the "Psyche Mission Spacecraft" aimed at Mars flyby and Asteroid landing in 2026. NASA's Optical Communication and Sensors Demonstration (OCSD) program featured two 1.5U, 2.3kg Cubesats AeroCube-OCSD-B and C, establishing 200megabits per second downlink from Low Earth Orbit (LEO) [43][44][45][46][47][48][49].

2.1.3. European Laser Communication Missions

Optical communications activities in Europe started in 2001 with the SILEX experiment (Semiconductor Laser Inter-Satellite Experiment) [50][51] between the ARTEMIS and SPOT-4 satellite [52]. Demonstration of LEO-to-LEO 5.625Gbps bidirectional intersatellite optical communication was carried out between the TerraSAR-X and NFIRE (Near Field InfraRed Experiment) satellites in 2008 [53][54]. The world's first LEO to GEO optical communication links were accomplished by the Copernicus Sentinel-1A and Sentinel-2A Earth Observation satellites [55]. The European Data Relay System (EDRS) nodes (EDRS-A on EutelSat-9B satellite and EDRS-C on OHB Hylas-3 satellite) featuring laser communications terminal based in GEO were designed to provide LEO to GEO to Earth mission data feeder links [56]. AlphaSat (Inmarsat-4A F4) operated by Inmarsat and ESA launched to GEO in 2013, featuring an optical communication payload as part of the EDRS [57]. An intersatellite laser link was demonstrated between Sentinel-1A in LEO and AlphaSat in 2014. The DLR OSIRIS (Optical Space Infrared Downlink System) optical communication roadmap program consists of a series of four small satellites hosting laser communication terminals program [58]. The first was OSIRISv1 Flying Laptop [59] followed by BiROS (OSIRISv2) and the recently launched PIX-L (OSIRISv4) a 3U CubeSat hosting a very small and compact laser terminal (CubeLCT).

2.2. Trends with Small Satellites

The lean Satellite philosophy stipulates the adaptation of the following clauses throughout the development and mission life cycle of a small satellite or CubeSat: implementation of active safety measures, debris mitigation, compliance with radio frequency usage, UN registration, compliance with launcher interface control documentation (ISO-17689:2015), rigorous space qualification and acceptance testing (ISO-19683:2017) and conformity with the ISO-17770:2017 quality assurance metrics. Satellite owners and mission project managers adopting this philosophy also must take into account means of significant reduction of satellite mission cost, faster platform manufacturing and delivery time, platform simplicity, risk tolerance and mitigation, moderate to high reliability levels (considering the performance of COTS components), seamless launch operations and waste minimization (this further includes: transportation, efficient personnel communication channels, direct physical interactions and proximity or collocation of production activities) [60].

The proliferation of CubeSats is accelerating and there has been intensified research, development efforts and numerous space missions (by space agencies, private companies, educational institutions etc.) utilizing the benefits of the platform. There has also been an increasing proposal for the use of CubeSats for technology demonstrations and deep-space missions particularly the Moon as an immediate destination. NASA's Cubesat launch initiative for Artemis spaceflight program is providing opportunities for 13 lunar bound Cubesat missions as secondary payloads on the planned second flight of the unmanned Orion vehicle to be launched by the first flight of the Space Launch System (SLS) super heavy rocket in 2020. Table 2-1 below provides a brief overview of some of the planned missions [61]. The 2020 NASA State of the Art Report of Small Spacecraft Technology [62] [63] listed the current Technology

Readiness Level (TRL) of Small Satellites Lasercom technology in some missions between level 5 and 7. The DLR OSIRIS4 3U CubeSat launched recently was designed to deliver 100Mbps laser link from LEO [64]. The NASA's planned TeraByte InfraRed Delivery (TBIRD) 6U CubeSat program will host a 2U-size Lasercom payload delivering up to 200Gbps direct downlink from LEO [65][66]. The SpaceX StarLink constellation of 260kg-class small satellites features inter-satellite laser communication link at 2.5Gbps and 5000km range, each satellite hosting five laser transponders to pair with other satellites in it neighborhood [67]. As depicted in the illustration below, the historical trend of optical communication terminals development has been characterized by continuous reduction in size and weight but with consistent increase in data throughput capacity, similar to the Moore's law effect in computers.

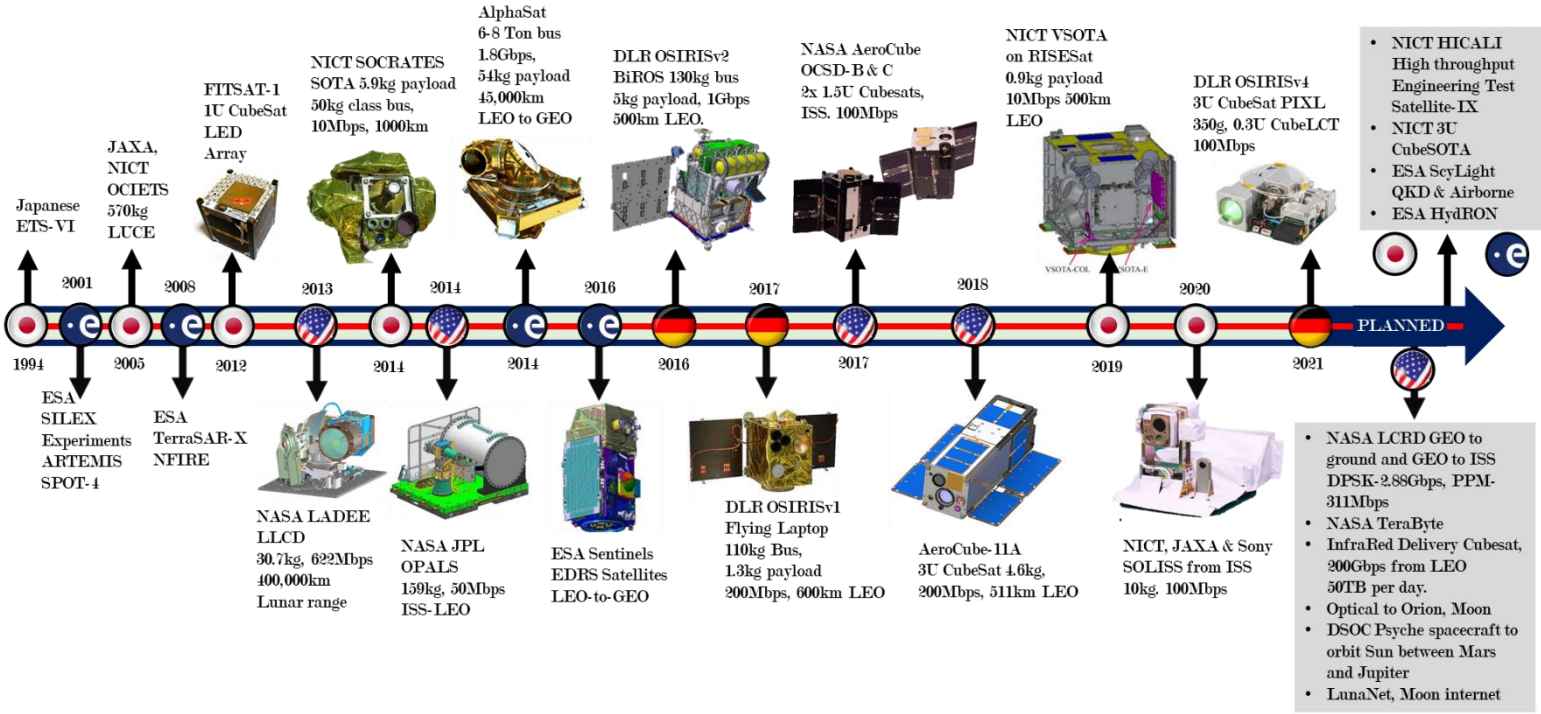

Figure 2-2: Historical trends of satellite optical communication developments. (Sub-images credits [68, p. 1][69][70][71][72][73][74][75])

As part of the Artemis program, NASA has outlined plans to work with several stakeholders to fly a number of CubeSats on a piggy back ride on the Orion spacecraft to be launched by the Space Launch System (SLS) into deep space [76]. The CubeSats communication aspect adopts the JPL developed Iris deep-space transponder, designed to operate with the Deep Space Network at X-band frequencies (7.2GHz uplink and 8.4GHz downlink), 3.8W transmitter RF power and 8kbps data rates [77]. None of these CubeSats features an optical communication link either with a mother spacecraft or direct-to-Earth transmission.

Table 2-1: Some of the planned Cubesat Moon missions

Cubesat	*Platform*	*Mission*

Lunar IceCube	6U, X-band	Prospect for water in solid, liquid, and vapor forms and other lunar volatiles.
Lunar Flashlight	6U, X-band	Detect and map lunar surface ice in permanently shadowed regions of the lunar south pole. Link 34m Deep Space Network
LunaH-Map	6U, X-band, 500kbps	Map hydrogen within craters and other permanently shadowed regions throughout the moon's south pole.
Cislunar Explorer	6U, X-band	Pair of self-propelled engineering demonstrations, proving tech of water as rocket fuel and simple optical navigation
JAXA Omotenashi	6U, 14kg, X-band	Outstanding moon exploration technologies demonstrated by nano semi-hard impactor lander.
BioSentinel	6U, 14kg, X-band	Measurement of deep space radiation effects on DNA using yeast organisms
NEA Scout	6U, 14kg, X-band	Near-Earth Asteroid Scout. Demonstration of solar sail deployment and a near Earth Asteroid flyby

2.3. Free Space Optical Communication Link Analysis

2.3.1. Transmitter Gain and Beam Divergence

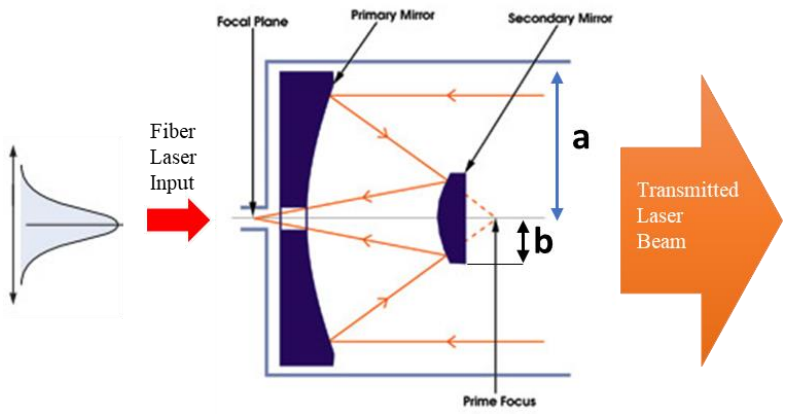

Figure 2-3: Cassegrainian Transmitter Telescope

Laser communication is advantageous mainly because of the large bandwidth, narrow beamwidth and high directivity of the beam and hence very high transmitter gain, playing a significant role in boosting the link margin in a long range communication scenario. Considering an optical fiber laser source coupled with a Cassegrainian telescope as illustrated

above, the incident source function $E_0(r_0)$ at the transmitter aperture is modeled as a Gaussian amplitude function:

$$E_0(r_0)=\sqrt{\frac{2}{\pi\omega^2}}\times\left\{e^{-\left(\frac{r_0^2}{\omega^2}\right)}\right\}\times\left\{e^{\left(\frac{jkr_0^2}{2R_c}\right)}\right\} \tag{2-1}$$

R_c is the radius of curvature of the phase front at the aperture. The transmitted laser beam has a beam width is denoted as , measured from the telescope axis to the $\frac{1}{e^2}$ point. The outgoing power over the aperture plane of the transmitter can be expressed as:

$$P=\int_0^{2\pi}\int_0^{\infty}|E_0(r_0)|^2 r_0\,dr_0\,d\emptyset_0 \tag{2-2}$$

The intensity at an observation reference point$(r_1,\ \theta_1)$ in a cylindrical coordinate is given by:

$$I(r_1,\ \vartheta_1)=\frac{k^2}{r_1^2}\left\{\int_b^a\frac{\sqrt{2}}{\omega\sqrt{\pi}}e^{-\frac{r_0^2}{\omega^2}}e^{\frac{jkr_0^2}{2}\left(\frac{1}{r_1}+\frac{1}{R_c}\right)}J_0(kr_0\sin\vartheta_1)r_0\,dr_0\right\}^2 \tag{2-3}$$

The intensity of the field produced at distance r_1 from a unit power isotropic radiator is:

$$I_0=\frac{1}{4\pi r_1^2}$$

Therefore, the transmitter telescope gain is define as the ratio;

$$G_t(r_1,\vartheta_1)=\frac{I(r_1,\ \vartheta_1)}{I_0}$$

$$G_t(r_1,\vartheta_1)=\frac{8k^2}{\omega^2}\left\{\int_b^a e^{-\frac{r_0^2}{\omega^2}}e^{\frac{jkr_0^2}{2}\left(\frac{1}{r_1}+\frac{1}{R_c}\right)}J_0(kr_0\sin\vartheta_1)r_0\,dr_0\right\}^2 \tag{2-4}$$

The gain depends on r_1 only in the near field. The main contributor to power losses in the transmitter telescope are the truncation by aperture boundary and obscuration ratios induced by the secondary mirror.

Let $r_0=s\times a$, where s is a dimensionless variable, the gain becomes;

$$G_t(r_1,\vartheta_1)=\frac{8k^2}{\omega^2}\left\{\int_{\frac{b}{a}}^1 e^{-\frac{a^2s^2}{\omega^2}}e^{\frac{jka^2}{2}\left(\frac{1}{r_1}+\frac{1}{R_c}\right)}J_0(s\times k\times a\sin\vartheta)a^2s\,ds\right\}^2 \tag{2-5}$$

To simplify the above equation, let us assign the following denotations;

$$u=s^2\ ,\ \alpha=\frac{a}{\omega}\ ,\qquad \gamma=\frac{b}{a}\ ,\qquad X=ka\sin\vartheta\qquad \beta=\frac{ka^2}{2}\left(\frac{1}{r_1}+\frac{1}{R_c}\right)$$

Therefore;

$$G_t(\alpha,\beta,\gamma,\ X)=\frac{4\pi A}{\lambda^2}\left\{2\alpha^2\left[\int_{\gamma^2}^{1}e^{-\alpha^2 u}\,e^{j\beta u}\,J_0\left(X\sqrt{u}\right)du\right]^2\right\} \tag{2-5}$$

The transmitter telescope efficiency factor $g_t(\alpha, \beta, \gamma, X)$

$$g_t(\alpha,\beta,\gamma,\ X)=\left\{2\alpha^2\left[\int_{\gamma^2}^{1}e^{-\alpha^2 u}\,e^{j\beta u}\,J_0\left(X\sqrt{u}\right)du\right]^2\right\}$$

$$G_t(\alpha,\beta,\gamma,\ X)=\frac{4\pi A}{\lambda^2}g_t(\alpha,\beta,\gamma,\ X)$$

Now, taking $\beta=0$ for far field gain and $X=0$ for on-axis gain; $g_t(\alpha, \beta, \gamma, X)=g_t(\alpha, 0, \gamma, 0)$

$$g_t(\alpha,\beta,\gamma,\ X)=\frac{2}{\alpha^2}\ \left[e^{-\alpha^2}-e^{-\gamma^2\alpha^2}\right]^2$$

$$G_t(\alpha,\beta,\gamma,\ X)=\frac{4\pi A}{\lambda^2}\left\{\frac{2}{\alpha^2}\ \left[e^{-\alpha^2}-e^{-\gamma^2\alpha^2}\right]^2\right\} \tag{2-6}$$

If the transmitter telescope efficiency factor is differentiated with respect to α

$$\frac{2\alpha^2+1}{2\alpha^2\gamma^2+1}e^{-\alpha^2(1-\gamma^2)}=1$$

The approximate solution is given as;

$$\alpha=1.12-1.30\gamma^2+2.12\gamma^4$$

$$G_t(\alpha,\beta,\gamma,\ X)=\frac{4\pi^2a^2}{\lambda^2}\left\{\frac{2}{\alpha^2}\ \left[e^{-\alpha^2}-e^{-\gamma^2\alpha^2}\right]^2\right\}$$

$$G_t(\alpha,\beta,\gamma,\ X)=\left(\frac{2\pi a}{\lambda}\right)^2\left\{\frac{2}{\alpha^2}\ \left[e^{-\alpha^2}-e^{-\gamma^2\alpha^2}\right]^2\right\}$$

$$G_t(\alpha,\beta,\gamma,\ X)=\left(\frac{\pi D_t}{\lambda}\right)^2\left\{\frac{2}{\alpha^2}\ \left[e^{-\alpha^2}-e^{-\gamma^2\alpha^2}\right]^2\right\}$$

$$G_t(dB)=20\log\left(\frac{\pi D_t}{\lambda}\right)+10\log\left(\frac{2}{\alpha^2}\ \left[e^{-\alpha^2}-e^{-\gamma^2\alpha^2}\right]^2\right) \tag{2-7}$$

The theoretical transmitter telescope gain derived above is only valid in an ideal optical system that is far from reality. The achievable gain and beamwidth are perturbed in real operations by wave front aberrations. The Strehl Ratio is therefore introduced as a metric for characterizing the performance of the optical system. [78] Defined it as the ratio of on-axis intensity in the focal plane with aberrations to intensity without aberration and dependent on the Wave-front Variance.

$$0 \leq S \leq 1$$

$$\sigma^2=\frac{1}{\pi}\int_0^{2\pi}\int_0^1[W(r,\vartheta)-\overline{W}]^2 r\,dr\,d\vartheta \tag{2-8}$$

$W(r,\vartheta)$ is the aberrated wave front while $\bar{W}$ is the mean aberrated wave front over the aperture. For small aberrations, equation (10) can be approximated to:

$$\sigma<\frac{\lambda}{2\pi}$$

And the Strehl ratio[79][80];

$$S\approx e^{-(\sigma^2)} \tag{2-9}$$

$$\sigma^2=1.03\left(\frac{D_t}{r_0^*}\right)^{\frac{5}{3}}$$

$$S=\frac{1}{1+\sigma^2}$$

$$S=\frac{1}{1+\left(\frac{D_t}{r_0^*}\right)^{\frac{5}{3}}}$$

$$\text{Provided } \frac{D_t}{r_0^*}<1$$

$$r_0^*=\left\{0.423k^2\int_0^L C_n^2(Z)\left(\frac{Z}{L}\right)^{\frac{5}{3}}dz\right\}^{-\frac{3}{5}} \tag{2-10}$$

For weak and strong turbulence conditions;

$$S\approx\left\{1+\left(\frac{D_t}{r_0^*}\right)^{\frac{5}{3}}\right\}^{-\frac{6}{5}} \tag{2-11}$$

$$\text{For } 0\le\frac{D_t}{r_0^*}\le\infty$$

2.3.2. Receiver Gain

A uniform plane wave of the transmitted signal impinges on the surface of the receiving aperture because of the large distance between the transmitter and the receiver.

$$G_r=\frac{4\pi A}{\lambda^2}(1-\gamma^2) \tag{2-12}$$

$$G_r(dB)=10\log\frac{4\pi^2r^2}{\lambda^2}+10\log(1-\gamma^2)=20\log\frac{2\pi r}{\lambda}+10\log(1-\gamma^2)$$

$$A = \pi r^2 \quad , \quad \gamma = \frac{q}{r}$$

$$G_r = \frac{4\pi^2 r^2}{\lambda^2}(1-\gamma^2) = \left(\frac{2\pi r}{\lambda}\right)^2 (1-\gamma^2)$$

$$G_r = \left(\frac{2\pi r}{\lambda}\right)^2 \left(1-\frac{q^2}{r^2}\right) \tag{2-13}$$

2.3.3. Received Optical Signal Power

The Friis transmission equation is applicable to both RF and optical communication channels. The received optical power at the receiver aperture is given by [81][82]:

$$P_{r\text{-}opt} = EIRP \times G_r \times L_{path} \times L_{atm} \times L_{rx\text{-}opt} \times L_{tx\text{-}opt} \times L_{point} \tag{2-14}$$

$$EIRP = P_t \left(\frac{\pi D_t}{\lambda}\right)^2 \tag{2-15}$$

The link budget relation

$$P_{r\text{-}opt}\,(dB) = 10 \log P_t + 20\left[\log\left(\frac{\pi D_t}{\lambda}\right) + \log\left(\frac{\pi D_r}{\lambda}\right) - \log\left(\frac{\lambda}{4\pi R}\right)\right] - \left(L_{atm} + L_{rx-opt} + L_{tx-opt} + L_{point}\right) \tag{2-16}$$

The biggest contributor to attenuation of the link is the Path Loss L_{path} which magnitude up to 310dB in the case of lunar apogee distance of 395,000km and infrared beam at 1550nm. When the Moon is at perigee of its orbit around Earth, the range is decrease to about 365,400km. Atmospheric loss, L_{atm} is dependent on weather conditions and cloud cover at the receiving station. MODTRAN atmospheric modelling simulation (Figure 2-4) reveals that atmospheric losses are minimal at 1550nm optical wavelength. The Pointing loss L_{point} also greatly impacts the link. This loss can be reduced with highly capable and precise ADCS and an agile ground telescope tracking mechanism.

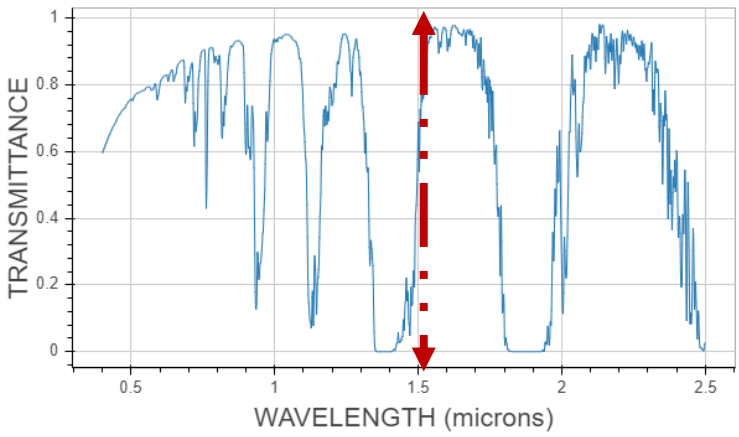

Figure 2-4: Atmospheric Transmittance [83]

2.3.4. Required Received Signal Power

The link margin is the difference between the received optical signal power from the satellite and the sensitivity of the photodetector. Due to the presence of background power and noise current in the APD, the fidelity of the received signal is determined by the BER given by:

$$P'_r = P_t \times \left(\frac{\pi D_t}{\lambda}\right)^2 \times \left(\frac{2\pi r}{\lambda}\right)^2 \times \left(\frac{\lambda}{4\pi R}\right)^2 \times L_T$$

$$P'_r(dB) = P_t(dB) + 20\log\left(\frac{\pi D_t}{\lambda}\right) + \left(20\log\frac{2\pi r}{\lambda}\right) - \left(20\log\frac{\lambda}{4\pi R}\right) - L_T$$

A good optical link must satisfy;

$$P'_r(dB) \gg P_r(dB)$$

$$\text{Link Margin} = P'_r(dB) - P_r(dB)$$

$$BER = \frac{1}{2}\text{erfc}\frac{Q_{req}}{\sqrt{2}} \tag{2-17}$$

The Q-factor is dependent on the nature of the APD, the photocurrents at on and off pulses

$$Q_{req} = \frac{\mu_1 - \mu_0}{\sqrt{\sigma_1^2 + \sigma_0^2}} \tag{2-18}$$

$$\mu_1 = M_{apd} R_{apd} (P_{peak} + P_{bg}) \tag{2-19}$$

$$\mu_0 = M_{apd} R_{apd} (P_{off} + P_{bg}) \tag{2-20}$$

Taking $P_{off} = -120.45\text{dBW}$ and $P_{bg} = -120.29\text{dBW}$

$$\sigma_1^2 = (2qM_{apd} NEBF_n \mu_1) + (M_{apd} R_{apd} NEP)^2 \tag{2-21}$$

$$\sigma_0^2 = (2qM_{apd} NEBF_n \mu_0) + (M_{apd} R_{apd} NEP)^2 \tag{2-22}$$

$$NEP = \frac{I_n}{R_{apd}} = \sqrt{\frac{4k_B T F_n}{R_{in} {R_{apd}}^2}} \tag{2-23}$$

APD Quantum efficiency:

$$Q_e = \frac{1240 R_{apd}}{\lambda} \tag{2-24}$$

The transmitter Extinction Ratio and PPM-order;

$$P_{peak} = P_{off} \times ER \tag{2-25}$$

$$PR_{peak-av} = \left(\frac{1}{M} + \frac{M-1}{M \times ER}\right)^{-1} \tag{2-26}$$

$$P_{req} = \frac{1}{PR_{peak-av}}\left(\frac{\mu_1}{M_{apd}R_{apd}} - P_{bg}\right) \tag{2-27}$$

2.4. Lasercom Modulation and Channel Coding

In a direct-detection system, Pulse Position Modulation (PPM) performs optimally compared to other signaling schemes [84]. The system data rate is given by:

$$R_b = R_{ecc}\frac{\log_2 M}{MT_s} \tag{2-28}$$

Where T_s is the slot width and the PPM modulation order $M \in \{16, 32, 64, \ldots . 2^{(n+3)}\}$ and the code rate:

$$R_{ecc} \in \left\{\frac{1}{3}, \frac{1}{2}, \frac{2}{3}\right\} \tag{2-29}$$

2.4.1. Optical Channel Capacity

Moison and Xie [85] provides expressions for the channel capacity in an optical channel at signal only and background noise regimes. At signal photoelectrons regime:

$$C_{OPT} = \frac{\log_2 M}{MT_s}\left[1 - \exp\left(-\frac{MP_rT_s}{\varepsilon}\right)\right] \tag{2-30}$$

When background noise is considered:

$$C_{OPTn} = \frac{1}{\varepsilon \ln 2}\left[\frac{P_r^2}{P_r\frac{1}{\ln(M)} + P_n\frac{2}{M-1}}\right] \tag{2-31}$$

The maximum achievable optical data rate:

$$R_{b\text{-}opt} \le C_{opt} = \frac{\log_2 M}{MT_s}\left[1 - \exp\left(-\frac{M \times P_t \times G_t \times G_r \times \lambda^2 \times \eta_s \times T_s}{(4\pi R)^2 \varepsilon}\right)\right] \tag{2-32}$$

Comparing the Optical and RF domains the data rates declines progressively with distance in Ka-band while it remains high in optical at very enormous distances, endorsing the suitability of optical links for deep-space applications.

$$C_{RF} = \frac{1}{\ln(2)}\frac{P_t \times G_t \times G_r \times \lambda^2 \times \eta_s}{(4\pi R)^2 KT} \tag{2-33}$$

$$\left(\frac{1}{R_{b\text{-}rf}}\right)\left(\frac{G_r}{T}\right)\left(\frac{1}{R^2}\right) = \frac{\ln(2) \times (4\pi)^2 \times K}{P_t \times G_t \times \lambda^2 \times \eta_s} \tag{2-34}$$

Table 2-2: RF and Optical Data Capacity Comparison

Parameters	*Optical*	*Ka-band*
Frequency	1550nm	27GHz
Tx Power	5W	6.98dBW
Rx Diameter	40cm	240cm
Rx Gain	118.15dB	52.3dB
G/T	-	28.88dBK
Signaling	PPM	QPSK
System Loss	-8dB	-3dB
Data Rate at Lunar Range	10^6 bps	10^3 bps

2.5. Pointing, Acquisition and Tracking Requirements

The beamwidth of the transmitted laser viz-a-viz the communication range and size of the receiving optical ground telescope determines the satellite platform attitude control and fine pointing requirements. An optical transmitter beamwidth must be large enough to accommodate the Cubesat pointing error [86][87]. To maintain the pointing losses with 3dB, the full width at half maximum (FWHM) beamwidth must be larger than the pointing error [88]. Hence for a 5cm aperture transmitter operating at 1550nm, the basic platform pointing requirement would be 23.25μrad. The laser beam divergence angle, half power beamwidth (HPBW), FWHM and the aperture diameter are related as presented in equations (2-35) to (2-37). Beam Divergence is expressed as:

$$\phi = 2.24 \left(\frac{\lambda}{D_t}\right) \tag{2-35}$$

$$\text{HPBW} = \frac{4}{\pi} \times \left(\frac{\lambda}{D_t}\right) \tag{2-36}$$

The beam pointing requirement is given by:

$$\theta_p = \frac{\theta_{FWHM}}{2} = \frac{3}{4} \times \left(\frac{\lambda}{D_t}\right) = 23.25\mu\text{rad} \tag{2-37}$$

High precision laser pointing, acquisition and tracking (PAT) mechanisms are essential for achieving continuous line-of-sight connectivity between the optical transmitter and receiver. It also becomes indispensable in mitigating beam misalignment problems caused by satellite attitude variations, perturbations by micro-vibrations and moving subsystems. PAT mechanisms are generally implemented in two stages; coarse pointing and fine pointing subsystems for keeping a steady communication link [89][90][91][92]. Coarse pointing involves the initial pre-alignment of the optical heads, utilizing directional guiding beacons or

positional sensors (GNSS) [93] attitude actuators and sometimes the platform's propulsion systems. In the deep space scenario where GPS service is not available, the satellite PAT system must rely on ground beacons operating on a different wavelength from the signal uplink and downlink bands.

Point-Ahead systems compensates for the relative motion between a moving satellite in the orbit and a quasi-static ground telescope. The system ensures that the transmitted beam is steered in advance to the estimated direction that the ground station would be at a later time. The point-ahead angle, Ω is related to the transmitter-receiver relative velocity by [94][95][96]:

$$\Omega = \frac{2V_r}{3x10^8} \tag{2-37}$$

Fine pointing systems (FPS) performs more accurate beam alignment and precision control irrespective of the platform's movement, attitude changes and induced jitter. Fine Steering Mirrors are usually employed with optical sensors in a close-loop control to implement the fine pointing system.

2.6. Propagation Channels

2.6.1. Compensation for Atmospheric Turbulence

Atmospheric turbulence are optical disturbance effects that adversely perturbs the wavefront of transmitted laser beam propagating through the free-space atmospheric channel. The disturbance effects are random variations in the refractive index of the air medium due to unpredictable temperature variations causing beam wander, spreading and scintillation at the aperture of the receiving telescope [97]. The Fried parameter r_0 also known as the atmospheric coherence length is the measure of atmospheric turbulence level and dependent on wavelength, zenith angle and the structure parameter:

$$r_0 = \left[0.423k^2 \sec\theta \int_{h_o}^{h_0+L} C_n^2(h)dh\right]^{-\frac{3}{5}} \tag{2-38}$$

The refractive index structure parameter defined in the Hufnagel Valley Boundary model [26]:

$$C_n^2(h) = m \times 0.00594\left(\frac{\upsilon}{27}\right)^2 (10^{-5}h)^{10}e^{-\frac{h}{1000}} + 2.7 \times 10^{-6}e^{-\frac{h}{1500}} + Ae^{-\frac{h}{100}} \tag{2-39}$$

$$\upsilon = \left[\frac{1}{15\times10^3}\int_{15\times10^3}^{20\times10^3} V^2(h)dh\right]^{-\frac{1}{2}} \tag{2-40}$$

$$V(h) = \omega_g h + v_g + 30\exp\left(-\frac{h-9400}{4800}\right) \tag{2-41}$$

Roytov variance:

$$\sigma_R^2 = 1.23 C_n^2 k^{\frac{7}{6}} L^{\frac{11}{6}} \tag{2-42}$$

Scintillation Index [98]:

$$\sigma_I^2 = \exp\left[\frac{0.49\sigma_R^2}{\left(1+1.11\sigma_R^{\frac{12}{5}}\right)^{\frac{7}{6}}} + \frac{0.51\sigma_R^2}{\left(1+0.69\sigma_R^{\frac{12}{5}}\right)^{\frac{7}{6}}}\right] - 1 \tag{2-43}$$

Adaptive optics system is applied for wavefront error compensation and degradation induced by atmospheric turbulence. Juan et al [78] modified the antenna gain to account for turbulence effect:

$$G_r = 10\log_{10}\left\{\left(\frac{\pi D_r}{\lambda}\right)^2 + S_{com}\right\} \tag{2-44}$$

$$S_{com} = \left[1 + (\sigma_j)^2 + 0.5(\sigma_j)^4 + 0.167(\sigma_j)^6\right]^{-\frac{6}{5}} + \left[\frac{1}{K_2} + (K_2 + 0.35)\left(\frac{D}{r_0}\right)^{\frac{5}{3}}\right]^{-\frac{13}{10}} \tag{2-45}$$

$$\sigma_j{}^2 = K_2\left(\frac{D}{r_0}\right)^{\frac{5}{3}} \tag{2-46}$$

$$K_2 = 0.24(N)^{-\frac{5}{3}} \tag{2-47}$$

Aperture averaging mitigates the effect of atmospheric turbulence by setting the size of the receiver aperture such that fast intensity fluctuations generated by small eddies. The factor A_F is the measure of the reduction in channel fading with the help of aperture averaging. Churnside approximation of A_F for plane wave in weak turbulence [99]:

$$A_F = \left[1+1.07\left(\frac{kD^2}{4L}\right)^{-\frac{7}{6}}\right]^{-1} \tag{2-48}$$

3. LUNAR CUBESAT LASERCOM DESIGN REFERENCE MISSION

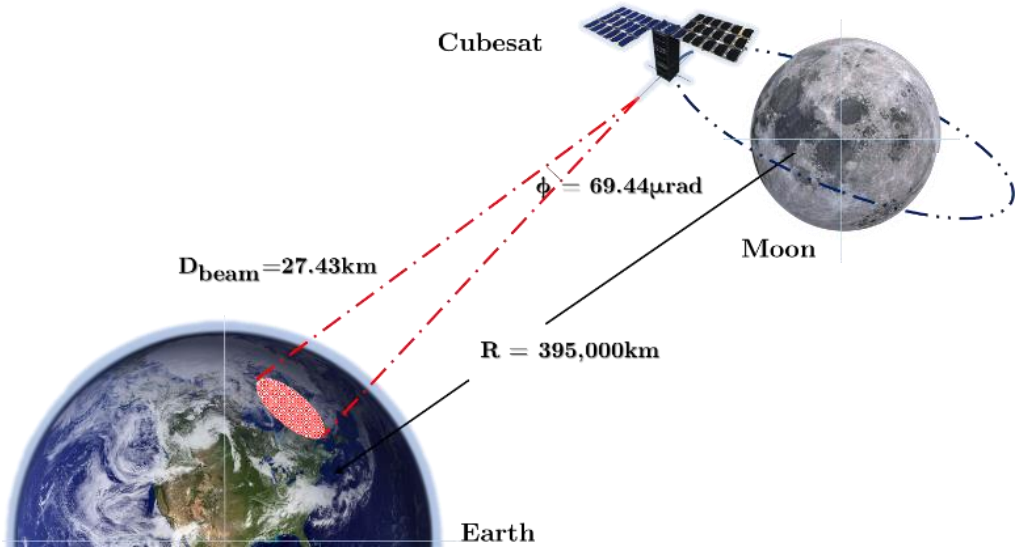

Figure 3-1: LaSEINE-Lunar Moon to Earth Optical Communication Link.

3.1. Introduction

The LaSEINE-Lunar concept introduced in this Chapter is an hypothetical design reference mission (DRM) adopted by this research to study the feasibility analysis of direct laser communication from a Moon orbiting CubeSat and an Earth-based optical ground station. Achieved transfer rates and overall exchanged data volume to and from small satellites in deep-space missions are limited by RF bandwidth, platform size, weight and power (SWaP) constraints. Spacecrafts and planetary probes in deep space regions communicating using upper limits of the RF channel (S, X and Ka bands) with the Deep Space Network (DSN) perform within few kilobits per seconds to the peaks of scanty megabits per seconds. More recently, advanced and future missions are demanding higher capacity unsupported by the DSN. This reassert the constraints of the present architecture and the need for gradual adaption of deep space optical network for future planetary explorations. Deep space optical communications technology involves the use of laser beams to encode and transmit information at superior data rates over enormously large distances compared to radio frequency (RF) channel based communication systems.

The performance of laser communication makes it very attractive for space applications such as direct space to ground links, inter-satellite and inter-orbital networks, especially in cases of larger separating distances. Laser beam narrow beamwidth enhances concentration of the transmitter EIRP and supersedes similar RF system throughput with equal power and weight by several order of magnitude increase. The viability of optical communicating Cubesat in lunar orbit with a small-scale, amateur-class telescope ground segment is analyzed in this Chapter. An annual link availability and outage estimation is evaluated for a fixed ground terminal and the link performance is compared at different weather conditions.

3.2. Mission Requirements

Considering a 6-U Cubesat in a lunar orbit, 395,000km range with a compact, 40cm low-cost telescope on Earth achieving 250Mbps Pulse Position Modulated downlink. The Cubesat optical communication payload features a 5Watts, 1550nm Solid State Laser and MEMS Steering Mechanism to provide beam pointing control. Julian and Douglas [100] detailed a similar set of 12 viable DRMs of deep space optical communications for NASA operational use. Table 3-1 below compares some system parameters of the LLCD mission with the LaSEINE-Lunar. Previous optical communication missions have been mostly for technology demonstration rather than a critical mission requirement utilizing the high data throughput. An optical link operating at 250Mbps means 450GB data transfer in 30mins and 22TB for a cumulative 24hours of acquisition of signal (AOS). It is indeed challenging to match an existing CubeSat payload or scientific instrument capable of generating the data volume that will maximize the target 250Mbps rate of the optical communication module. This DRM proposes "Moon Walk": Ultra high definition & 3D virtual reality mapping of entire lunar surface and high resolution imaging using a Cubesat. The system parameters are dictated based on the size, weight and power constraints of the platform to derive the optimum rate, signaling schemes and identification of COTS components for the system implementation.

Figure 3-2: JAXA Moon Viewer

Table 3-1: Lunar Optical Comms Mission Comparison

Parameters	*LADEE-LLCD*	*LaSEINE -Lunar*
Data Rate	622Mbps, 77Mbps	250Mbps
Tx Optical	0.5W downlink	5W downlink
Wavelength	1550nm	1550nm
Platform Size	117cm	6U

Platform Weight	175kg	~20kg
GS Telescope	100cm, 40cm x 4 array cryogenic	40cm Dobsonian, InGaAs APD
GS Diversity	Yes	Fixed
Cost	Expensive	Cheaper

3.3. System Design Considerations

3.3.1. Lasercom Optical Module

Options for the laser source includes a standalone high power laser source or combination of low-power semiconductor fiber laser source and Erbium-Doped Fiber Amplifier (EDFA). Other components of the optical module includes beam collimator assembly, expander optics, MEMS fine beam steering mirror and the driver units. A good candidate for the standalone laser source is the Akela fiber coupled laser module (ALC-1550-07000-FM200.22-R). With a maximum of 7W optical output, the module is deemed adequate to provide 5W transmitter optical power sufficiently. Its package dimension (38mm x 38mm x 12mm) also fits well within the available space of the optical module. The transmitting optics final aperture (5cm) is constrained by the attitude control system capability and beam divergence which also impacts the amount of photons that can be captured by a given size of receiving aperture within the beam footprint diameter on ground. The fine steering mirror provides additional dual-axis beam pointing correction when perturbed by platform micro-vibrations or attitude changes.

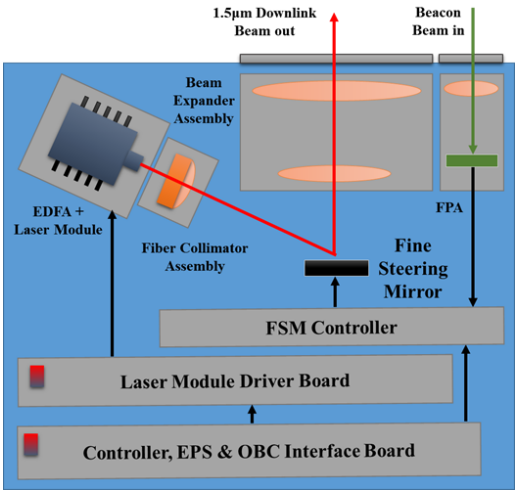

Figure 3-3: Cubesat optical module layout

3.3.2. CubeSat Structure Space and Power Management

As a result of the subsystems power consumption, particular by the lasercom module, it is important to have a platform that is capable of generating and storing excess energy. A two wings double deployable solar arrays in-addition to the body mounted cells, becomes ideal

on the CubeSat structure to increase the available solar panel area needed to generate the orbit power demand.

The electrical power requirement of the optical module is estimated to be 30W and budgeting 30W for other subsystems indicates the minimum amount of power generation by the Cubesats solar cells. We estimate a baseline total power consumption more than 100W (average value to be determined by the imaging payload instruments). The LaSEINE-Lunar 6U Cubesat will need to generate at least 100W at the beginning of life (BOL), 50W BOL per wing. DHV Technology manufactures qualified 6U deployable solar arrays for deep space missions [101].

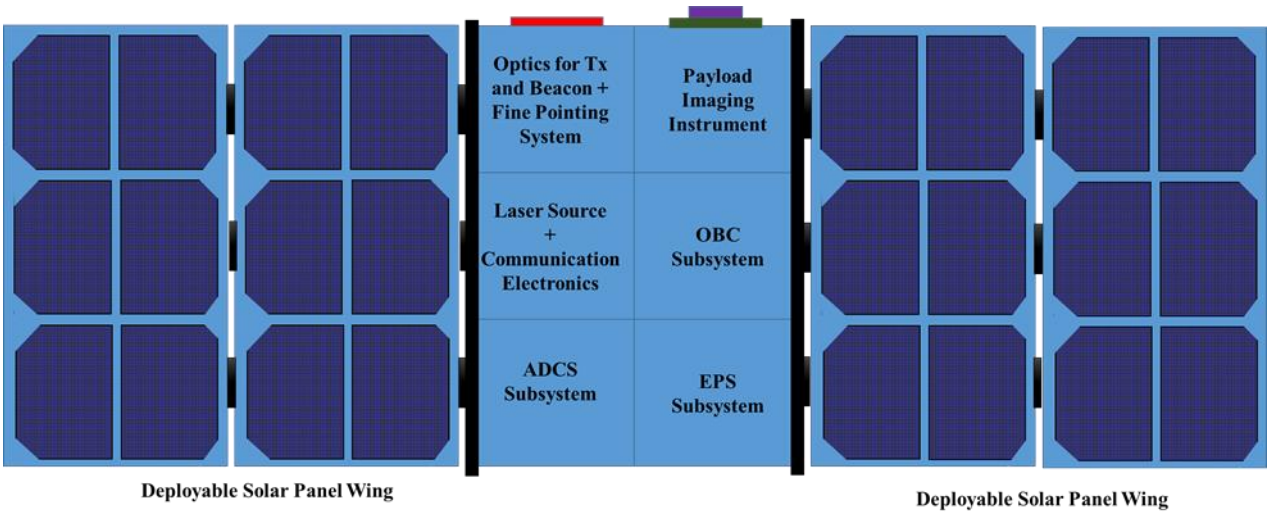

Figure 3-4: Structure and subsystems distribution

The GOMSpace 6U premium platform is also an alternative COTS solution which comes integrated with the NanoPower Tracking Solar Panels (TSP): NanoPower P60 and two 8 cell battery packs. The platform is likewise compatible with NanoMind A3200 onboard computer (OBC), NanoCom SR2000 S-band 500Kbps to 6Mbps for telemetry and command link. It also comes handy with an electric propulsion system having a typical bus power consumption of 50W. The double deployable array maximum orbit average power generation is 100W and standard platform mass without payload is 7.5kg. Figure 3-6 illustrates an example allocation of space of the 6U structure to the important subsystems.

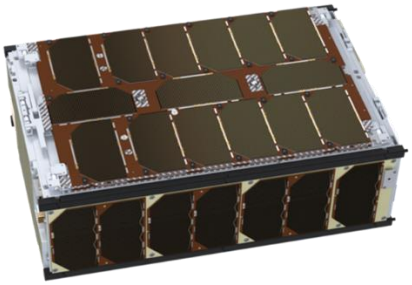

(a)

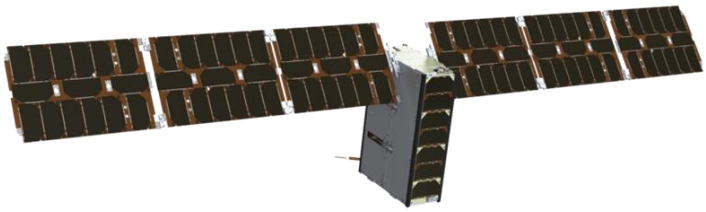

(b)

Figure 3-5: GOMSpace 6U CubeSat premium platform (a) stowed and (b) deployed panels. (Image Source: [102])

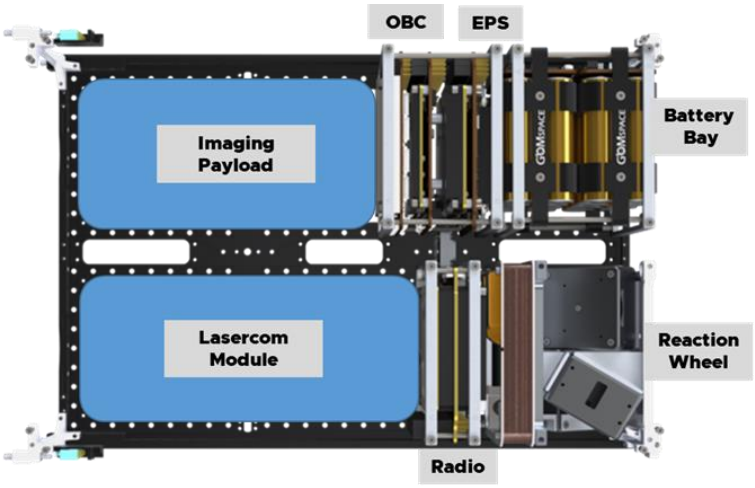

Figure 3-6: Typical distribution of subsystems inside the GOMSpace 6U CubeSat structure. (Adapted Image from [103])

3.3.3. Attitude Determination & Control System

Owing to the high directivity of the output laser, a highly precise attitude control system and accurate beam pointing during each satellite-to-ground telescope line of sight access is a very strong requirement of successfully establishing a communication link. In order to achieve this, the ADCS unit must include sensors suites for high fidelity attitude knowledge and determination. LaSEINE-Lunar requires an attitude pointing accuracy of θ_p=23.25μrad (calculated from the half-power beamwidth) for a 5cm transmitting optics aperture. The COTS

BCT-XACT is a flight proven, compact module suitable for the mission. XACT was flown on the MinXSS 3U CubeSat with good performance reported [104][31]. It featured star tracker, sun sensor and actuators (three-axis reaction wheel and torque rod).

Figure 3-7: Blue Canyon Tech XACT module [106].

Table 3-2: BCT-XACT COTS ADCS Module Specifications

Parameters	*Specifications*
Accuracy	0.003° or 52.35μrad (1-σ) for 2 axes and 122.17μrad (1-σ) for 3rd axis
Power	1W nominal, 2.8W peak
Operating voltage	5V, 12V Selectable
Size	0.5U (0.85kg)
Sensors	Nano-star trackers, sun sensor, MEMS IMU, Magnetometer
Actuators	3-Axis reaction wheels, 3 torque rods

3.3.4. Compact Telescope-Ground Segment

The telescope-ground segment architecture and top-level components are shown in Figure 3-8 below. The receiving aperture size is based on the need to develop a low cost optical ground receiver. Dobsonian telescope (modified Newtonian telescope) is suitable for space to ground downlink collection. It is commonly used by amateur astronomers and readily available. The telescope has a compact, streamlined structure and lend itself easily to good observation of faint sky objects. Scintillation, wavefront aberration and beam wander of the downlink laser light caused by atmospheric turbulence adversely affects the receiving system. Mitigation of these effects include taken advantage of the aperture-averaging factor (discussed in section Chapter 2), gain compensation and use of adaptive optics. An example of COTS deformable mirrors is the Alpao DM65-DM85 series which have large deformation and high dynamic motion. An azimuth and elevation motor driven tracking system will ensure that the telescope tracks the satellite and pointed accurate to achieve maximum signal light collection.

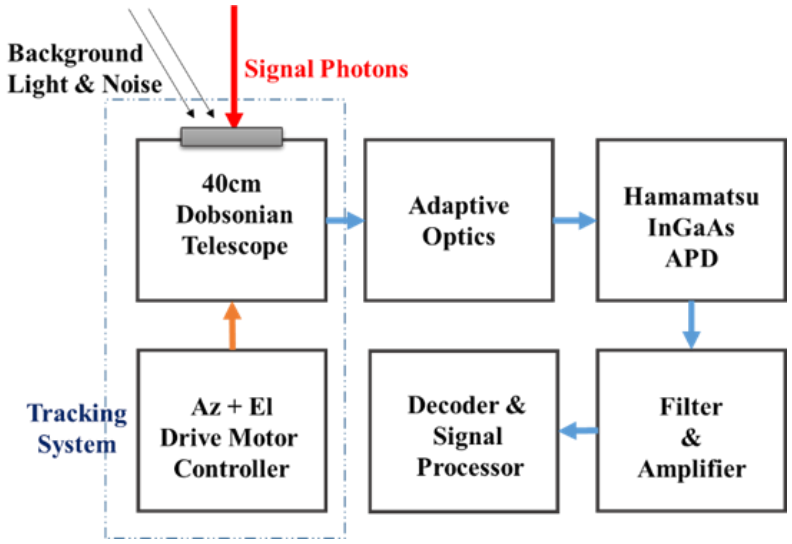

Figure 3-8: Block diagram of the telescope ground segment

3.4. Link Budget Summary

Table 3-3: LaSEINE-Lunar CubeSat Optical link budget summary

System Parameters	*Values*	*Units*
Link Range	395000	km
Modulation PPM Order	128	
Slot width	70	ns
Coding rate	0.33	
Data Rate	250	Mbps
Transmitter Optical power output	5	W
Wavelength	1550	nm
Extinction ratio	37	dB
Half-power beamwidth	39.5	μrad
Beam divergence	69.44	μrad
Transmit optics aperture	5.0	cm
Transmitter gain	100.12	dBi
Transmit optical loss	-0.50	dB
Output photon flux	108.19 dB Photons/sec	
Pointing loss	-3.0	dB

Path loss	-310.1	dB
Atmospheric loss	-3.0	dB
Background noise power	9.34E-13	W
Sky spectral radiance	6.00E-04	
Beam footprint diameter	27.43	Km
Receiver optics aperture	40.0	cm
Receiver optical loss	-2.0 dB	
Receiver gain	118.15 dB	
Received photon flux	96.57 dB Photons/sec	
Responsivity	0.9 A/W	
Gain	30	
Excess noise figure	0.7	
Quantum efficiency	0.72	
Noise equivalent power	1.68E-11 W	
Noise equiv. bandwidth	3.00E8 Hz	
Required BER	1e-4	
Signal power at detector	-92.34 dBW (18.2 photons/bit)	
Signal power required	-94.94 dBW (10 photons/bit)	
Link Margin	1.6 dB	

3.5. Line-of-Sight Link Duration Simulation

In order to determine the link and outage duration due to the satellite orbital motion with respect to a notional ground station in Kitakyushu, the LaSEINE-Lunar mission orbit was simulated in STK using the astrogator orbit propagation model. The satellite orbits the Moon at an inclination of 90^0. Time parameter was set at year 2018 in order to match with available historical weather data.

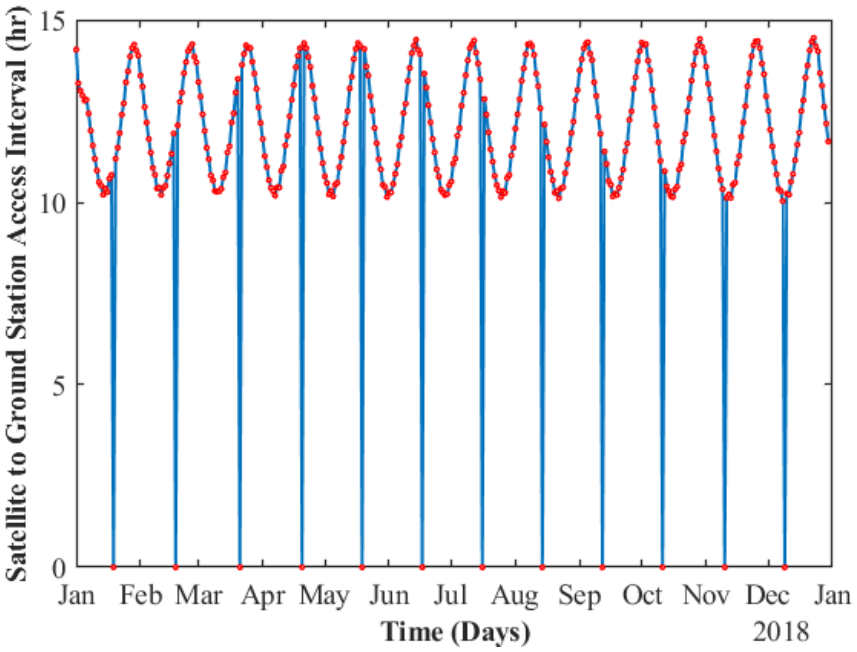

Figure 3-9: Ground station access simulation result

3.6. Impact of Weather Condition on the Link

The passage of laser beams through the Earth atmosphere results to loss of intensity and link outage especially during bad weather conditions. The predominant obstacle to laser beam propagation is cloud cover and is often estimated statistically. Thick cloud cover over the receiving telescope can also result to immediate signal outages. Therefore, ground segment site locations are chosen to be places with less cloud activity, preferably higher elevation. Fog and rain are prevalent weather effects at which significantly attenuates laser signals. The signal loss due to fog and rain is obtained by the relation:

$$L_{atm}(dB) = 10\log\{\alpha_{fog}h_{fog} + \alpha_{rain}h_{cloud}\} \quad (3\text{-}1)$$

3.6.1. Fog and Cloud Cover

Optical signal attenuation in the atmosphere is caused by absorption and scattering of light as it interact with gases and water vapor molecules in the air. During fog events and low visibilities, Mie scattering is produced when the light wavelength is comparable with the aerosol particles. Rayleigh scattering is produced during haze because the particle sizes are less than the wavelength. Attenuation is lower during rainfall, snow and hail because the particle sizes are much larger than the wavelength [107]. Stratus or low clouds (at 1.98km altitude) can cause fog and very low visibility. The specific atmospheric attenuation coefficient is a function of visibility (measure of distance at which light or object can be distinctly discerned) and expressed in Kim's model [108] as follows:

$$\alpha_{fog} = \frac{17}{V}\left(\frac{\lambda}{550}\right)^{-q} \quad (3\text{-}2)$$

$$g = \begin{cases} 1.6, (V > 50km) \\ 1.3, (6km < V < 50km) \\ 0.16V+0.34, (1km < V < 6km) \\ V-0.5, (0.5km < V < 1km) \\ 0, (V < 0.5km) \end{cases} \quad (3\text{-}3)$$

Figure 3-10: Clear sky at night and daytime cloud cover (Images Credit: [109][110])

Table 3-4: Specific Attenuation for fog conditions

Weather Condition	*Visibility (km)*	*dB/km a t 1550nm*
Heavy Fog	0.1	170
Light Fog	0.5	34
Haze or Smoke	4	1.54
Clear	>10	<0.44

3.6.2. Rain Attenuation

The specific rain attenuation coefficient is dependent on the drop size and temperature. The International Telecommunication Union (ITU-R P.1814) proposed a model for rain attenuation prediction in free-space optical systems. For a location in Japan. The rain rate, R (mm/hr) is related with the attenuation coefficient as given by [111]:

$$\alpha_{rain} = 1.58R^{0.63} \quad (3\text{-}4)$$

Table 3-5: Attenuation for rain conditions

Rain Intensity	*Rain Rate (mm/hr)*	*dB/km at 1550nm*
Light	3	3.16
Average	15	8.70
Heavy	>30	13.47

Weather data was obtained for atmospheric visibility at Kitakyushu airport for year 2018 from METAR data archive available at [112]. Hourly rain rate data for year 2018 was acquired from the JAXA global rainfall watch system; Global Satellite Mapping of Precipitation (GSMaP).The system aggregates data from different weather satellites and sources such as the U.S. National Oceanic and Atmospheric Administration (NOAA) Climate Prediction Centre, European Meteorological satellites Organization (EUMETSAT) and the NASA/GSFC Precipitation Processing System.

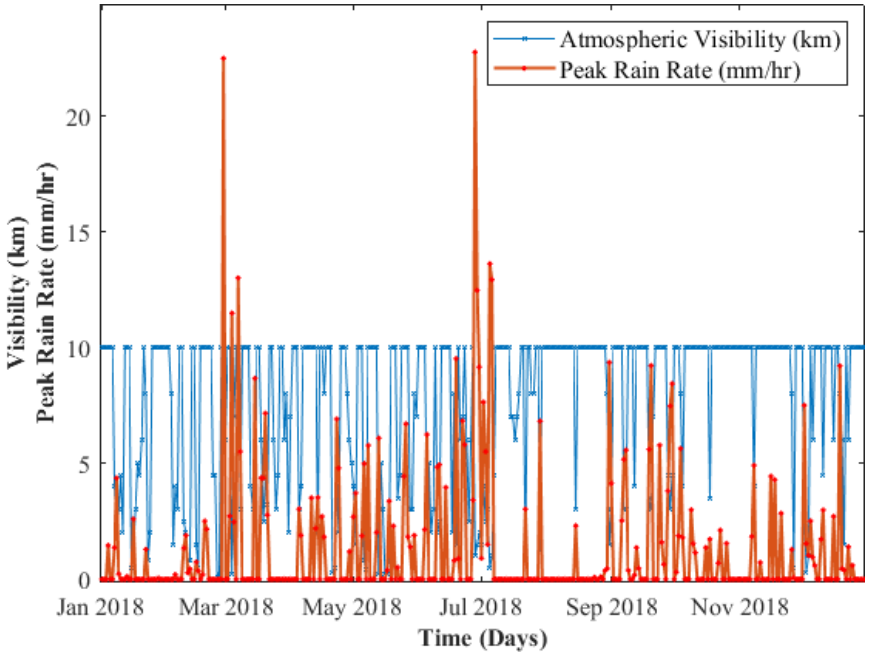

Figure 3-11: Kitakyushu atmospheric visibility and rain rate

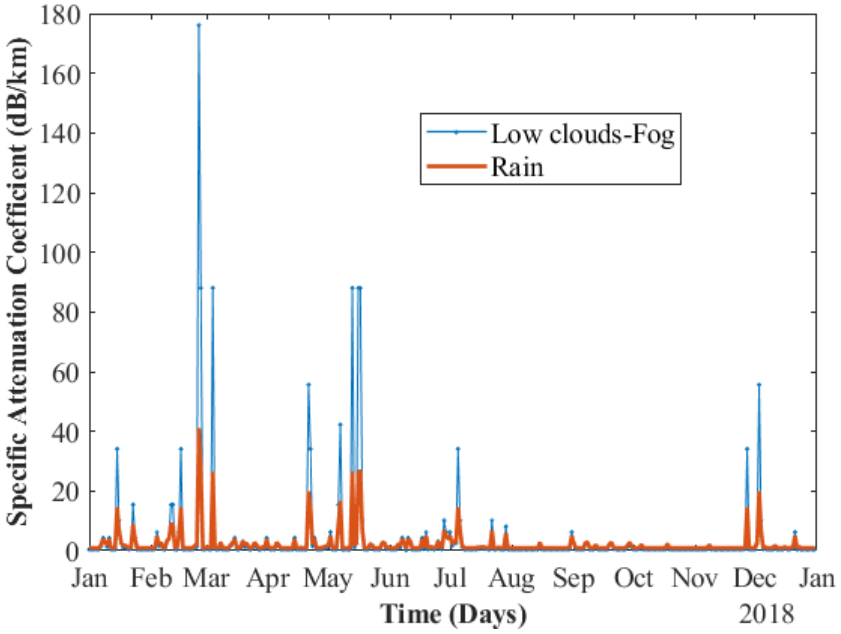

Figure 3-12: Specific attenuation coefficient

3.7. Link Outage Probability Estimation

Outage probability is defined as the ratio of the length of outage time in the link and the total observation interval. Figure 3-14 below presents the link availability simulation for a conceptual Moon orbiting CubeSat and a ground station in Kitakyushu. The sum $\sum_n(T_{out})$, is the outage periods out of the total observation time that the link is not available as a result of satellite not within line-of-sight of the receiving telescope and when the QoS (quality of service) is below the link margin and the BER threshold. The total link time is define as:

$$\Psi = \frac{\text{Lenth of outage time}}{\text{Total observation time}} = \frac{\sum_n(T_{out})}{T_{obs}} \tag{3-5}$$

$$\sum_n(T_{out}) = T_{out}^{access} + T_{out}^{pointing} + T_{out}^{fog\text{-}cloud} + T_{out}^{rain} \tag{3-6}$$

$$T_{link} = T_{obs} - \sum_n(T_{out}) \tag{3-7}$$

Link Availability, A

$$A = 1 - \Psi = \frac{T_{obs} - \sum_n(T_{out})}{T_{obs}} \tag{3-8}$$

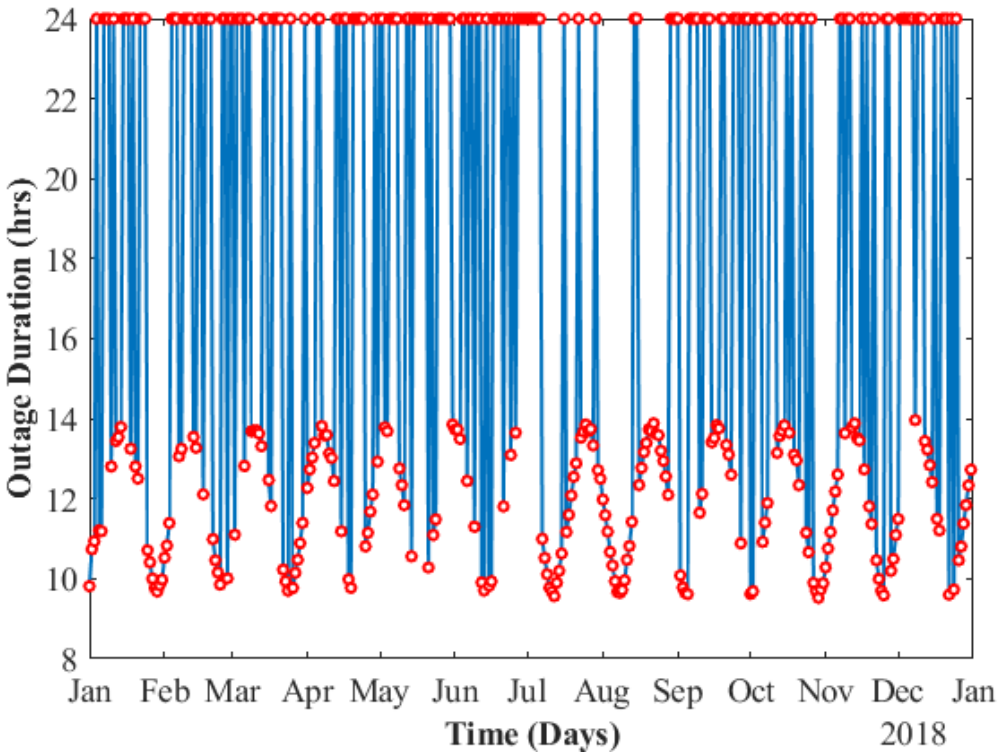

Figure 3-13: Link outage duration

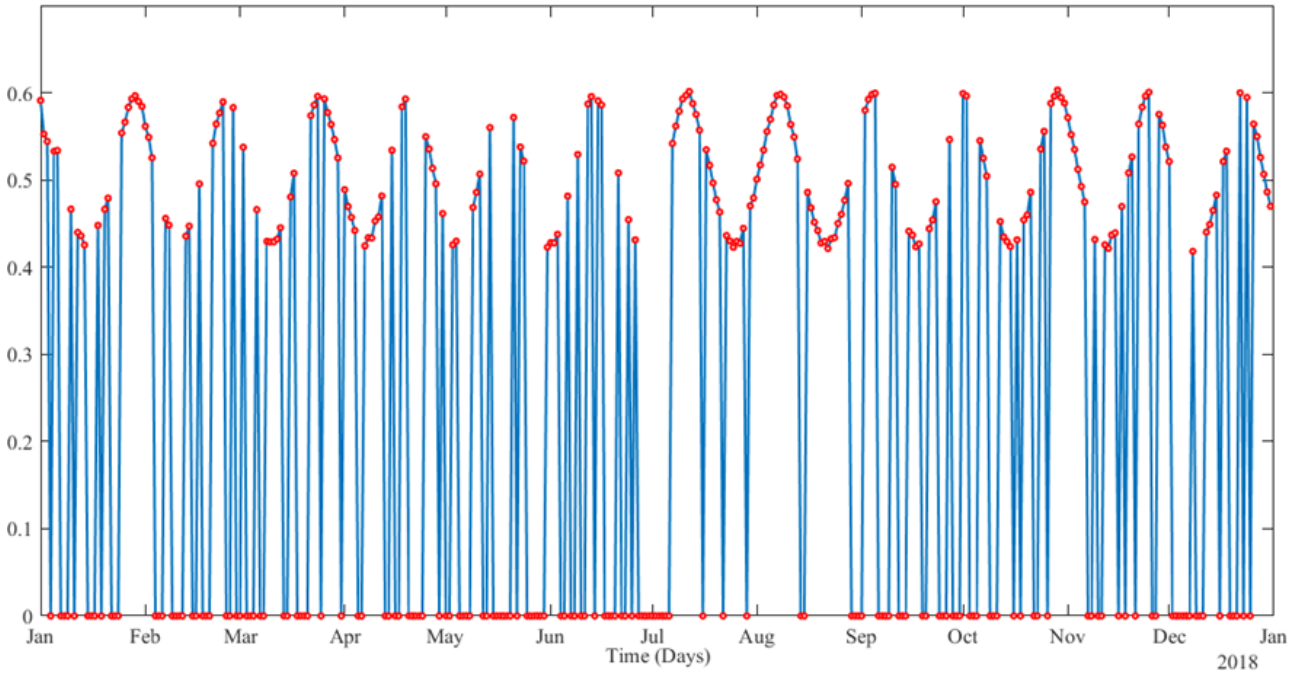

Figure 3-14: Optical link availability during weather conditions of year 2018

3.8. Summary

Typical allocation of the satellite on-board resources, most importantly power consumption by the optical module, payload and other subsystems shows that it is practicable to integrate laser communication transceiver on a 6U CubeSat platform. Required COTS components including ADCS and MEMS fine steering mirror units with desired capabilities are readily available. The ground segment described featuring is a low-cost telescope adaptable to the system architecture for achieving 250Mbps laser link from lunar orbit (400, 000km range). Use of adaptive optics (deformable mirrors) helps mitigate effects of wavefront aberration and scintillation induced by atmospheric turbulence. The selected photodetector possess adequate gain and responsivity characteristics to achieve required 10^{-4} BER threshold for the optical link margin. The estimated the link availability and outage probability due to the weather conditions for 2018 calendar year deduced that the link would be maintained for averagely 50% of time each day of the year. Peak atmospheric attenuations were noticed during heavy fog events with low atmospheric visibility. It was shown in the simulation that attenuation due to rain and visibility follows similar pattern throughout the year. Heavy rainfall events would have had strong impacts on the link but fog and cloud cover remains the biggest contributor.

4. PHOTODIODE ARRAY AIDED LASER BEAM STEERING EXPERIMENT

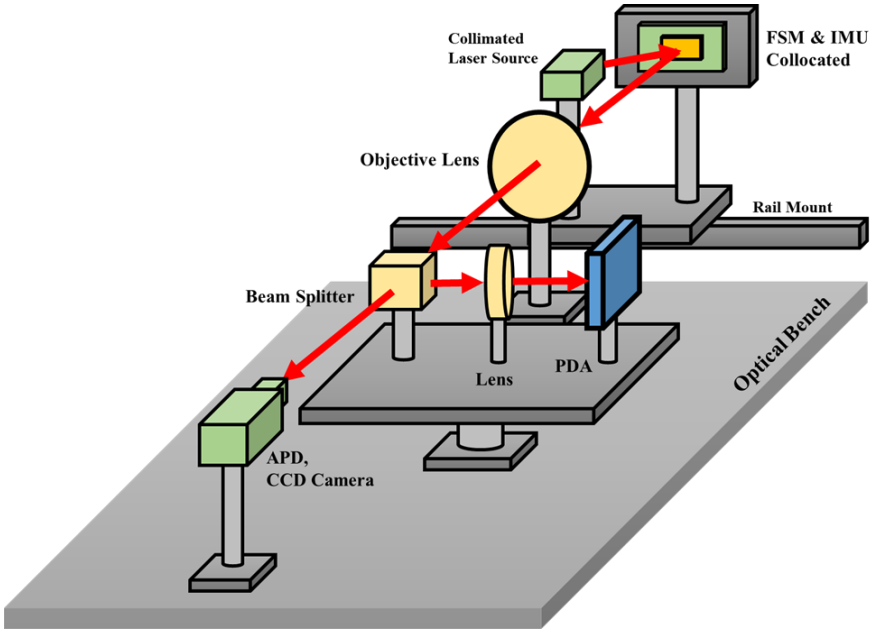

Figure 4-1: Photodiode Array Sensor Test-bed Layout

In this section, a new approach of utilizing Photodiode Array (PDA) as an optical feedback sensor in control of a one-axis micro-electromechanical (MEMS) fine steering mirror is presented. The system stabilizes a laser communication link assembled on an optical bench in the laboratory. Disturbance profiles similar to vibrations on dynamic platforms are induced into the setup using an electrodynamic vibration machine to test the efficacy of the fine steering control mechanism. Collocated with the PDA sensor was an Avalanche Photodiode (APD) at the receiving section providing continuous information about the transmitter's movements and beam displacements while the received optical signal strength is monitored. The feedback signals are transmitted to the FSM controller via an XBee radio link. The constructed prototype, conducted experiment and results obtained demonstrated the capability to stabilize a laser beam transmission in the presence of external disturbances and platform movements using a PDA sensor assisted control.

4.1. Architecture of Lasercom Pointing Systems

Fine pointing systems are not limited to satellites. Airborne and mobile ground platforms are equally suitable to hosting lasercom transceivers which requires an accurate fine tracking and beam alignment system. High precision laser pointing, acquisition and tracking (PAT) mechanisms are indispensable in mitigating beam misalignment problems in optical links. PAT mechanisms are generally implemented in two stages; coarse pointing and fine pointing subsystems for keeping the communication link [89][91][92][90]. Coarse pointing involves pre-aligning the optical heads, utilizing directional (guiding beacons) or positional sensors (GNSS)

[93], attitude actuators and sometimes the platform's propulsion systems. Fine pointing systems (FPS) are dedicated to more accurate beam alignment and precision control irrespective of the platform's movement, attitude changes and induced jitter.

Pointing instability on satellite platforms are a result of high-frequency micro-vibrations generated by the reaction wheel imbalances [113][114]. Rotary-wings based aircrafts and multi-rotor propelled Drones also experiences significant vibrations that must be damped or isolated when hosting optical imaging or direct laser transmission devices [115]. Fine Steering Mirrors (FSM) are extensively used in laboratory optical setups and in lasercom FPS to maneuver outgoing laser beams to desired directions. Combination with inertia sensors such as accelerometers and gyroscopes enables continuous tracking of the platforms attitude and implementation of robust closed-loop control [116][117]. Additional optical tracking Focal Plane Array (FPA) sensors such as Quadrant Detectors (QD), Position Sensitive Device (PSD) and Charge-Coupled Device (CCD Cameras) monitoring the transmitted beam enhances the performance of the FPS control system [118][119]. CCD cameras are excellent choice for conducting detailed laser beam profiling but generally suffers low frame rate adding unwanted time delay to the control feedback loop and limiting the disturbance rejection bandwidth. They are also bulkier and consume more power than the others. PSDs are highly sensitive and provide rapid response [120]. QD and PSD are however limited in aperture size, often requiring the use of additional optics for wider field of view. FPS for a low SWaP (size, weight and power), resource limited platform such as Cubesats and Drones must be compact and efficient. A tradeoff consideration between key characteristics such as resolution, speed or sampling rate, effective aperture and power consumption of the most suitable optical tracking sensor becomes essential.

Existing FSM beam control systems uses inertial sensors, QD, PSD and CCD as feedback elements [116][121][122][123]. Adaptation of PDA as demonstrated by the foregoing experiment, improves the performance and speed of tracking laser beam position. An application is in the case of ground beacon light illuminating the Fine Pointing System (FPS) of deep- space bound lasercom satellite

4.2. Segmented Quadrant Detectors

Quadrant Detectors (QD) are primarily used for light position detection and light switch applications. Figure 4-3 showcases an example of the use of a QD for laser beam control. However, in long-range FSO link with severe background light interference, QD performance and accuracy is degraded because of the weak light incident on its aperture, hence low SNR at the receiver [124]. QD also have limited FoV due to the number of pixels/elements. Additionally, the laser spot size vis-à-vis the aperture size gives rise to accuracy limitations when detecting bigger beams. An example of QD device is the Hamamatsu S4349 PIN Silicon Quad-cell Photodiode which can be interfaced with LTC1053CSW quad-precision operational amplifier for detecting a laser beacon signal. In the laboratory prototype assembled, the output of the amplifier was connected to a microcontroller ADC enabling seamless centroid calculation.

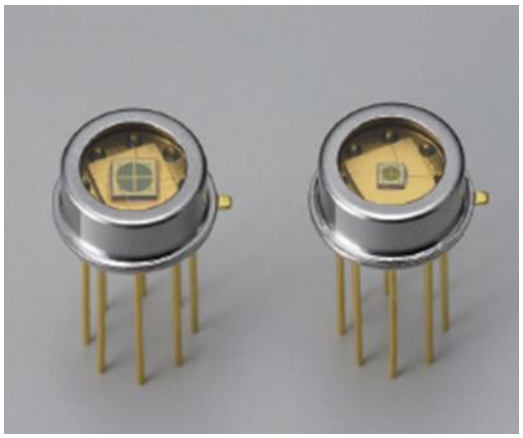

Figure 4-2: Hamamatsu G6849 InGaAs PIN QD

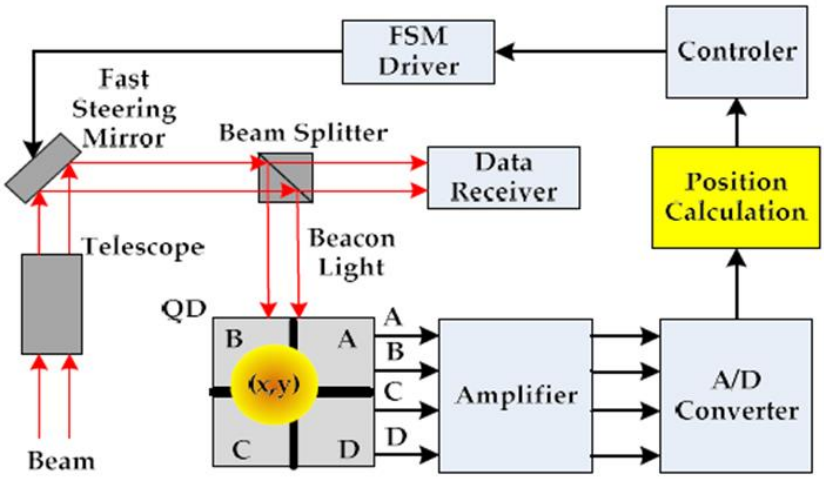

Figure 4-3: Application of QD as an optical feedback sensor. Source: [125]

4.3. Lateral Effect Position Sensitive Detectors

Position Sensitive Detectors (PSD) operate on the principle of photodiode surface resistance. They contain four electrodes with each relative potential proportional to the horizontal and vertical distances to the incident laser spot. On the other hand, PSD suffers non-linearity towards the outer edges of its aperture. Some COTS Position Sensing Devices are the S5981, S5991 and S1880. The Hamamatsu C9069 is an independent board for evaluating the devices. The board has a USB interface to the PC and utility software showed in Figure 4-5.

Figure 4-4: Hamamatsu C9069 mounted on evaluation board

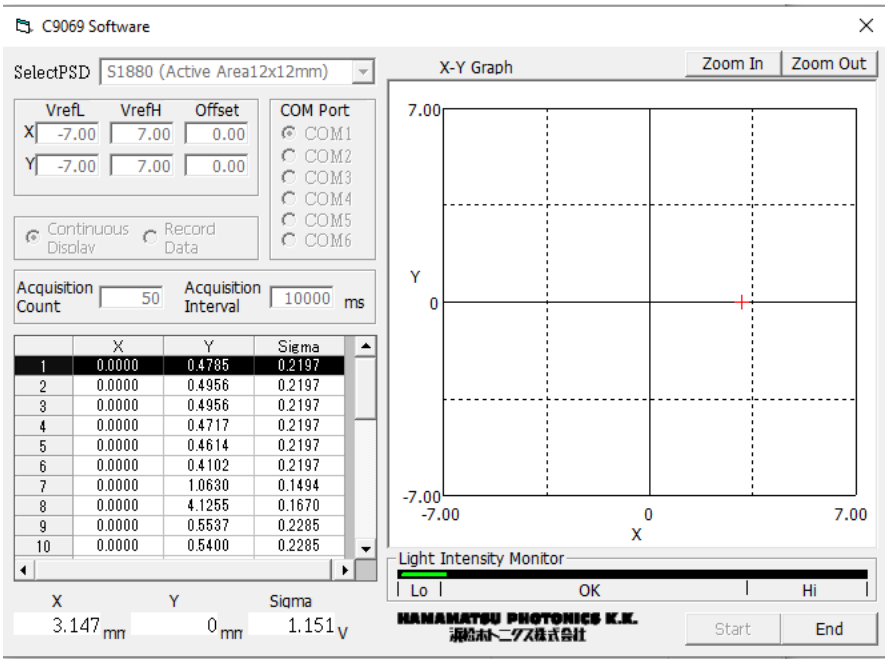

	X	Y	Sigma
1	0.0000	0.4785	0.2197
2	0.0000	0.4956	0.2197
3	0.0000	0.4956	0.2197
4	0.0000	0.4717	0.2197
5	0.0000	0.4614	0.2197
6	0.0000	0.4102	0.2197
7	0.0000	1.0630	0.1494
8	0.0000	4.1255	0.1670
9	0.0000	0.5537	0.2285
10	0.0000	0.5400	0.2285

Figure 4-5: Screenshot of C9069 Software Showing Beacon Laser Centroid on PSD

4.4. CCD and CMOS Imaging Devices

CCD Cameras are excellent choice for beam profiling, analysis and light position detection but have serious setbacks when used in high-speed laser fine beam control and pointing systems. CCD usually have very high resolution/pixels count. At pixel level, CCD possess higher charge-to-voltage conversion efficiency and are suitable for low light level detection. However it is plagued by slow read-out speeds, low frame rates, bulky form factor, demanding computing requirement and higher power consumption. CCD low frame rate induces unwanted time delay to the control feedback loop in FPS and limits the disturbance rejection bandwidth.

Figure 4-6: ThorLabs 340M-USB CCD Camera [126].

4.5. The Photodiode Array Sensor

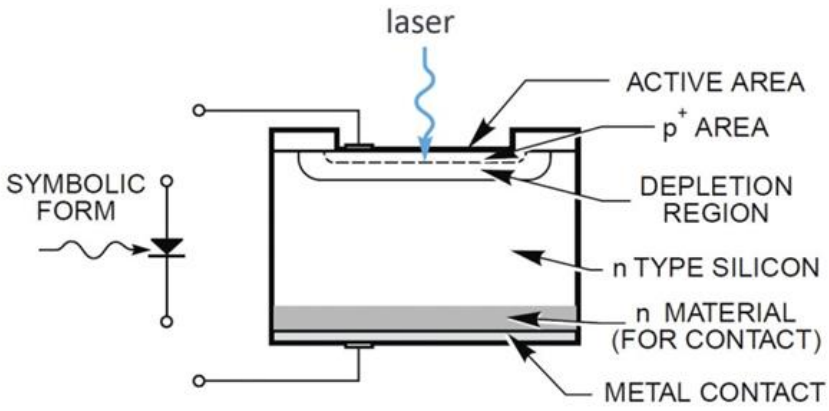

Figure 4-7: Structure of the Photodiode Array. Image source: [127]

Photodiode Arrays are widely used in spectrophotometry (together with Monochromator-prisms/diffraction gratings), clinical and X-Ray scanning systems (with scintillators). Unlimited field of view achievable when using PDA because they are stackable with very minimal panel gaps. Other desirable characteristics of the PDA includes wavelength precision, high sensitivity, reliability, ruggedness, very fast scan speed (depending on microprocessor) and very high signal-to-noise ratio. In this experimental study, an 8 x 8 pixels PDA was selected to monitor the angular displacement of a transmitted laser beam and to support a fine laser pointing controller in the test system constructed. The PDA system comprises of the S13620-02 64-elements two dimensional array, 16 LTC1053 quad precision zero drift buffer amplifiers and 64-to-4 Multiplexer (CD74HC4067) circuit feeding four ADC channels of the microcontroller. The microcontroller clock speed and ADC sampling rate dictates the achievable frame rate of the PDA sensor system. The ATMega2560 microcontroller ADC has 10 bit depth, with reliable sampled values when the ADC input clock is between 50 KHz and 200 KHz.

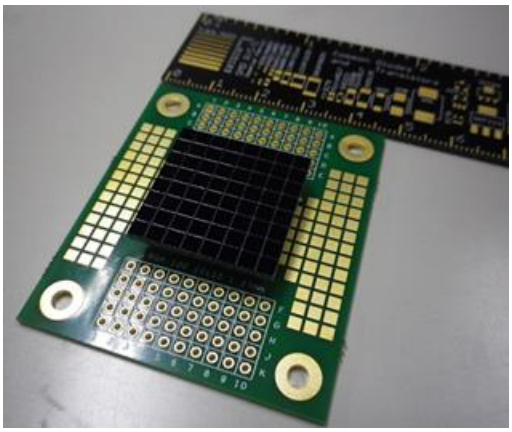

Figure 4-8: Photodiode Array assembled on a BGA adapter

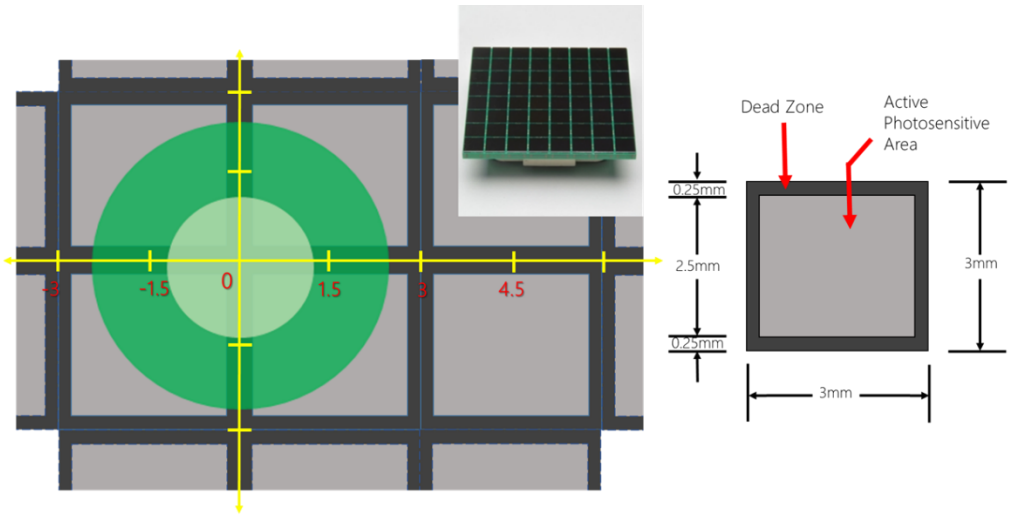

Figure 4-9: PDA aperture and pixel size (Inset: Hamamatsu S13620-02).

4.5.1. The PDA Frontend Electronics

The 64 pixels PDA frame rate of 50fps was recorded when an Arduino Mega microcontroller board (clock prescaler adjusted to 8MHz clock speed) was interfaced with the PDA buffer amplifier and multiplexer. Higher PDA frame rate is easily achievable by utilizing faster microprocessors and dedicated ADC chips such as 24-bits ADAS1127 delivering up to 20kSPS conversion rate. In comparison with CCD camera, the scA-1600 used in the experiment is capable of 14fps but 6 order of magnitude higher resolution than the PDA. The PDA system frame rate must be sufficiently greater than (at least twice) the beam position fluctuation frequency in order to effectively track the beam and support the control system.

4.5.2. PDA Beam Centroiding

The laser beam centroid is defined as the location in-between the 3dB region of maximum intensity where most of the received signal strength is concentrated. The 64 elements resolution array was selected as the primary sensor for optical feedback in the experiment

because higher frame rates can be achieved compared to CCD cameras, effectively trading resolution for faster response speed. However, elemental pixel gaps or dead zones in the array still impacts the overall precision and performance of the PDA. Sub-pixel accuracy also depend on the beam spot size. Frame rate can be related to number of pixels and the digital drive system processing capability. The received laser beam at the PDA surface has a Gaussian distribution with roughly 3mm spot size comparable to the width of each pixel $l_q = 3mm$ of the PDA. Half of the beam's intensity is concentrated within the Full Width at Half Maximum (FWHM), hence centroid calculation was simply implemented using the Center-of-Gravity (CoG) algorithm expressed in equation (4-1), having the benefit of lower computing power requirement [128].

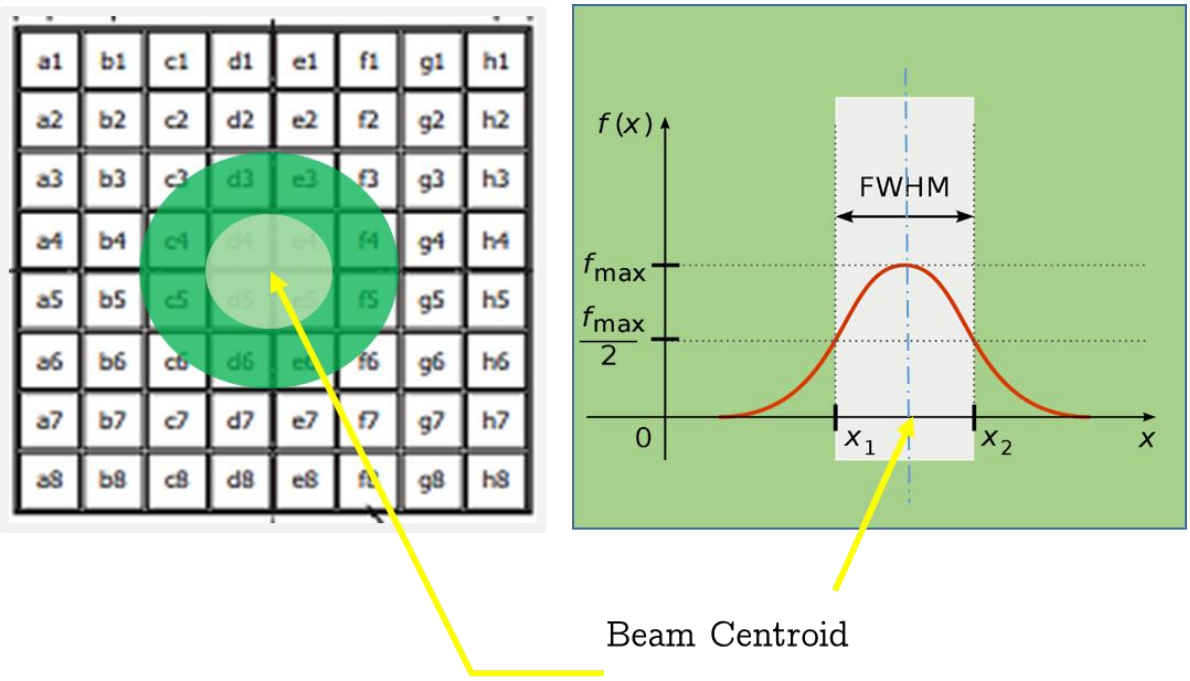

Figure 4-10: Illustration of laser beam centroid and PDA pixels

$$(x, y) = 4l_q\left\{\frac{\sum X_{ij}I_{ij}}{\sum I_{ij}}, \frac{\sum Y_{ij}I_{ij}}{\sum I_{ij}}\right\} \tag{4-1}$$

Quadrant Detectors (2x2 array) and Position Sensitive Devices (PSD) are commonly used for laser beam displacement measurement but have limited aperture size making them unfitting for sensing larger angular displacements without the use of additional optics. Beam centroid using QDs are done by continuous sampling of the currents from the four photodiode's quadrants as in equation (4-2). The PDA can also be modeled as a stack of multiple QDs to enable wider aperture sensing.

$$(\Delta x, \quad \Delta y) = 4\left(l_q\left\{\frac{(I_A + I_D) - (I_B + I_C)}{I_A + I_B + I_C + I_D}\right\}, \quad l_q\left\{\frac{(I_A + I_B) - (I_C + I_D)}{I_A + I_B + I_C + I_D}\right\}\right) \tag{4-2}$$

4.6. Fine Steering Mirrors

Fine steering Mirrors (FSM) are miniature actuators that deflects an incident laser beam by an angular deviation proportional to the applied current. Generally, FSMs are categorized as electromagnetic-type, piezoelectric-type and the voice coil type. The piezo type have very high response but often require higher drive voltages. The voice coil types tends to be bulkier and are not attractive for adaption into lean platforms. The S12237-03P is an electromagnetic-type Micro-electromechanical (MEMS) Fine Steering Mirror operated by applying a current source to its coil which has a typical resistance of 165Ω at room temperature. Because the coil resistance is susceptible to change due to the ambient temperature variations, a grounded load voltage to current converter ensures that actuation current is unaffected by these environmental changes. An upper limit of θ_{fsm}=15° optical deflection angle and 100Hz drive frequency was recommended by the device manufacturer. Therefore, R1 to R4 = 333.3Ω were selected for a V_{dd} = 5V DAC reference. The maximum drive frequency sets the bandwidth of the platform disturbance rejection.

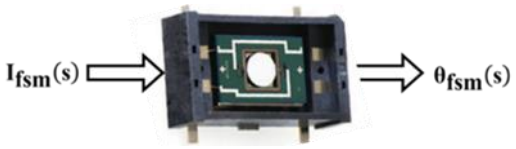

Figure 4-11: Hamamatsu S12237-03P FSM.

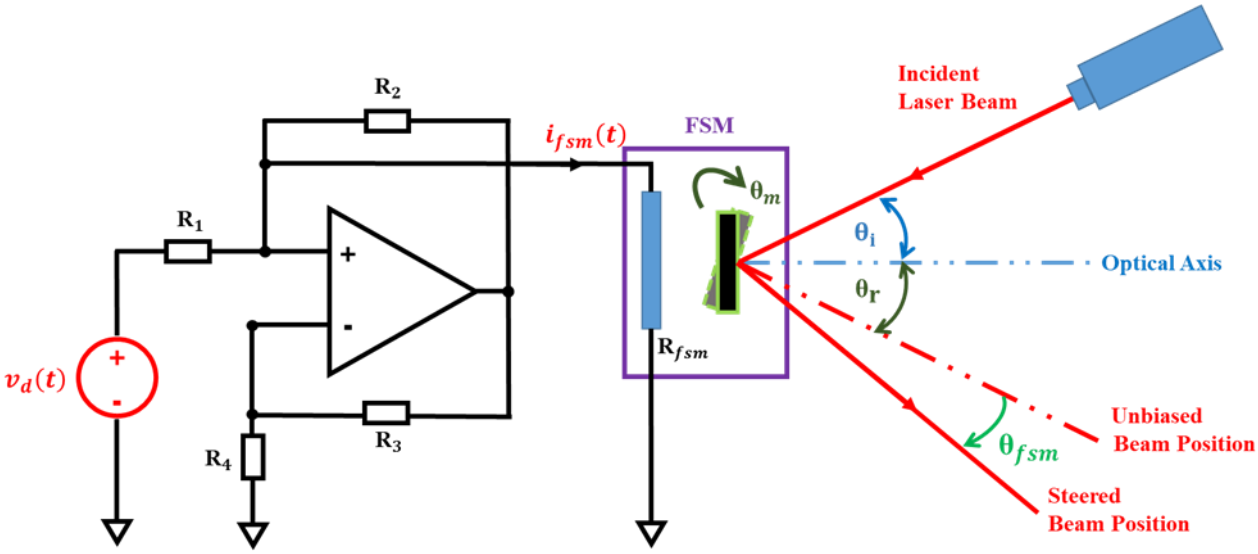

Figure 4-12: Operating principle of the MEMS FSM driver.

$$V_d(t) = v_{dd}\frac{D_{nr}}{(2^n - 1)} \; ; n = 12bits \tag{4-3}$$

$$i_{fsm}(t) = \frac{v_d(t)}{R_1} \tag{4-4}$$

The FSM optical deflection angle is always twice the mechanical angle, θ_m with good linearity when driven between -15mA to 15mA as expressed in equation (4-5).

$$\theta_{fsm}(t) = 2\theta_m = i_{fsm}(t) \times 1000 \tag{4-5}$$

Equation (4-6) to (4-9) are the Plant (FSM) transfer function with its complex response; amplitude and phase lag expressed with respect to the drive frequency, resonant frequency (530Hz) and the device Quality factor, Q = 30.

$$G_{fsm}(s) = \frac{I_{fsm}(s)}{\theta_{fsm}(s)} \tag{4-6}$$

$$G_{fsm}(\omega) = |G_{fsm}(\omega)|e^{\arg\{G(\omega)\}} \tag{4-7}$$

$$|G_{fsm}(\omega)| = 1 + \left(\frac{\omega}{530}\right)^2 \tag{4-8}$$

$$arg\{G(\omega)\} = tan^{-1}\left\{\frac{530\omega}{\boldsymbol{Q}(280900 - \omega^2)}\right\} \tag{4-9}$$

(4-10)

MATLAB System Identification Toolbox was utilized to obtain the Plant's poles-zero gain mathematical model:

$$G_{fsm}(s) = \frac{1.037S + 103.8}{S + 101}$$

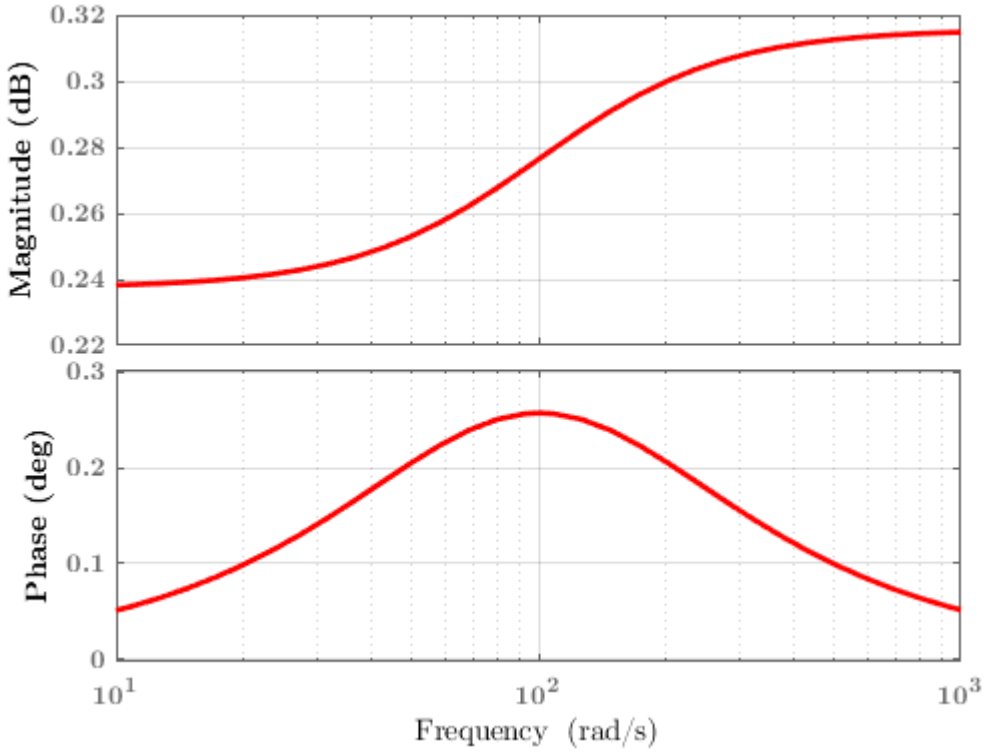

Figure 4-13: FSM open-loop frequency response.

4.6.1. FSM Open-Loop Response

The FSM was operated to switch an incident laser beam between two APDs separated at a known beam angular displacement (5°) to validate the accuracy of the fine steering mirror. The Arduino-based FSM Controller was programmed to retain the beam at APD1 and APD2 positions for 2s and 3s respectively. Figure 4-15 shows the sampled ADC voltages of the APDs in response to the beam movements. The spikes in the curves represents the background noise at the aperture of the detectors.

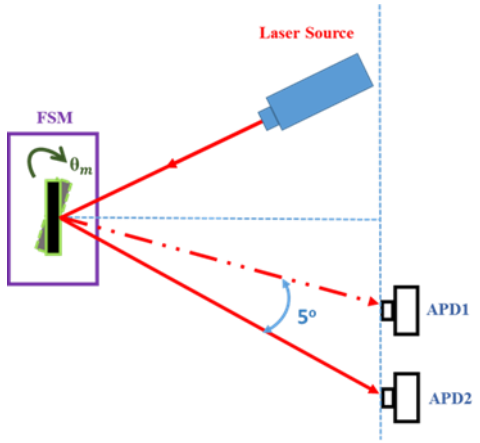

Figure 4-14: APDs setup

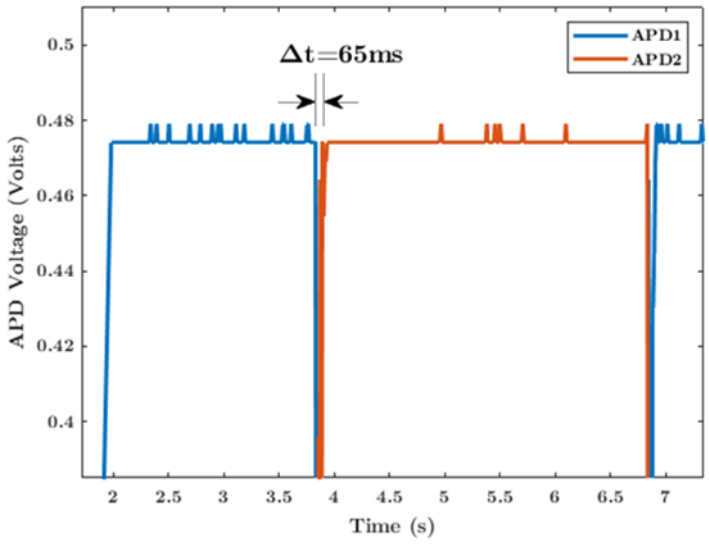

Figure 4-15: Beam switching response

4.7. Feedback Beam Control

A Proportional-Integral (PI) Controller was designed in Simulink to drive the FSM in a single-loop mode (i.e. using only PDA feedback). Optimal values of the proportional Kp, and integral Ki control gains were designed in Simulink for a stable control system with no

overshoot and minimal rise time (5ms) to achieve close-loop bandwidth of 100Hz. The MPU6050 device gyroscope and accelerometer maximum bandwidths were specified as 8 KHz and 1 KHz respectively in the device manual [20]. In the experiment, the platform was subjected to vibrations at different linear acceleration and displacement values for only the single mode. Figure 4-17 shows the simulated response to a sinusoidal external vibration with a sinusoidal profile of 4 degrees amplitude and 5 Hz frequency with 0.5s step time of the SetPoint.

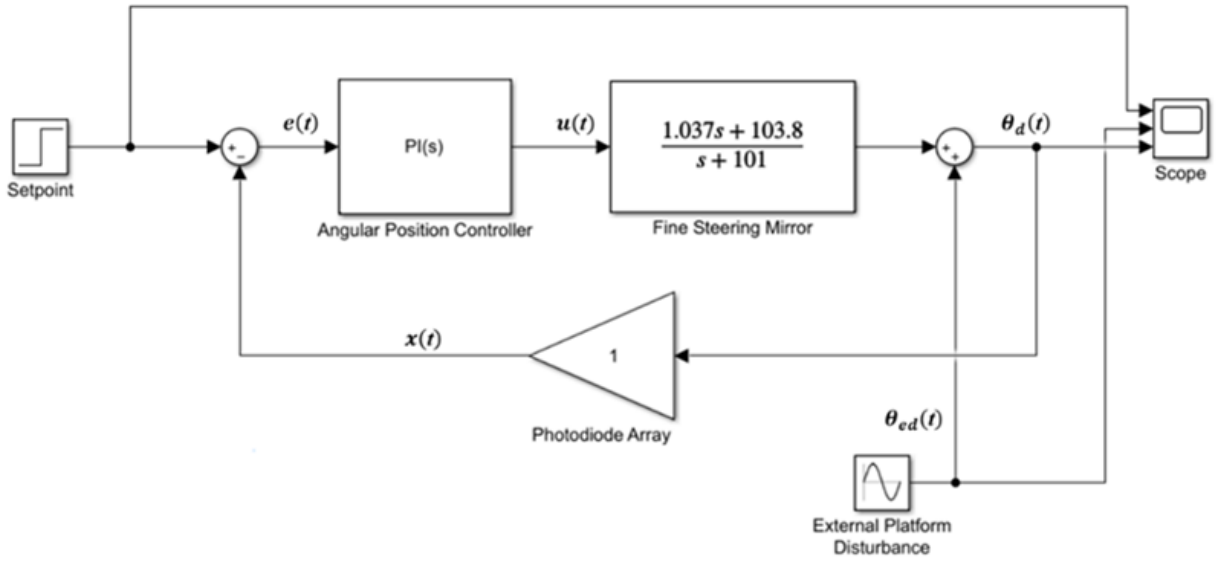

Figure 4-16: PDA single-loop feedback control model

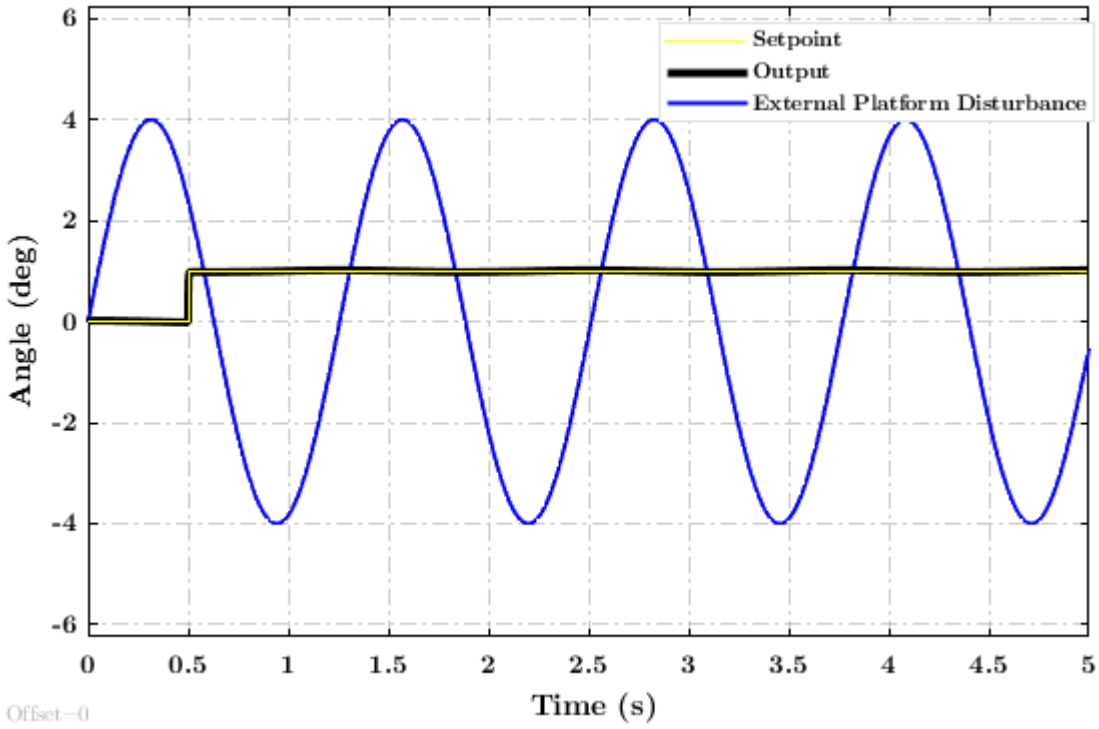

Figure 4-17: Simulated controller response to setpoint and sinusoidal disturbance profile.

The controller output oscillated by about the same frequency but its amplitude constrained to the SetPoint value (expected beam position) which was adequate to keep the laser link within the APD's field-of-view. Driving the FSM at values closer to its mechanical resonant frequency produces severe inaccuracies and instability because the optical deflection angular error and phase lag increases with Controller's output frequency. The Hamamatsu S12237-03P FSM can be reliably operated at 100Hz in linear mode, hence setting a limit for the system's vibration disturbance bandwidth. The choice of FSM is therefore based on the prior knowledge of the expected platform jitter bandwidth and sampling rates of the feedback sensors.

4.8. Multi-loops Feedback Beam Control

Multi-loops feedback control enables the use of several sensors to optimize the precision of the beam control system. The quality and response of the Controller is dependent on the information provided by sensors continuously monitoring internal and external conditions that affects the system. In the double-loop control mode featuring the PDA and accelerometer feedbacks, the accelerometer is positioned in the inner loop because of its high bandwidth. However, the reverse will be the case if the sampling rate of the PDA exceeds the output rate of the accelerometer.

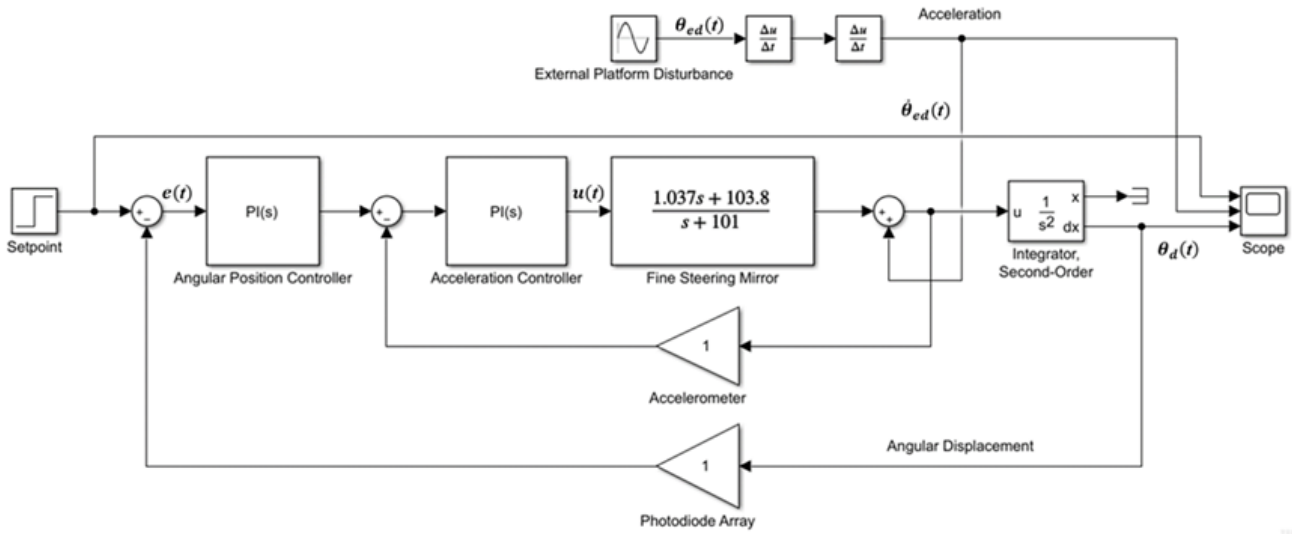

Figure 4-18: PDA and accelerometer double-loop feedback model.

4.9. Experimental Application of PDA for Feedback Beam Control

The objective of the beam steering experiment was to test the performance of the FSM feedback Controller using the PDA in suppressing the induced platform disturbances at varying vibration profiles. The transmitter setup consisting of the laser source, FSM, inertia sensor and Controller were firmly assembled on a mini-optical breadboard attached to a rail. The rail was firmly attached to an adapter jig on top of the vibration machine's slip table. The vibration machine is an industrial grade test system used for satellite qualification tests. The machine is

capable of generating vibrations of up to 2 KHz and 10cm linear displacement covering most of satellite launch and on-orbit jitter spectrum. The receiving and feedback systems were assembled on a small optical bench placed on a moveable trolley. At first, the platforms were arranged such that the laser beam was perfectly aligned with the axis of the PDA and APD sensors. Hence the position of the platforms were fixed while only the vibration machine altered the attitude of the stabilized transmitting setup in the x-axis direction. The two sections were completely mechanically isolated, the XBee radio feedback link also eliminated the need for cabling between them. During the vibration experiment, the transmitter platform was subjected to different acceleration movements to check the PDA feedback alignment error and FSM Controller responses. The test apparatus illustrated in Fig. 4-19 consists of transmitting and receiving sections mechanically isolated from each other to emulate the case of distant laser communicating platforms as much as possible. The FSM and accelerometer sensors were collocated in order to track the attitude changes of the transmitting platform and hence the beam due to induced vibrations. Both the optics and associated electronic circuitries are mounted on a rail for easy positional adjustments and coupling with the vibration generator. A mini-optical bench placed on top of an adjustable-height trolley host the receiving optics, thus enabling flexibility in aligning the systems. The sections were optically aligned such that in the absence of movements or disturbances, the receiving APD (ThorLabs' SM05PD3A) and the PDA sensor (Hamamatsu S13620-02) registers the maximum signal strength and zero angular beam displacement respectively. The APD was interchanged with a CCD Camera for profiling the beam characteristics.

A 1mW laser source with an in-built collimator generated Ø3mm visible beam directed to the Hamamatsu S1227-03P MEMS Fine Steering Mirror. The laser diode was driven directly and also by an amplitude modulated circuit when transmitting test signals over the laser link. A low cost Commercial off-the-shelf (COTS) Arduino ATMega2560 microcontroller at the heart of the control circuitry receives feedback signals from an XBee radio link as well as continuous attitude data stream from MPU-6050 (3-axis Accelerometer and 3-axis Gyroscope) Inertia Measurement unit while executing the FSM control algorithm.

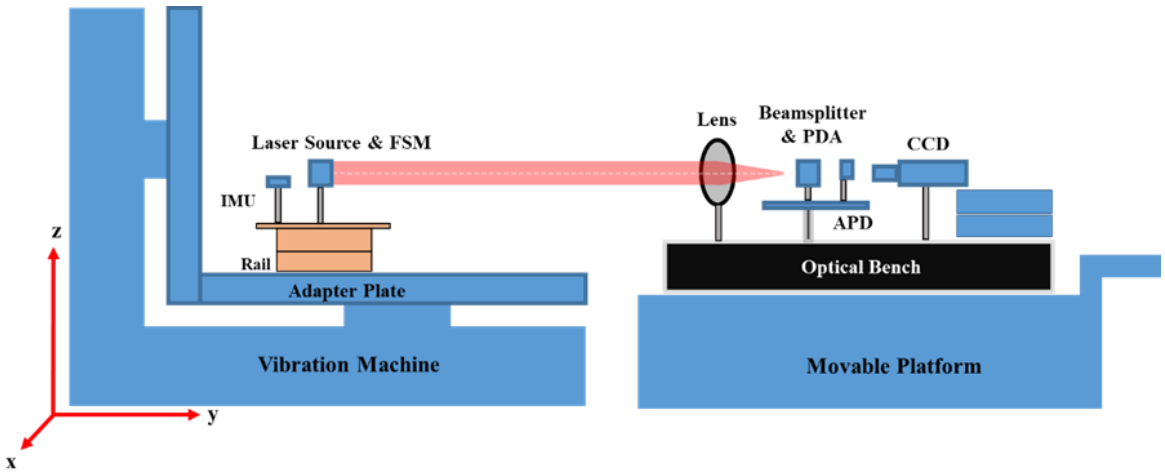

Figure 4-19: Layout of Vibration Machine Test Setup.

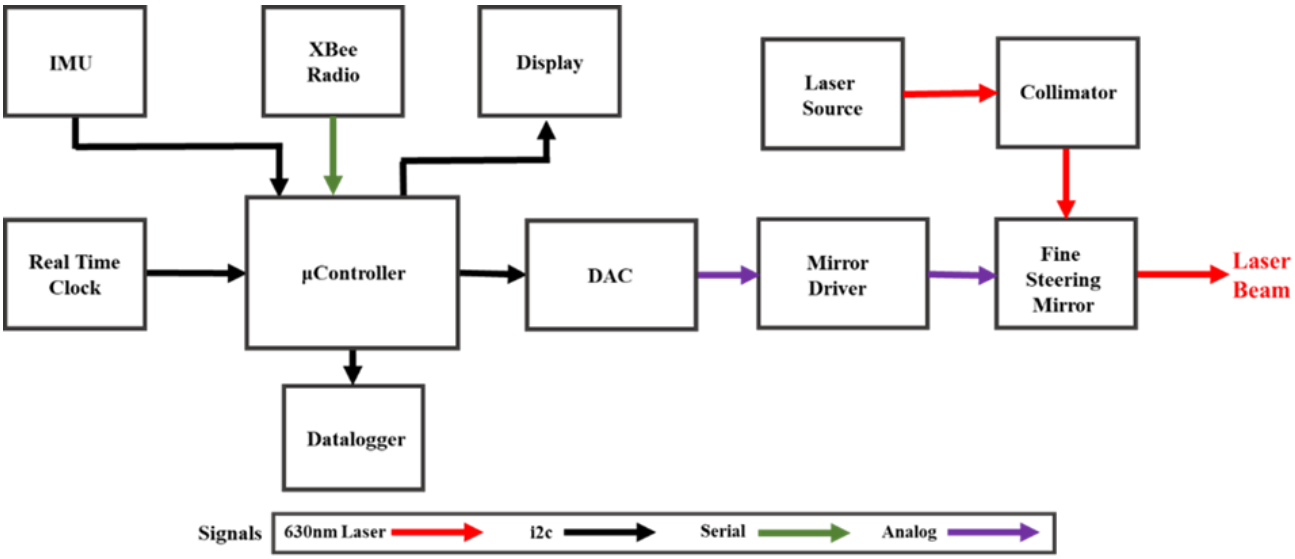

Figure 4-20: Block diagram of the transmitting section.

The Controller's digital voltage output was connected to MCP4725, a 12-bit resolution digital-to-analog converter (DAC) and feedthrough to the Mirror driver (LM324 quad-opamp voltage to current converter and monitor circuit). The Real time clock (RTC), LCD and datalogger also on I²C bus enables real-time visualization and recording of the system data during the vibration tests. A Cubic Beamsplitter divides the received laser beam equally between the receiving APD/CCD Camera setup and the Photodiode Array Sensor system positioned 45° to each other on the optical bench. The beam's centroid and angular displacement across the aperture of the PDA is computed by the microcontroller which then routes the information back to the transmitter's FSM controller via the XBee radio link. Similar to the transmitting section, a datalogger records the system information during the experiments. When a sufficient disturbance is applied to the transmitter platform, the beam position around the APD aperture fluctuates in proportion to the disturbance resulting to intermittent communication link outages. However, the PDA sensor continuously captures the angular deviation information needed for the FSM Controller to return the beam to the desired APD position.

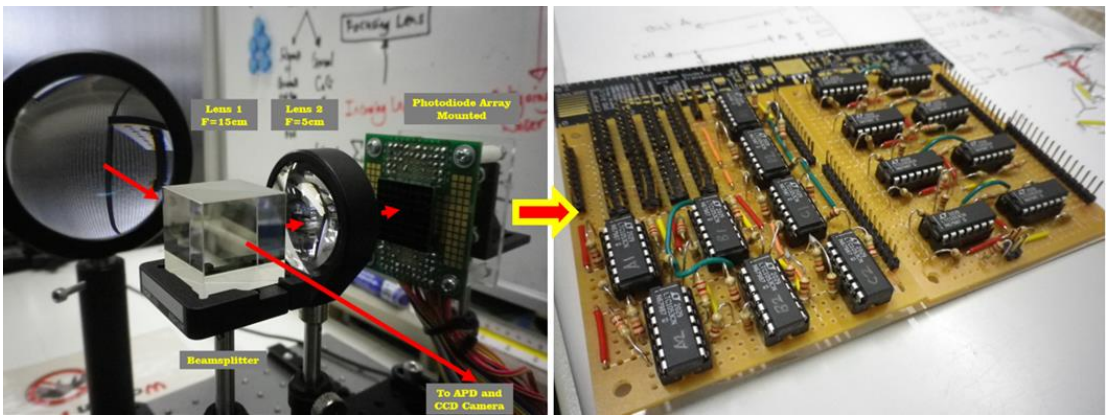

Figure 4-21: Receiver optics with mounted PDA and Buffer-amplifier board.

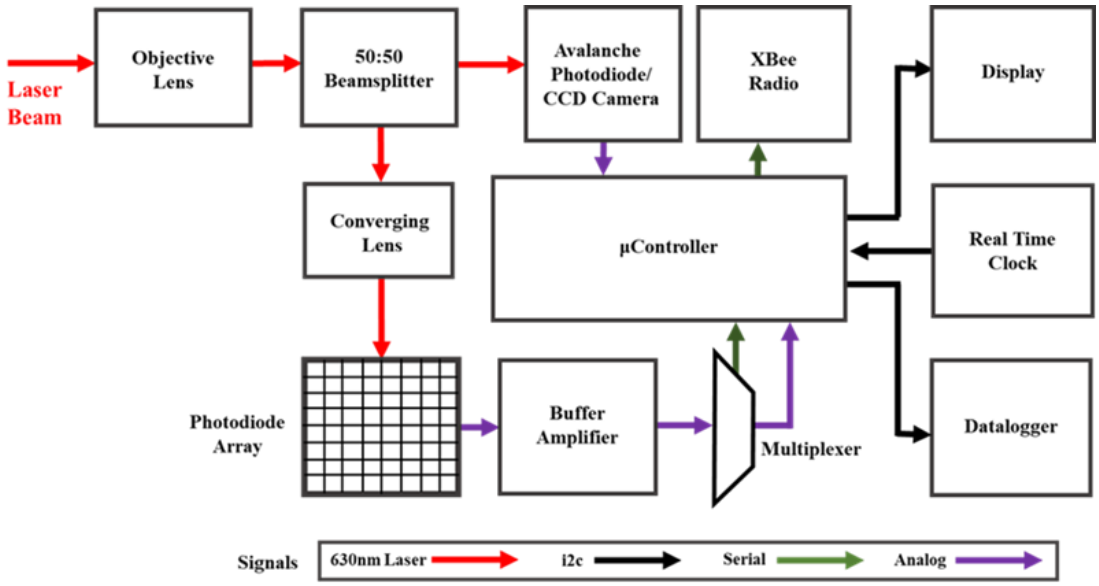

Figure 4-22: Block diagram of the receiving section.

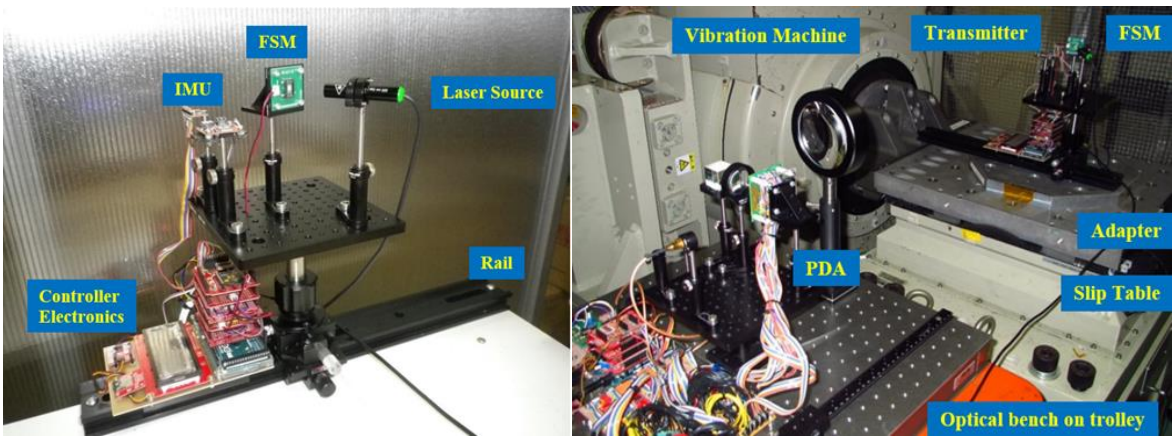

Figure 4-23: Prototype of FSM controller and receiver integration on vibration machine.

In the closed-loop operation mode, the beam angular displacement values computed using the PDA sensor was relayed to the Controller at the laser transmitter side. Therefore the FSM was constantly actuated automatically to suppress the vibration profiles by deflecting the beam to the desired angular setpoint (2.5°). Figure 4-25 shows the PDA response and the feedback controller effort.

Table 4-1: Experiment vibration test profiles

Vibration Machine Profiles	*Accell. (G)*	*Set Mean Freq. (Hz)*	*Linear Displacement Amplitude (mm)*
Profile A	0.25	5.00	5.00
Profile B	0.50	5.00	10.00
Profile C	0.75	5.00	15.00
Profile D	1.00	5.00	20.00

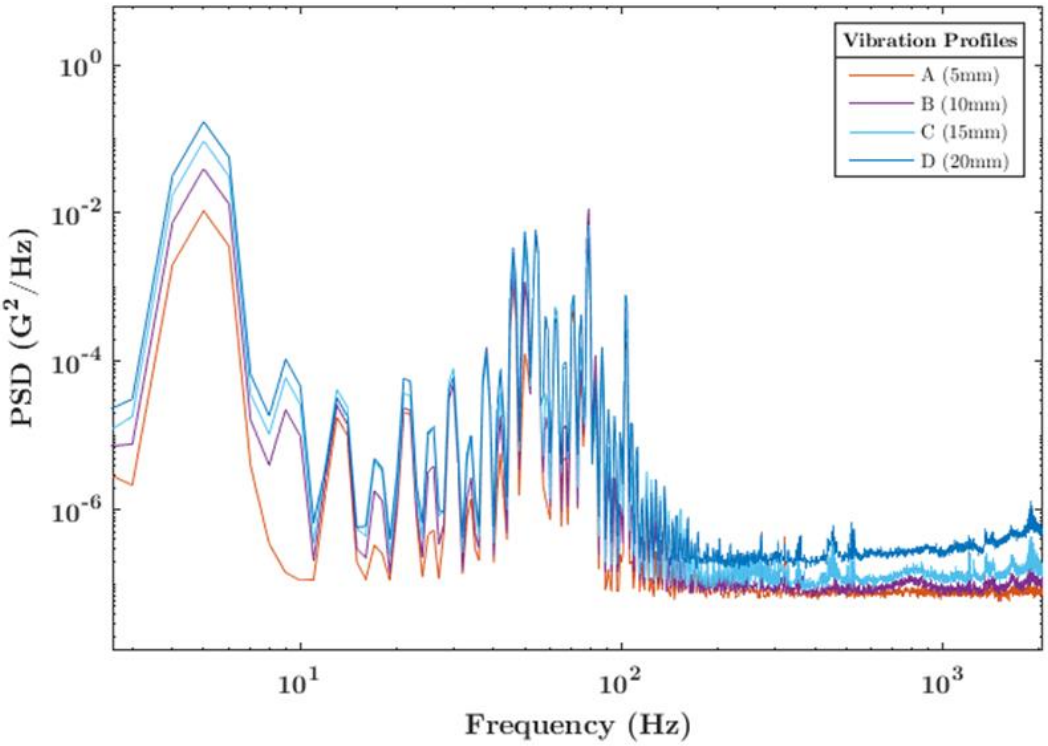

Figure 4-24: Frequency spectrum of vibration profiles at FSM and Accelerometer position.

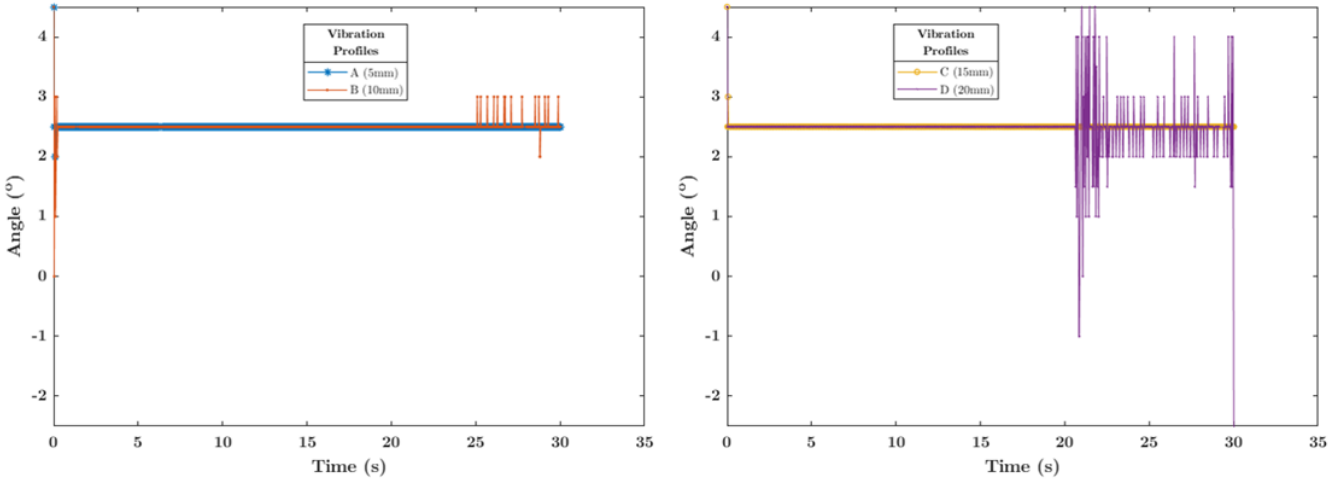

Figure 4-25: Closed loop beam stabilization under vibration machine disturbances.

The Controller steered the beam adequately in the Profiles A, B and C but was less effective in Profile D perhaps due to the larger displacement of the slip table, microcontroller performance and the XBee feedback channel. The overlapping flat lines in the plots shows that the laser beam was stabilized for over 20 seconds despite the induced fluctuations by the vibration machine. In these periods the PDA circuitry sends back continuous streams of beam angular error to the FSM controller. This demonstrated that a lower resolution PDA sensor can effectively substitute CCD cameras in feedback beam control for low resource platforms.

4.10. Limitations of the PDA

The elemental gaps (though narrow) and dead zones impacted the precision of dynamic laser beam centroid computation. Nevertheless, a more efficient centroiding algorithms such as the best-fit to Gaussian approach could possibly enhance the detection accuracy of the photodiode array sensor and consequently the performance of the fine steering control system.

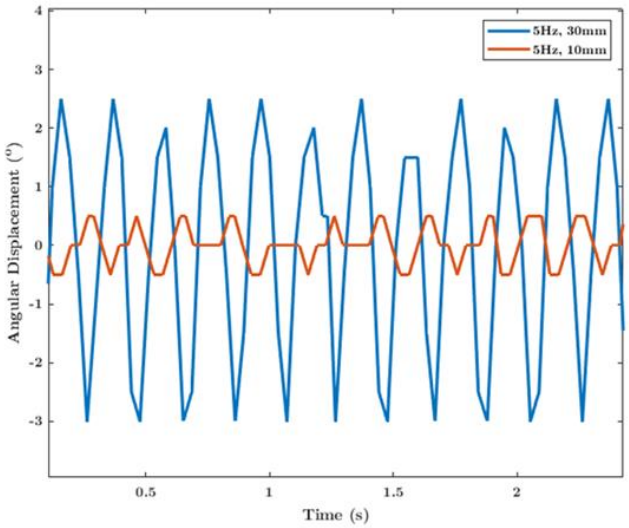

Figure 4-26: Open loop response to vibration machine disturbances

5. CUBESAT JITTER EFFECTS ON LASERCOM BEAM POINTING STABILITY

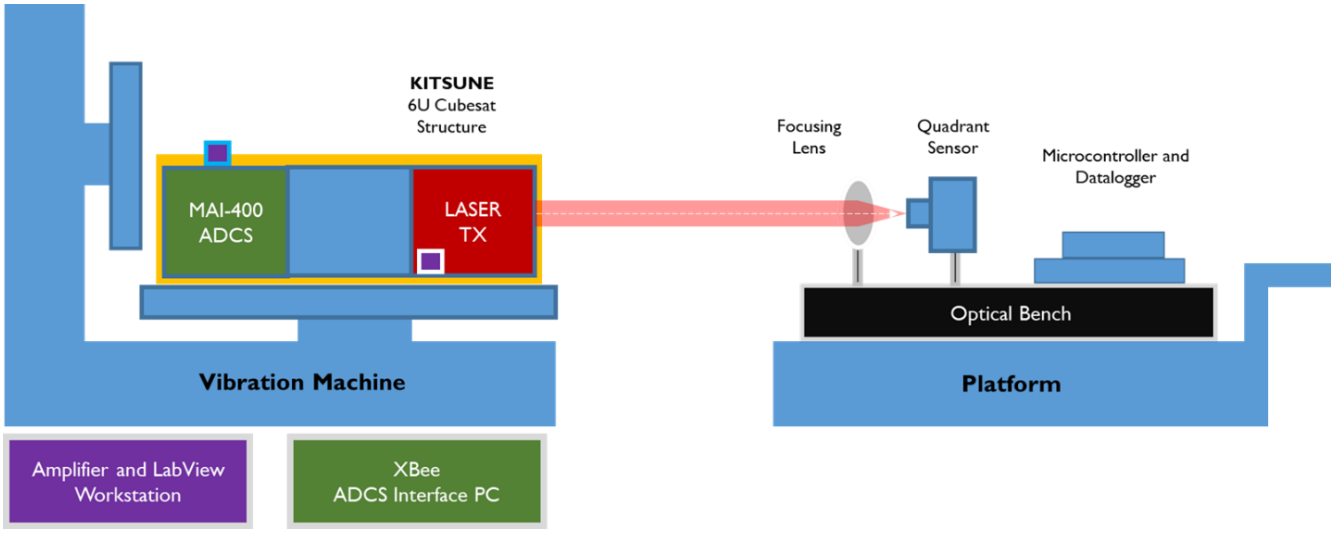

Figure 5-1: CubeSat Jitter Experiment Layout

Direct line-of-sight laser communication links require a very stringent beam-pointing stability, since they are easily perturbed by attitude variations and micro-vibrations generated by the host platform's propulsion system or other mechanically active subsystems in close proximity with the transmitter's optical head. Severe line-of-sight jitter causes a laser beam to drift from the target receiving optics position, inducing pointing errors, increasing signal outage probability and loss of transmitted information. In this Chapter, CubeSat platform jitter generated by the attitude-control unit's reaction wheels assembly (RWA) in a 6U CubeSat structure is examined. Experiments to determine the vibration spectrum are discussed. Requirements for applicable optical fine pointing and disturbance isolation or suppression systems needed to achieve a high-fidelity laser-communication link are also presented.

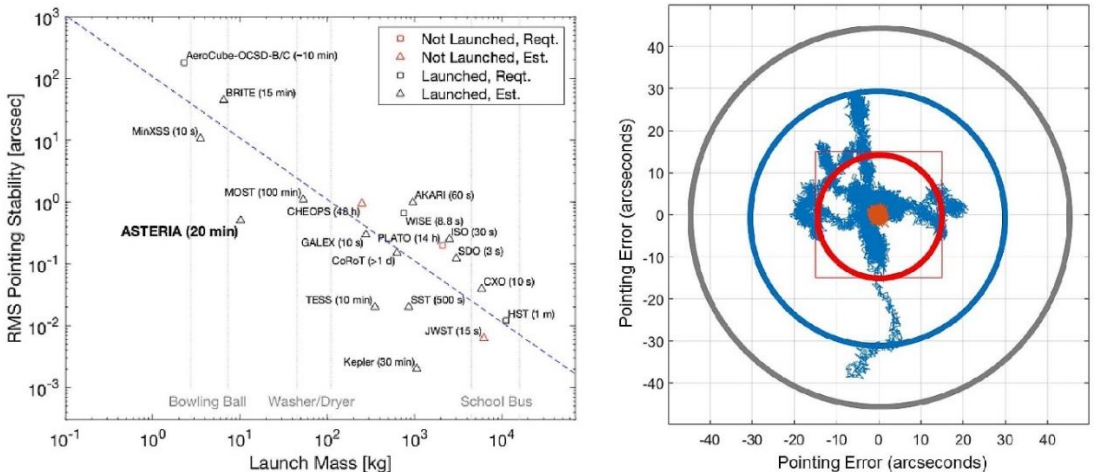

(a) (b)

Figure 5-2: (a) Optical Pointing Stability of Various Missions (b) ASTERIA Pointing Performance. Sources:[129][130]

5.1. Analysis of CubeSat RWA Micro-Vibrations

Micro-vibrations in satellites are structurally transmitted force disturbances originating from subsystems (such as reaction wheel assembly, control moment gyroscopes, servomotors, antenna drive mechanisms etc.), and appendages of the platform [131][132]. Micro-disturbances are generated chiefly by the satellite reaction wheels, perturbing the host instrument or payload line-of-sight pointing stability. The reaction wheel assembly produces micro-disturbances due to static and dynamic imbalances, bearing friction, manufacturing imperfections and operational degradation. Static imbalance is a misalignment of the wheel's center of gravity from its rotation axis while dynamic imbalance can be defined as the cross product of the wheel's inertia caused by angular deviation of the principal inertia with respect to the spin axis. The vibrations emanating from the RWA can be modeled in analytical, empirical and hybrid forms [133]. Hybrid model is the combination of the first two. These models rely on the manufacturer's design specification and experimental test data, however, most user manuals do not include complete information needed to forecast the jitter impact on mission payloads [134]. Hence, practical experiments aiming to characterize the impact of the RWA force export on a laser pointing setup were conducted and detailed in the foregoing sections.

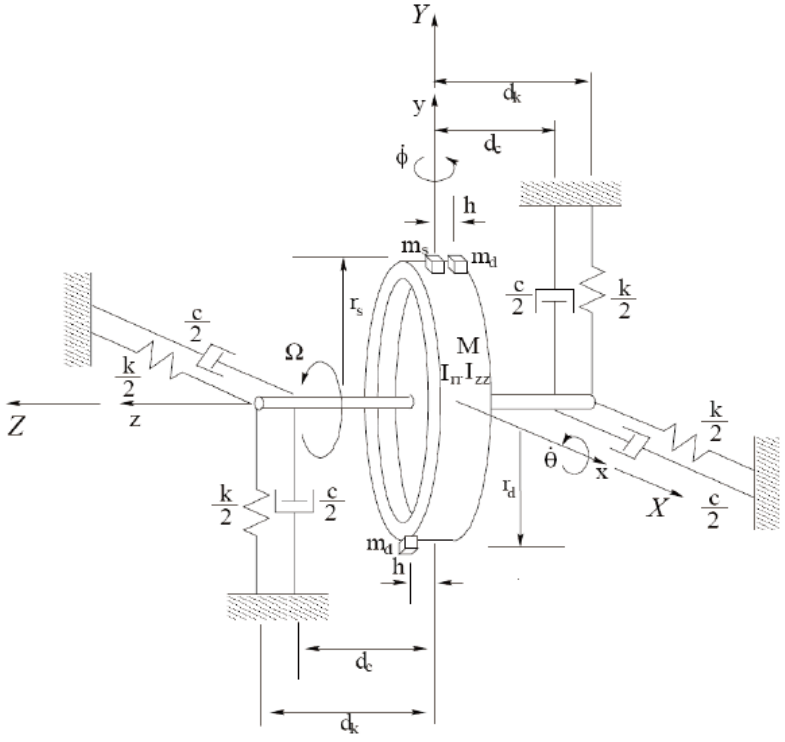

Figure 5-3: Analytical reaction wheel model with imbalance. Source: [135] [136]

5.2. CubeSat Jitter Spectrum Measurement Experiment

5.2.1. RWA Experimental Test-bed

An experimental test-bed was assembled to determine the spectrum of jitter induced by the MAI-400 reaction wheel, with a line-of-sight laser transmitter in a 6U CubeSat (KITSUNE satellite) structure. Axial acceleration and gyroscope data from the ADCS internal sensors where obtained via an XBee radio interface with a computer. High fidelity piezo accelerometers interfaced with amplifier setup measures the micro-vibration from the laser transmitter FSM location and a body of the reaction wheel. In order to monitor the effects of the vibrations at different reaction wheel speed, an optical beam position sensing system was incorporated as shown in Figure 5-2 below.

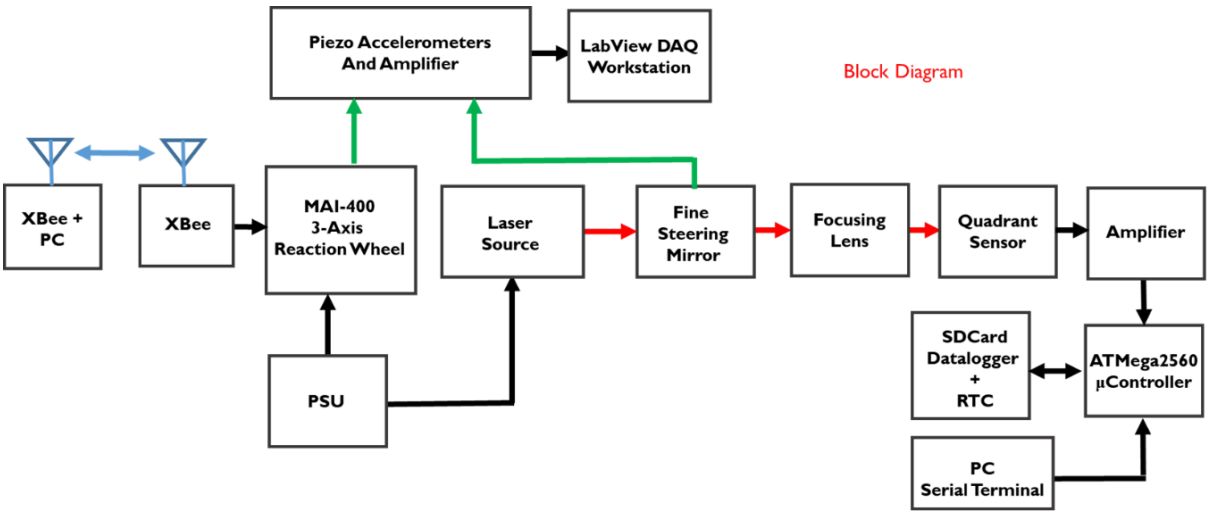

Figure 5-4: Block diagram of the experimental test-bed

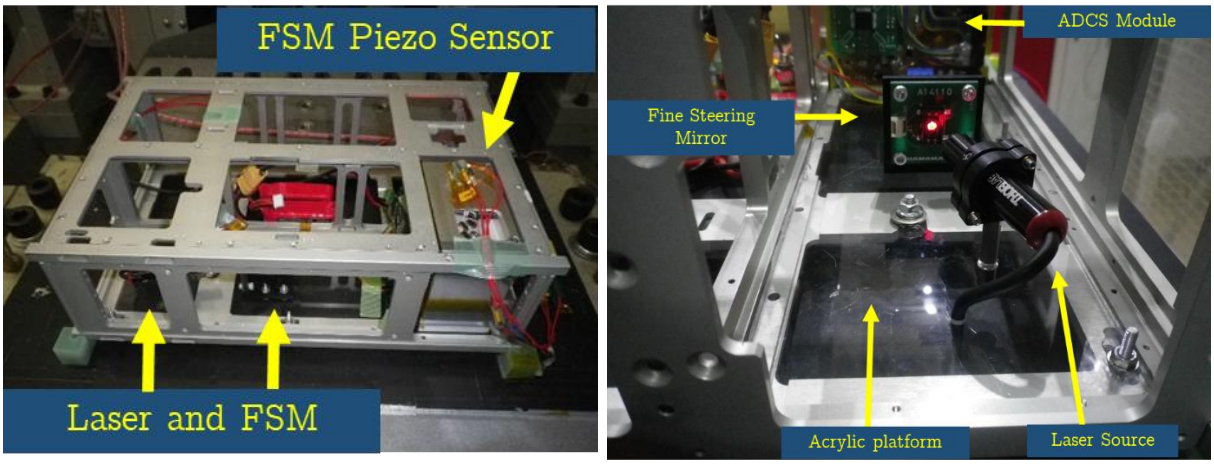

Figure 5-5: Sensors Placement

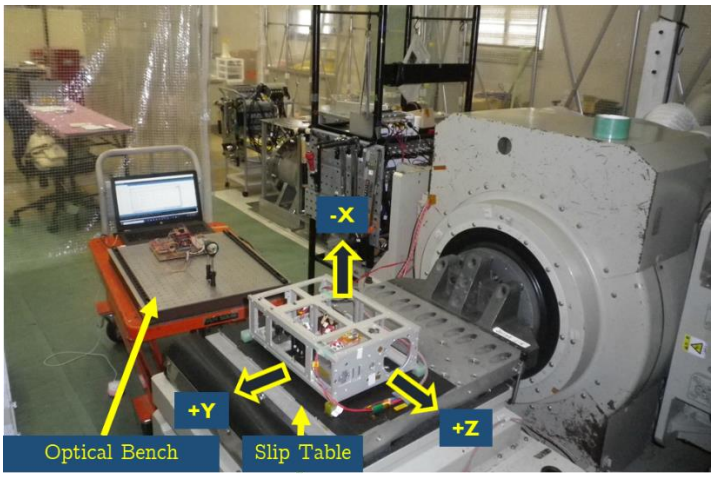

Figure 5-6: Integration of Piezo accelerometer and amplifier to positions on the CubeSat structure

5.2.2. MAI-400 ADCS Operation

The ADCS module reaction wheel speed was incremented in steps starting from off position to its full capacity (10,000rpm) in order to examine the impact on the magnitude of force projected to the optical components as well as the resultant instability of the laser beam. The internal accelerometer and gyroscope simultaneously recorded the dynamics at each steps.

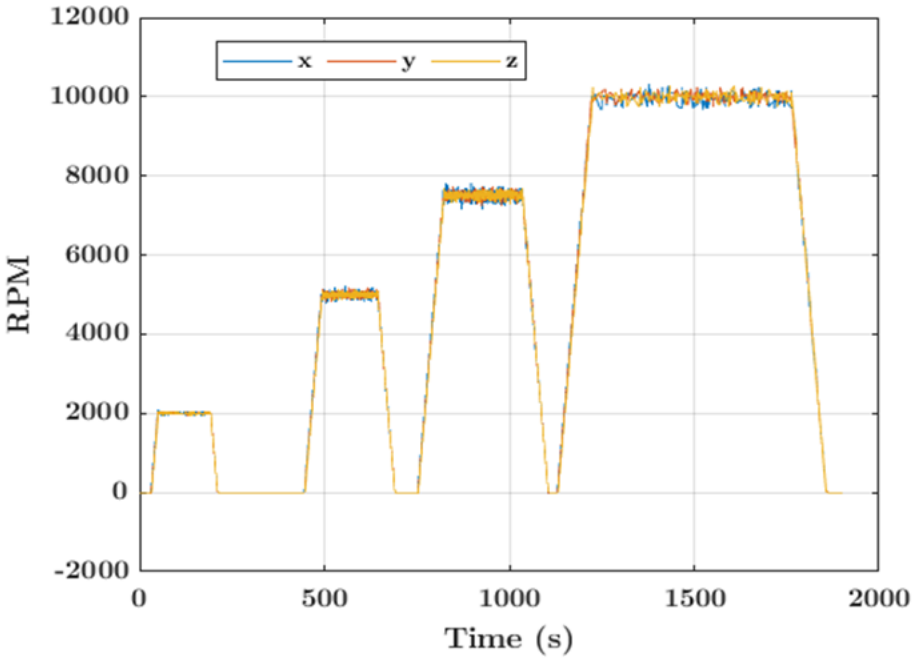

Figure 5-7: ADCS Tachometer profile

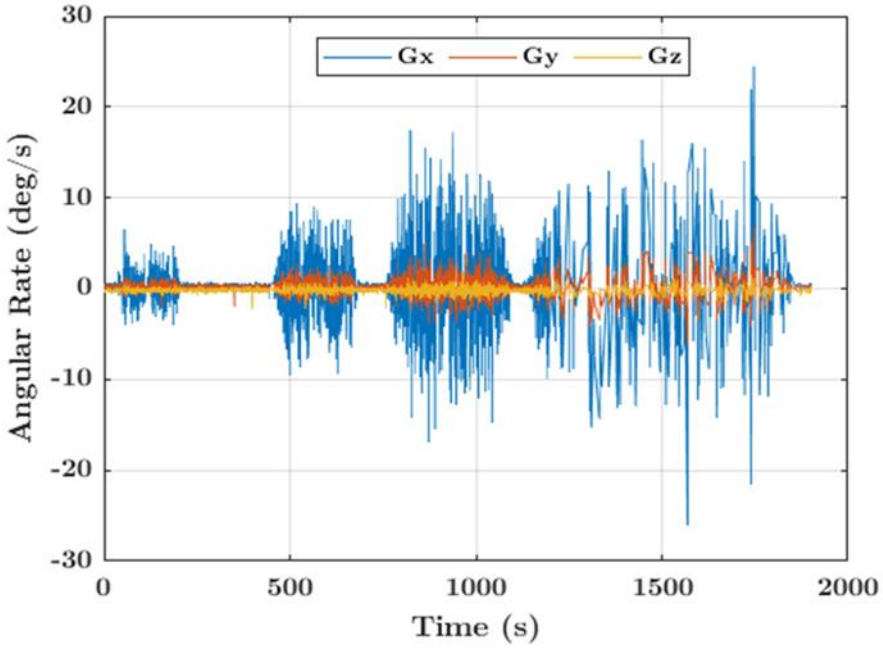

Figure 5-8: ADCS Gyroscope

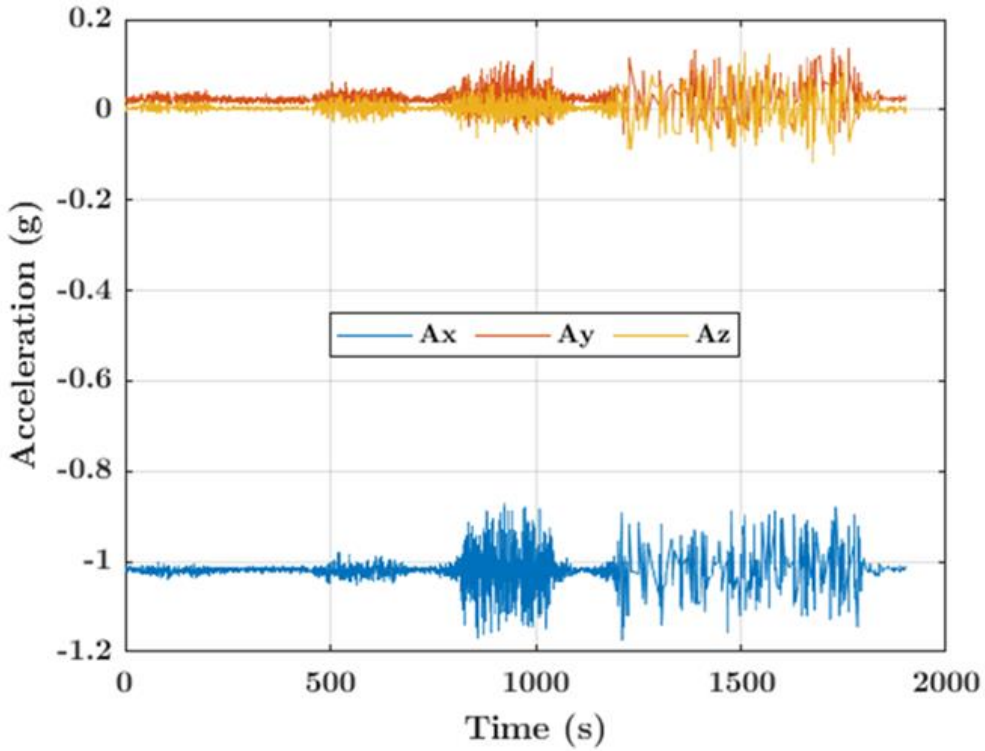

Figure 5-9: ADCS Accelerometer

5.2.3. Piezo-accelerometer Sensor Measurements

Three piezo accelerometers were mounted on a small cube and attached to the FSM location and ADCS location interfaces the pre-charge amplifier. The pre-charge amplifier converts the piezo-electric type accelerometer high impedance charge input into a low impedance voltage signal [137] fed into a LabView data acquisition system. Figure 5-8 shows the legend of the sensor orientations.

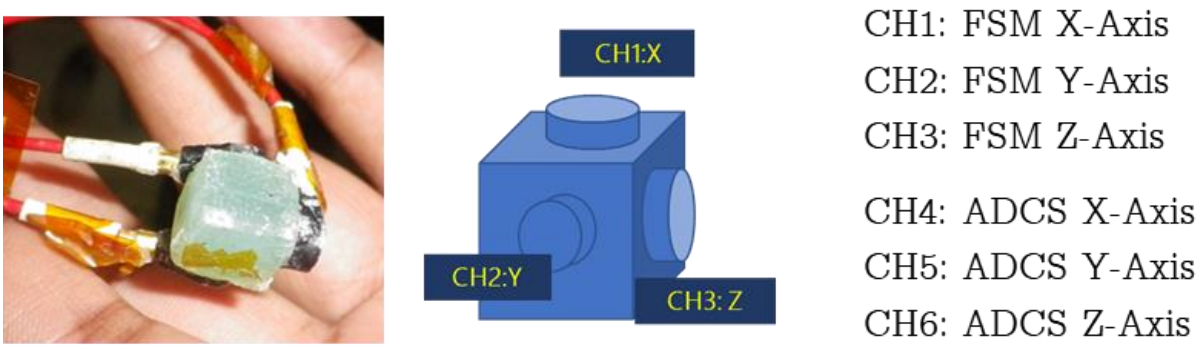

Figure 5-10: Piezo Accelerometer sensor placement and axes

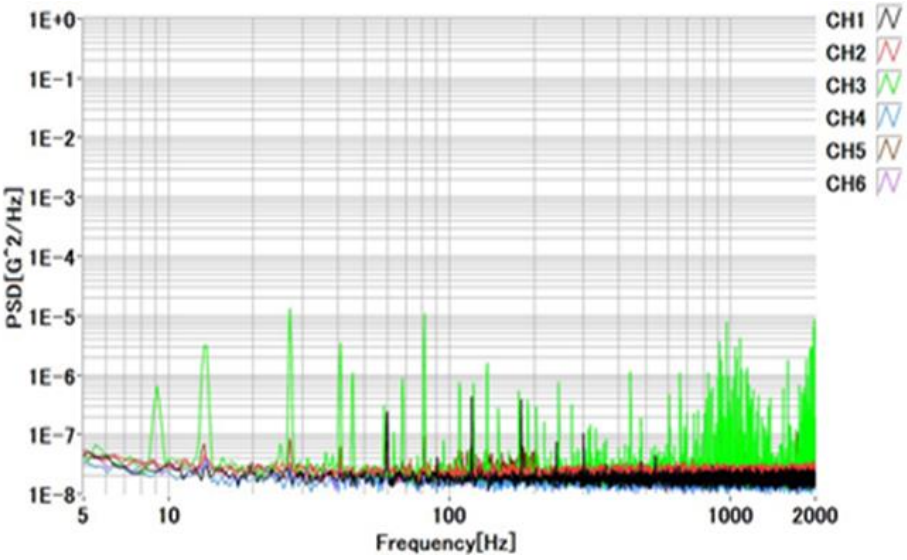

Figure 5-11: Vibrations at 0 rpm

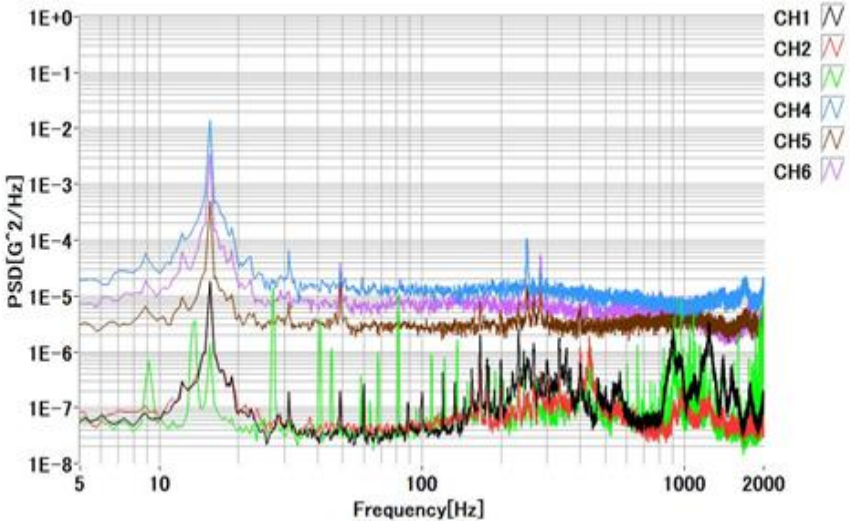

Figure 5-12: Vibrations at 2000rpm

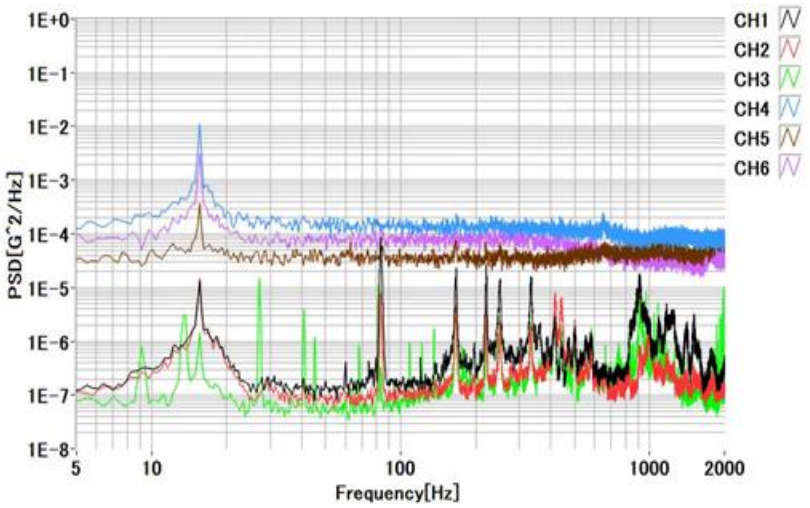

Figure 5-13: Vibrations at 5000rpm

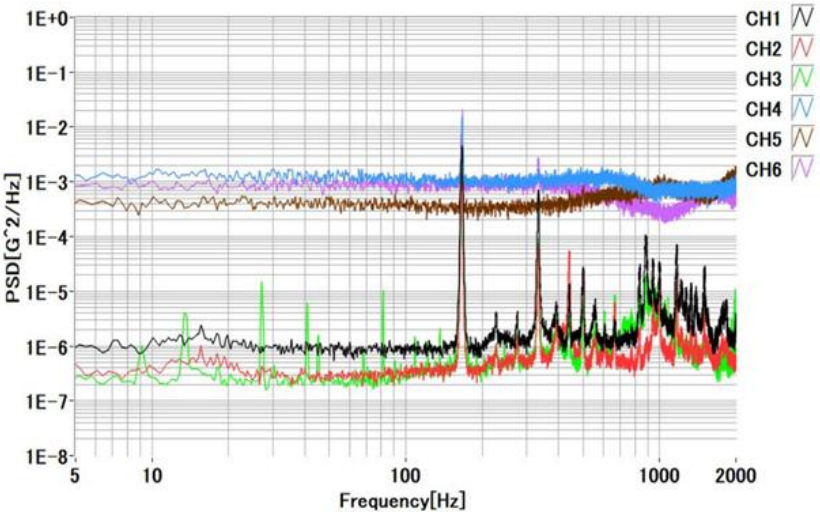

Figure 5-14: Vibrations at 10000rpm

5.3. Jitter Impacts on Beam Alignment and Stability

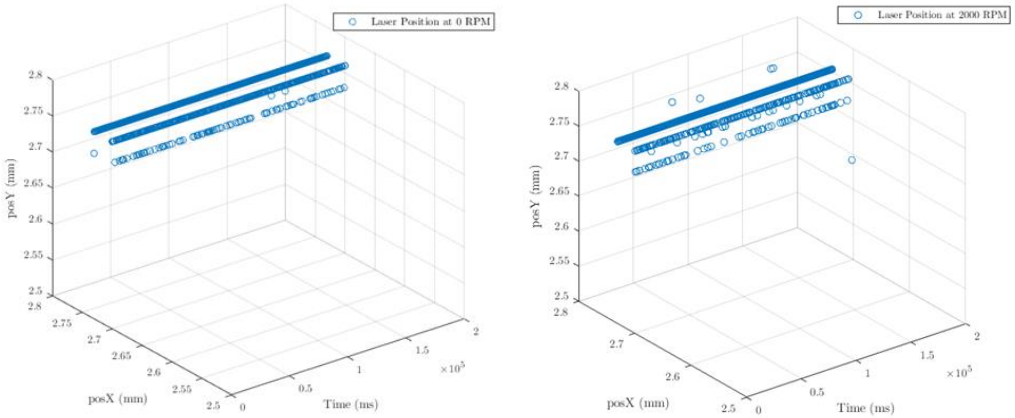

(a) (b)

Figure 5-15: Beam position at (a) 0rpm (b) 2000rpm

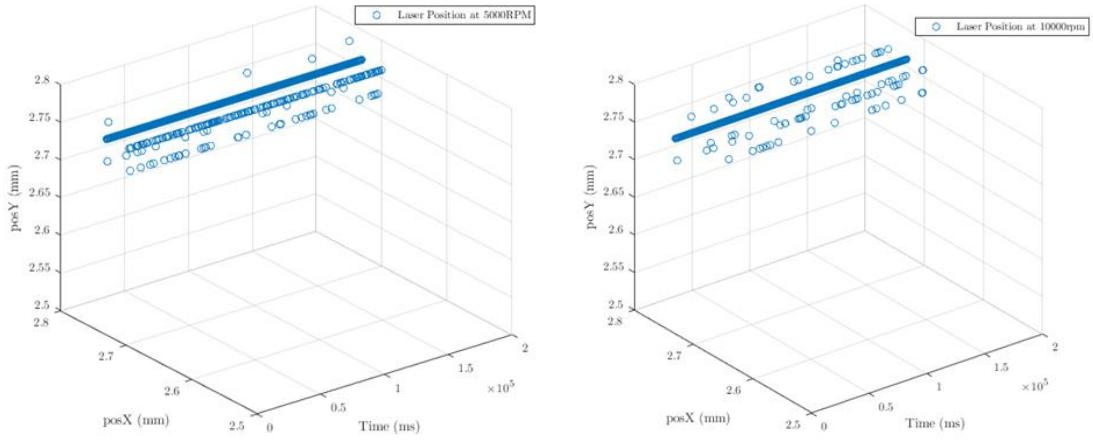

(b) (b)

Figure 5-16: Beam position at (a) 5000rpm (b) 10000rpm

5.4. Optical Receiver Sampling Rate Upgrade

The first experiment utilized the Arduino Mega 2560 internal ADC channels to sample the QD beam position sensor at 8MHz. The slow clock speed resulted to insufficient sampling rate required to fully characterize the high frequency beam position fluctuations. The subsequent system upgrade uses Arduino Due microcontroller with 84MHz clock speed, 12-bit ADC and AT91SAM3X8E 32-bit ARM Core MCU compared to ATMega2560 16MHz clock. A Quadrant detector connected to Due's four ADC channels was sampled at 71 KHz. A 64 channel PDA detector would be sampled at 4.4 KHz: this sufficiently meet the Nyquist criterion and the bandwidth of interest. It became crucial to employ an external dedicated ADC circuitry to interface between the PDA and the Arduino Due because of the limited ADC ports (12 analog ports) available on the board. The two leading contenders were the Texas Instruments DDC264 and the Analog Devices ADAS1127. DDC264 is capable of delivering up to 20-bit resolution, 64-channels conversion at 6000 samples per second and 3mW per channel. ADAS1127 can deliver up to 24-bit resolution, 64-channels conversion at 19,700 samples per second and 6.25mW per channel. DDC264 was selected because of its dual switched integrator architecture, converting current-to-voltage directly and eliminating the need for external buffer.

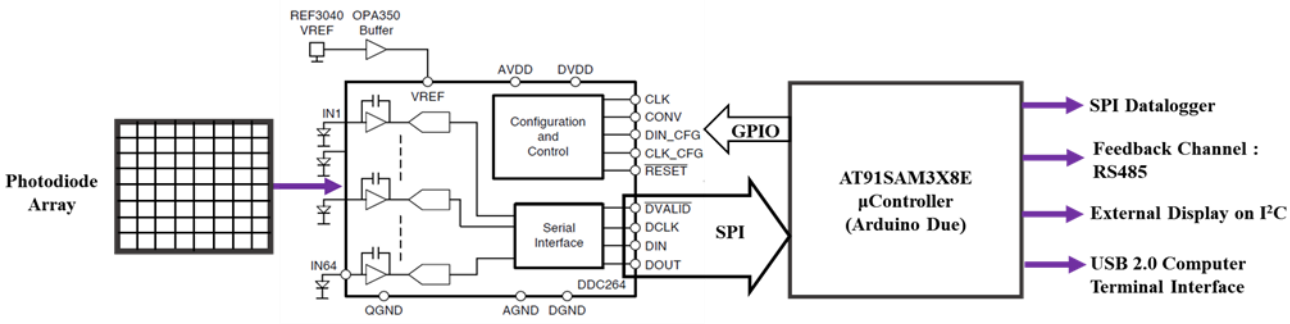

Figure 5-17: The Texas Instruments DDC264 analog Frontend

Figure 5-18: DDC264 Chip and DDC264EVM Module

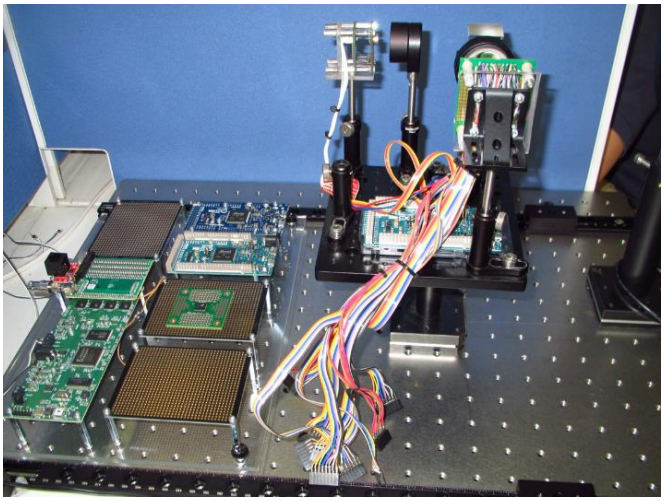

Figure 5-19: Optical bench assembly

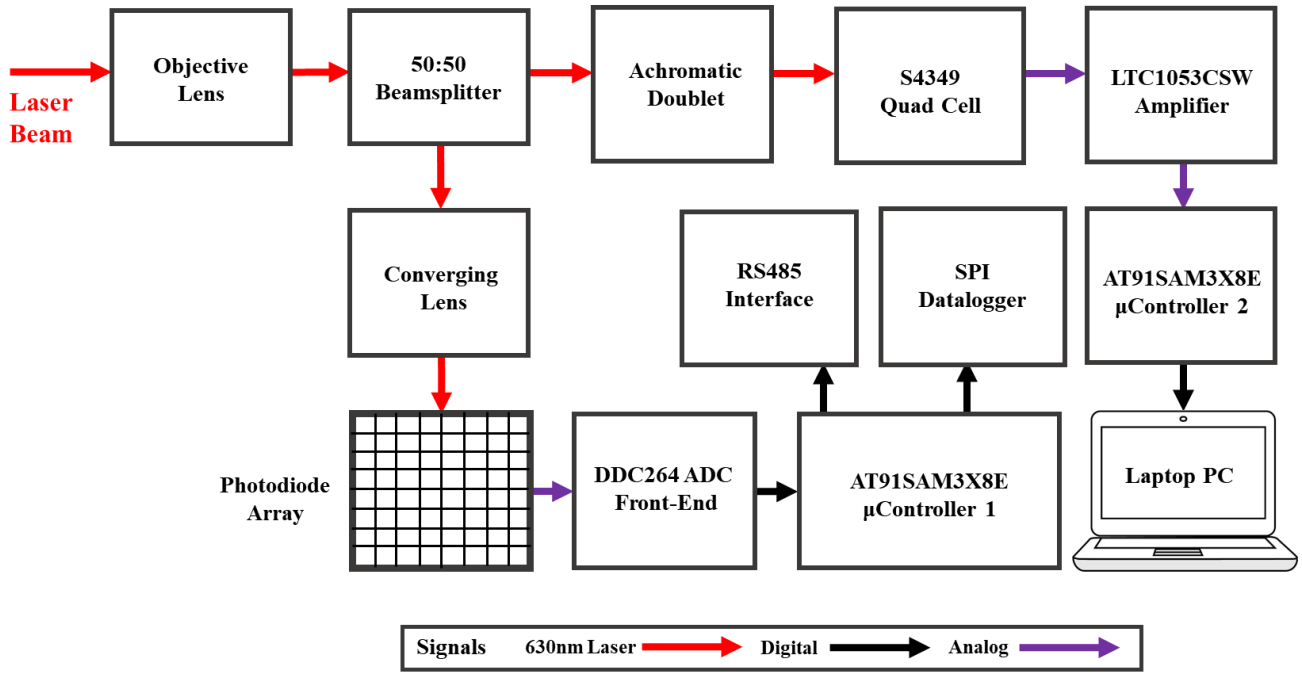

Figure 5-20: Block diagram of the upgraded PDA system.

5.5. A CubeSat Optical Module

A basic design of a CubeSat Optical Module is presented in this subsection. Designed around cheap and easily accessible COTS components. A fine steering mirror provides the required beam control while the form factor of the entire module conforms to the internal configuration of the target structure.

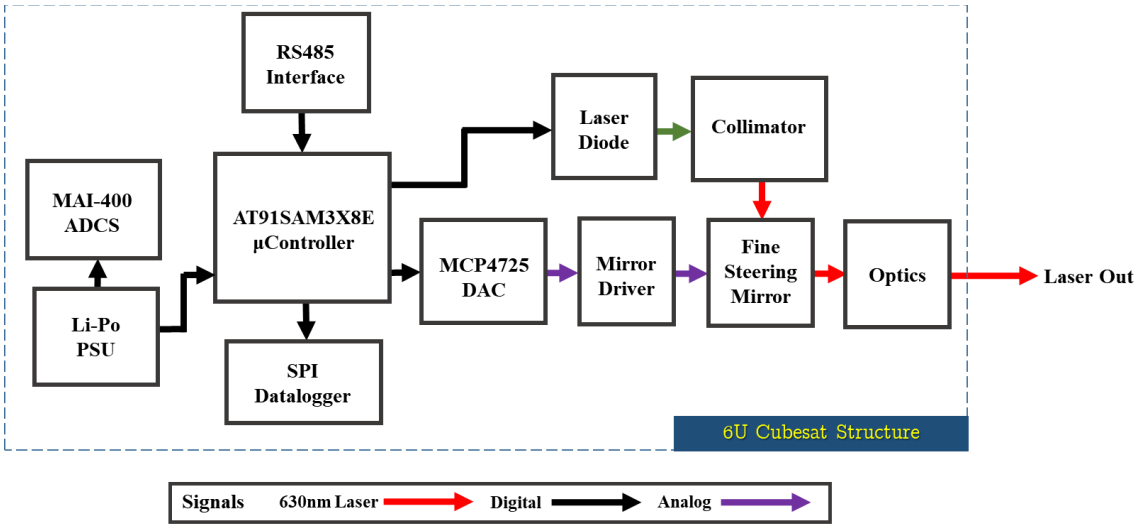

Figure 5-21: Block diagram of the CubeSat optical module

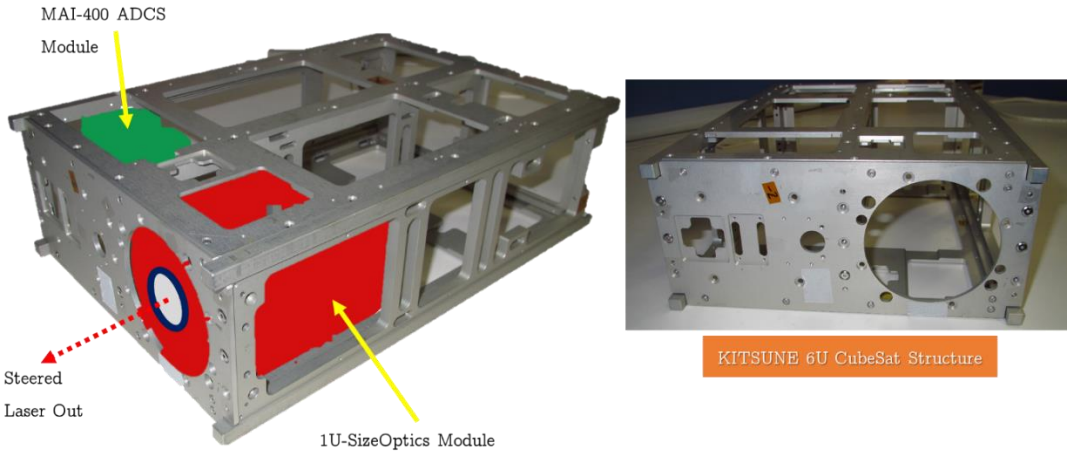

Figure 5-22: KITSUNE Satellite 6U Structure

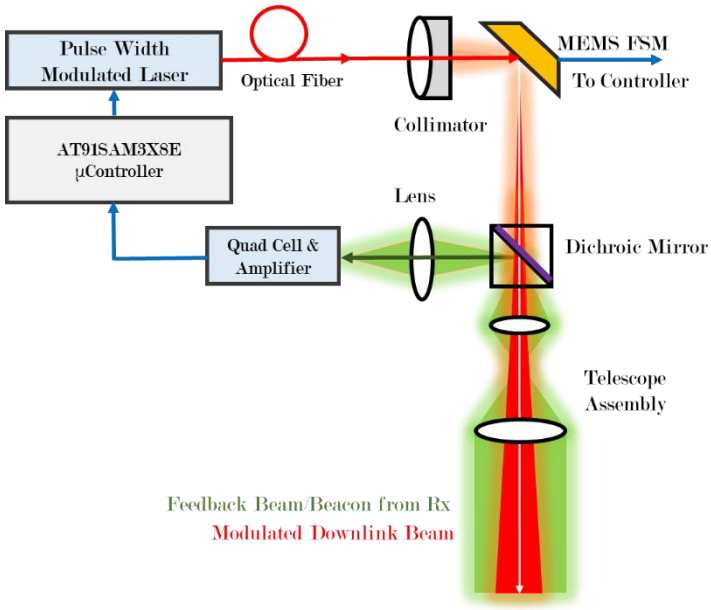

Figure 5-23: Conceptual layout of CubeSat Optical Communication Module Optics

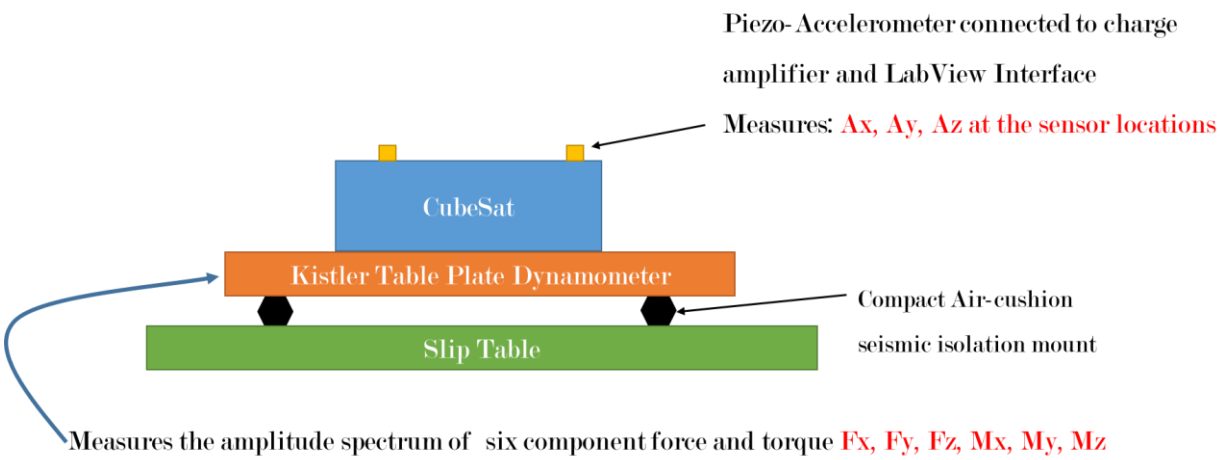

Figure 5-24: Typical Micro-Vibration or Jitter Measurement Setup

6. DRONE 40GBPS LASERCOM PROJECT

Figure 6-1: Hexacopter Drone with Fitted Lasercom Module

6.1. Introduction

Small satellites (CubeSats) and UAVs/Drones share similar limited-resources problem and can both be categorized as lean platforms. They are also the platforms of first consideration for laser transceiver integration in ubiquitous hybrid optical and RF metropolitan systems because of their wide range of utility. This Chapter describes the development of fine pointing system for the 40Gbps Drone laser communication project, an integral part of this research. The Space Communications Laboratory of the National Institute of Information and Communications Technology (NICT), Tokyo and the Laboratory of Lean Satellite Enterprises and In-Orbit Experiments (LaSEINE), Kyushu Institute of Technology commissioned collaborative research efforts on development of advanced laser communication systems for small satellites and air-borne platforms. Both NICT and LaSEINE possesses experience and previous technology demonstration heritage on lasercom and small satellites respectively. The Drone Lasercom system features an infra-red (1550nm) laser downlink with an optical ground receiving system (OGS). The OGS will be equipped with a wider divergence green (976nm) beacon laser and a motorized system for coarse-tracking of the Drone. Fine pointing of the downlink laser from the Drone will be implemented using microelectromechanical fine steering mirror in a closed-loop control with optical position sensing detectors on the Drone and the OGS. The Drone adopted for the experiment is the professional DJI Matrice 600 pro hexacopter capable of 3.5km horizontal flight range and payload mass of up to 5kg. It hosts a remote controllable DJI-Ronin-MX 3-Axis stabilized gimbal platform, which will be the platform for the onboard optical module, (Pseudo-Random Binary Sequence) PRBS data generator, Bit-Error-Rate Tester (BERT) and other electronic devices.

6.2. System Architecture

The system utilizes multi-stage control strategies in order to maintain a stable line-of-sight laser beam link between the Drone and optical ground system (OGS). Coarse pointing system using optical tracker on the ground and an onboard narrow FoV camera sending down live video feed. The handheld flight radio controller provides a simple way for the user to manually adjust the movement and orientation of the Drone and the gimbal hosting the lasercom module independently. Onboard GPS transmitter providing continuous and real-time streams of the Drone coordinates to the OGS also support the coarse tracking.

(a) (b)

Figure 6-2: (a) DJI Matrice 600 Pro, (b) Fitted Ronin MX Gimbal Stabilizer.

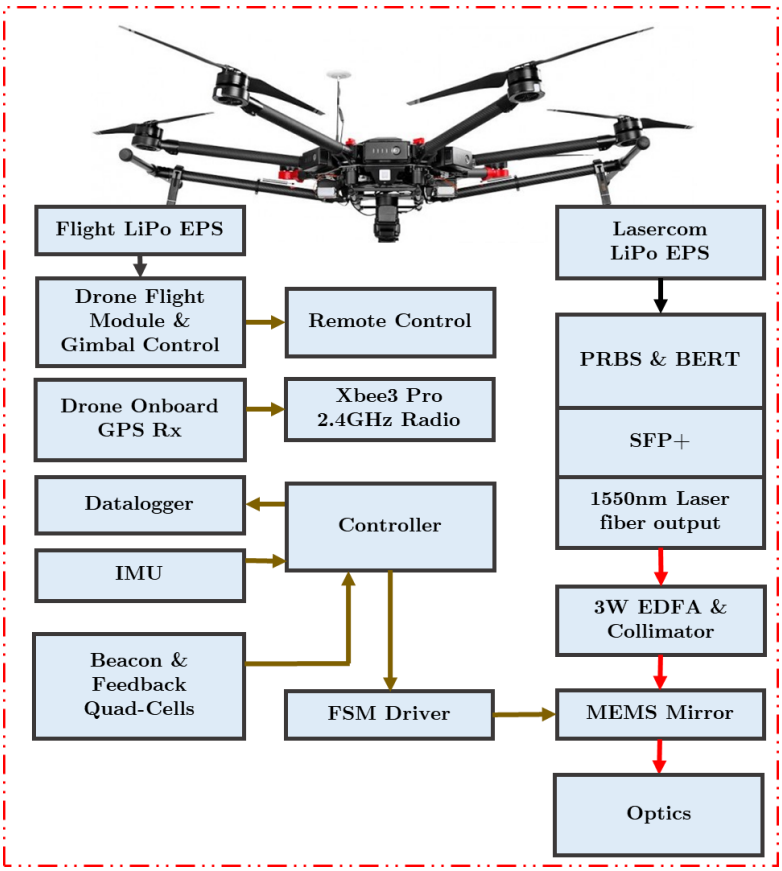

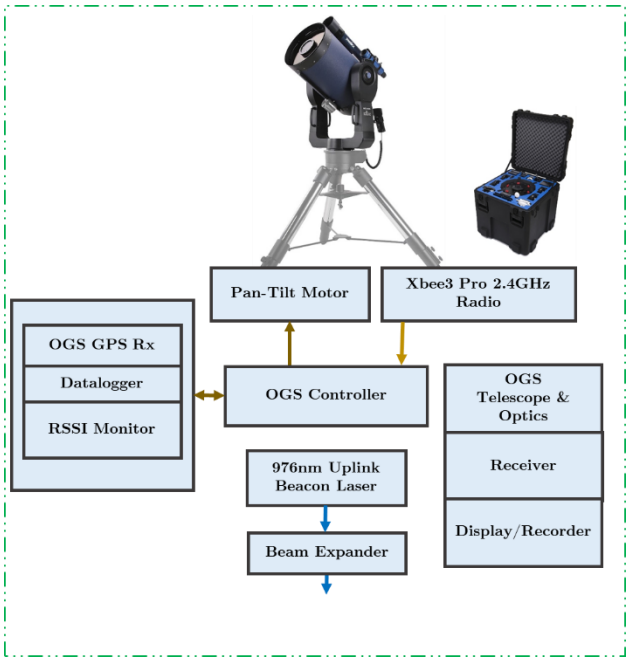

Figure 6-3: Onboard Lasercom and optical ground subsystems

6.3. Drone Onboard Optics Design

The Drone lasercom module was designed to be compact, minimal-weight and very low power consumption. A 3W EDFA amplifiers the PRBS fiber laser output and incident the FSM via the collimator assembly. A PSD senses the incoming beacon, while its angle of arrival is computed. A mapping of the PSD aperture and that of the FSM enables efficient control algorithm to point the downlink beam to the direction of the beacon. An internal closed-loop feedback control ensures fine control and stability of the FSM beam pointing as illustrated in the block diagram below:

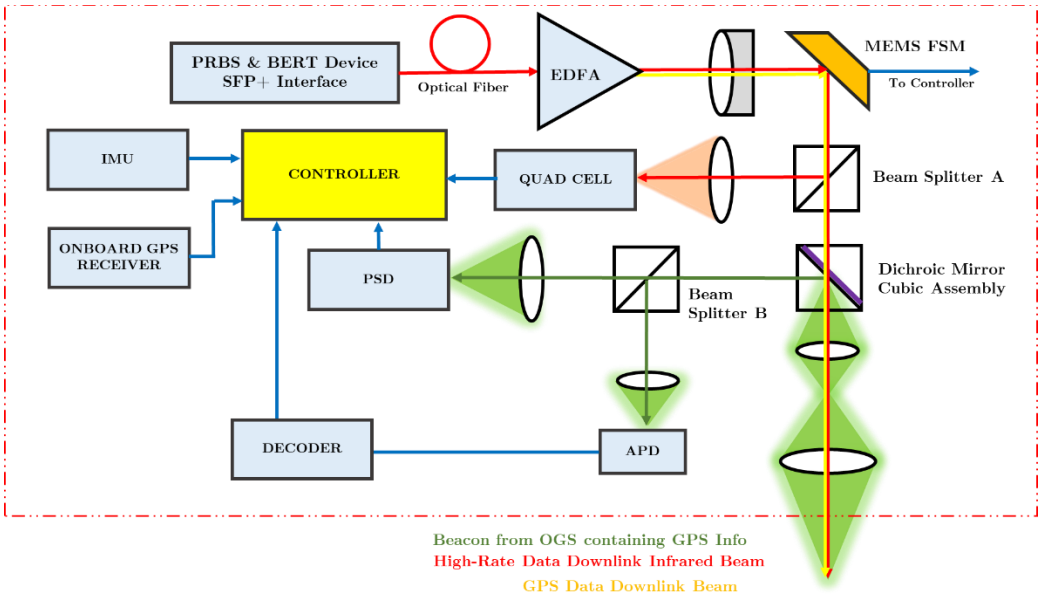

Figure 6-4: Optics system block diagram

6.4. Fine Pointing System

Fine beam pointing system (FPS) is achieved by a dedicated controller circuitry that drives a dual-axis MEMS Fine Steering Mirror. A beacon laser from the OGS is received by a PSD sensor on the Drone, while the angle-of-arrival of the beam is computed by the controller. The task of the controller is to maintain a highly stable downlink beam aligned with the OGS despite the vibrations or movement of the Drone in flight.

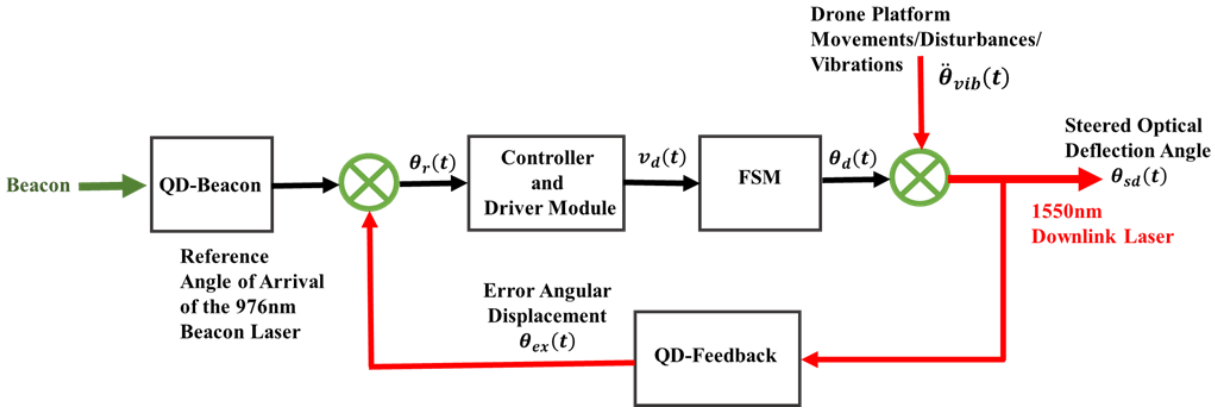

Figure 6-5: FSM Controller scheme

6.5. Onboard Electronics

6.5.1. Mirrorcle Fine Steering Mirrors

The two-dimensional, high dynamic response FSM from Mirrorcle Technologies was selected as the main beam actuator. Mirrorcle offered selectable fine steering mirror sizes, actuators and surface coatings as part of the semi-custom development kit. The table below summarizes the parameters of the mirrors as provided in the device datasheets

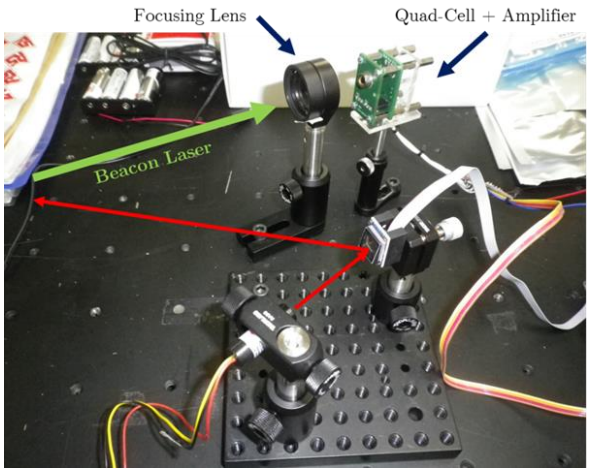

Figure 6-6: Mirrorcle FSM and Laser Diode Mounted on Breadboard

Table 6-1: Mirrorcle Semi-Custom Dev. Kits FSM

MEMS Mirror	*Size (mm)*	*Coating*	*Max. Angle (deg)*	*Max. VBias (V)*	*Size (mm)*	*Res.Freq. X, Y (Hz*	*LPF Cut-off freq*
S41369	2.4 Integrated	Al	7.7471	80	157.4	901, 905	300
S45842	5.0 Bonded	Au	6.3435	90	180	388, 386	140
S40206	7.5 Bonded	Au	1.2250	80	158	515, 518	240

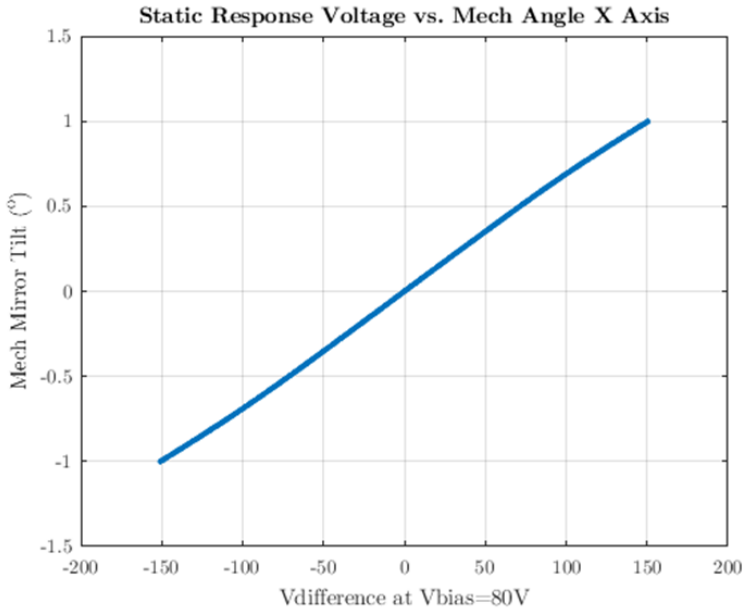

Figure 6-7: Mirrorcle FSM Static Response

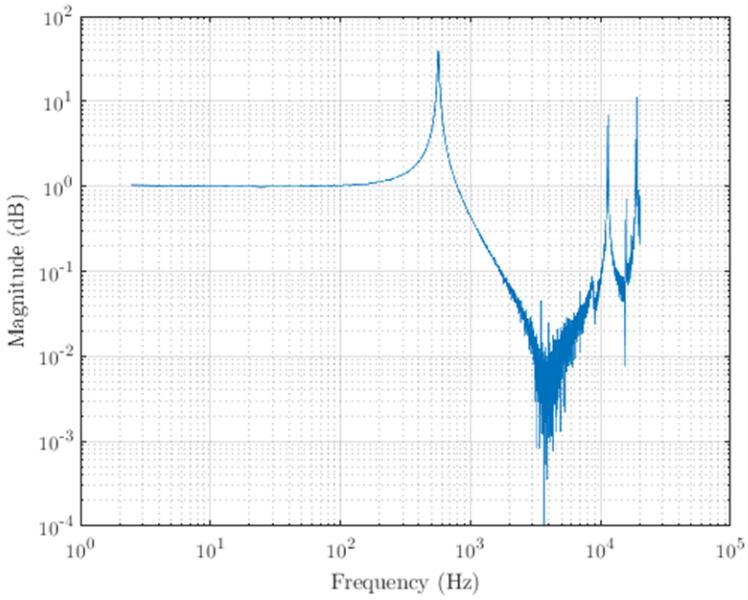

Figure 6-8: Mirrorcle FSM Magnitude-Frequency Response

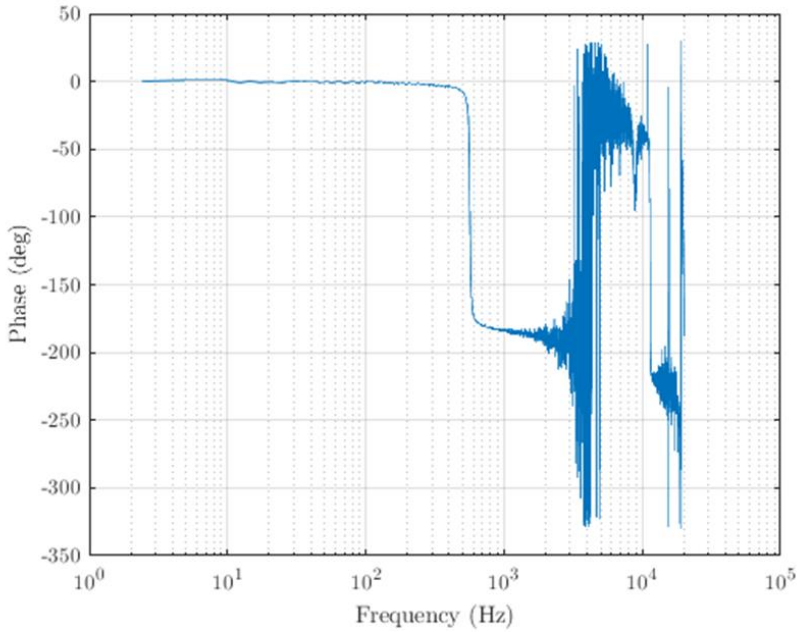

Figure 6-9: Mirrorcle FSM Phase-Frequency Response

6.5.2. Custom FSM Controller

The need to develop a custom controller for the fine steering mirrors stemmed from the non-adaptability of the Mirrorcle's USB Controller in the onboard optical system for the Drone. Flexibility, scalability, adding multiple sensors and implementing our beam steering algorithms requires the use of a microcontroller tasked with coordinating the processes. The Arduino board containing Atmel Mega2560 microcontroller was adopted with other peripherals for the initial prototype.

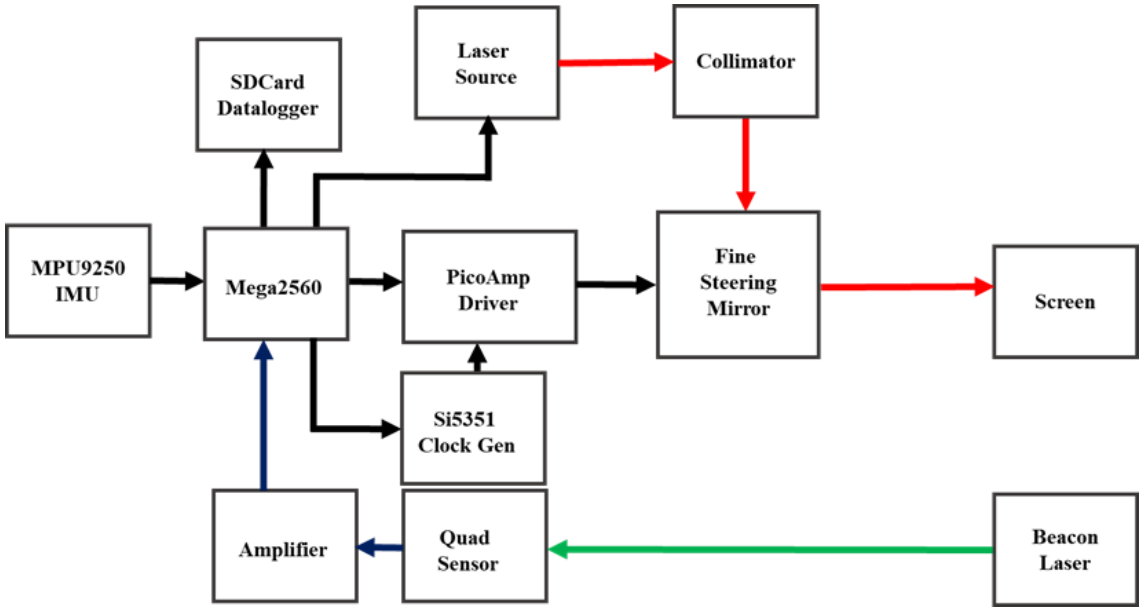

Figure 6-10: Block Diagram Showing the Custom Controller and the Beacon System

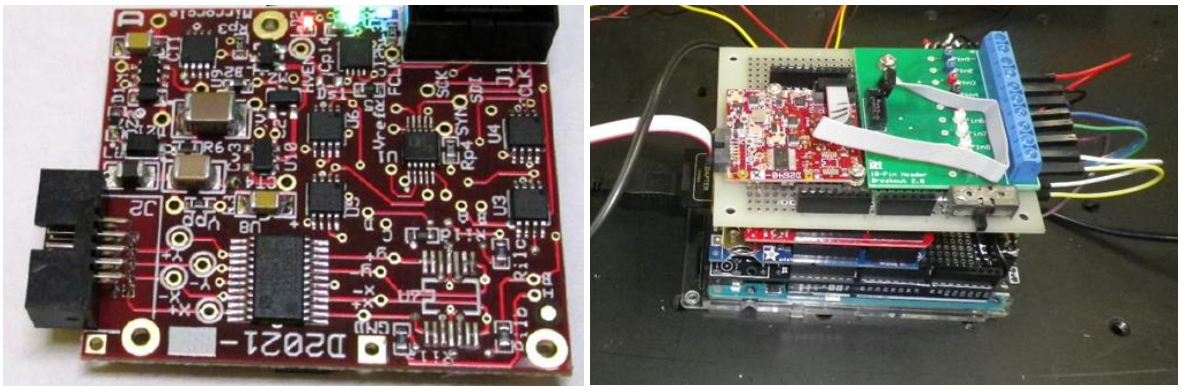

Figure 6-11: The PicoAmp board and Arduino-based custom FSM controller.

At the heart of the PicoAmp Driver board is the 16-bit AD5664R four-channel digital to analog converter and the MAX7413 Low-Pass Bessel Filter. The DAC receives SPI input data from the Mega2560 microcontroller and separate clock from an independent generator Si5351. PicoAmp supplies differential voltages ranging 0~160V. The output channels corresponds to the actuator inputs of the fine steering mirrors. The internal reference voltage was set at 1.25V. The FSM Bessel Filter requires a stable clock signal for its operation. The Si5351 breakout board by Adafruit was incorporated to provide software frequency selectable and clean square wave clock. The clock generator is controlled via I^2C datalines by Mega2560. For each FSM mirror, the filter cut-off frequency determines the frequency of the generators output. For example, recommended LPF cut-off frequency for the 7.5mm mirror is 240Hz, therefore the required clock frequency is FCLK=240 x 60 Hz = 14.4 KHz. Overall, the LPF determines the maximum bandwidth of the FSM (25 KHz upper limit for the Mirrorcle mirrors).

$$\mathrm{FCLK} = \frac{\mathrm{PLL}}{900 \times 32} \tag{6-1}$$

$$\mathrm{PLL} = 25\mathrm{MHz} \times \left(16 + \frac{368}{625}\right) \tag{6-2}$$

Before the beacon signal loop was connected, the Controller was programmed to display waveforms on the screen by deflecting the incident red laser light at predetermined patterns. The FSM actuator has four-channels; A, B, C and D with biasing voltage functions $V_A(t)$, $V_B(t)$, $V_C(t)$, $V_D(t)$ needed to move the mirror between +X to -X and −Y to +Y angular displacements.

$$\mathrm{X\_V_{diffence}}(t) = V_A(t) - V_B(t) \tag{6-3}$$

$$\mathrm{Y\_V_{diffence}}(t) = V_C(t) - V_D(t) \tag{6-4}$$

The amplitude of $\mathrm{X\_V_{diffence}}$ and $\mathrm{Y\_V_{diffence}}$ must not exceed 200V otherwise the FSM device will be damaged. The V_{bias} is device dependent (stipulated in the datasheet, see Table 6-1 above) and it set the FSM X and Y axes to origin position. By mixing different types of

wave functions in the four channels, it is possible to display any kind of shape or waveform on the screen using the fine steering mirror.

$$V_A(t) = V_{bias} + A\sin\left(2\pi ft + \frac{\theta_A}{360}\right) \quad (6\text{-}5)$$

$$V_B(t) = V_{bias} + A\sin\left(2\pi ft + \frac{\theta_B}{360}\right) \quad (6\text{-}6)$$

$$V_C(t) = V_{bias} + A\sin\left(2\pi ft + \frac{\theta_C}{360}\right) \quad (6\text{-}7)$$

$$V_D(t) = V_{bias} + A\sin\left(2\pi ft + \frac{\theta_D}{360}\right) \quad (6\text{-}8)$$

$$V_{bias} = \frac{V_{fsm}}{200} \times (2^n - 1) \quad (6\text{-}9)$$

V_{fsm} =16 bits for 7.5mm mirror, and n=16. For example, a circle with radius A, is displayed on the screen if the phase angles:

$$\theta_A, \theta_B, \theta_C, \theta_D = 0^o, 180^o, 90^o, 270^o \quad (6\text{-}10)$$

Spirograph and other shapes were displaced by varying the phase values. More complex functions can also be applied to display desired outputs.

6.5.3. GPS Receiver

The GPS board was configured in the UBlox U-Center desktop software to parse NMEA sentences at 115200 baud rate via the I2C port. The data is sent to the XBee radio on UART port of the microcontroller for transmission to the ground-based receiver and datalogger.

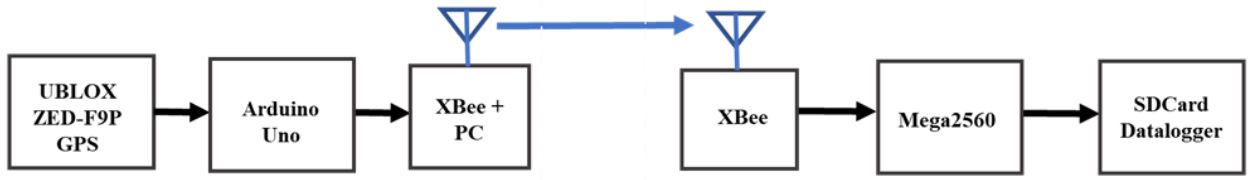

Figure 6-12: Block Diagram of GPS Data Transmission

6.5.4. The EDFA Unit

The Amonics Erbium Doped Fiber Amplifier (EDFA) was adopted as a critical component of the lasercom module. It provided the needed laser EIRP level to meet the design link margin with the receiving telescope. Operating at 1540-1565nm, it provides up to 3W laser power.

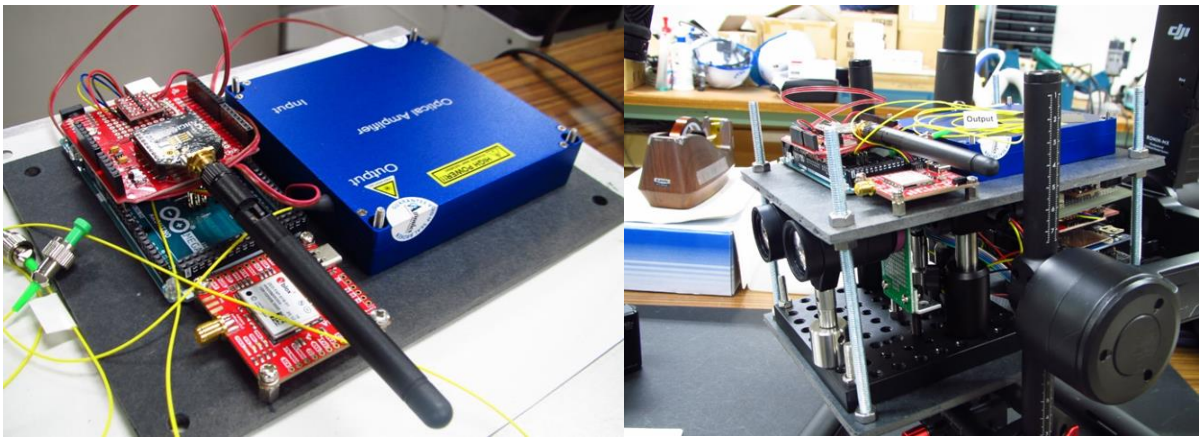

Figure 6-13: EDFA mounted close to the GPS module

6.6. Drone Jitter Measurement

In order to characterize the vibrations induced by the Drone propeller and how it could affect the operation of the fine pointing system, a jitter experiment was conducted where the lasercom module coupled with the Drone was firmly fixed to the ground. The Drone and a receiving system separated about 15meters and at direct line-of-light. The gimbal was stabilized while the propellers where operated at full speed. Accelerometer and Gyroscope in the lasercom module recorded the vibrations of the platform while a laser position sensor at the receiver monitored the displacement of the beam footprint at the receiving end.

6.6.1. Hardware Setup

Figure 6-14: Transmitting Drone and optical receiver.

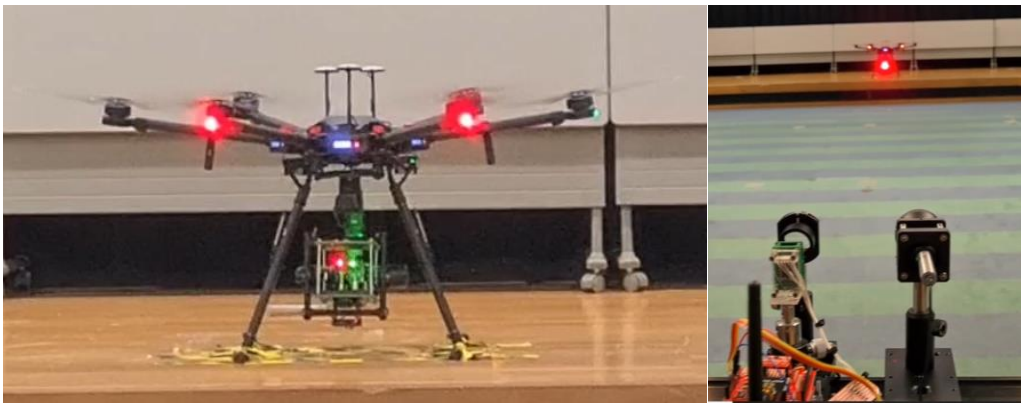

Figure 6-15: Laser beam from the Drone lasercom module illuminating the receiver.

Figure 6-16: Beam footprint at the receiver.

6.6.2. Experiment Results

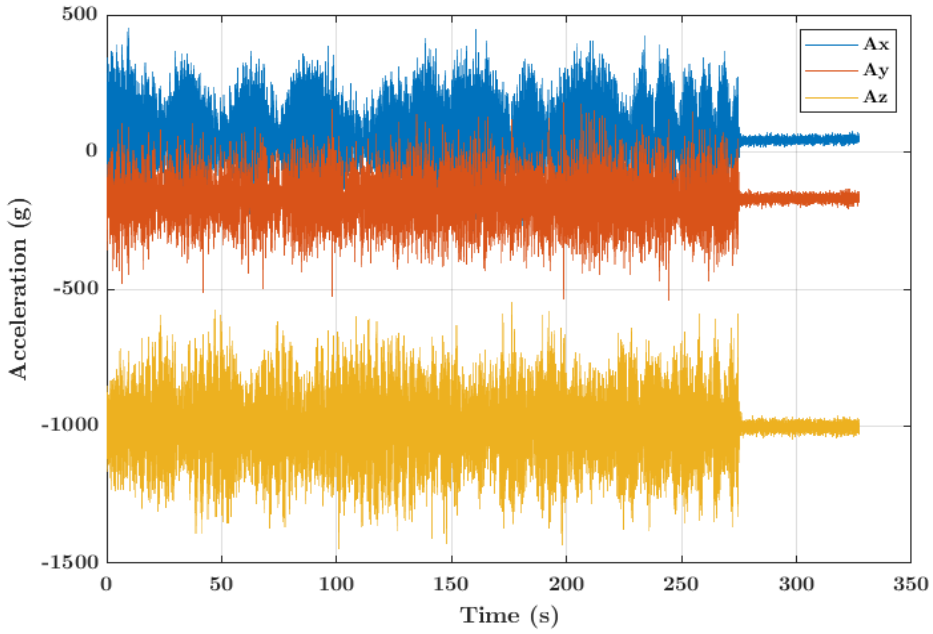

Figure 6-17: Readings from MEMS accelerometer inside the lasercom module

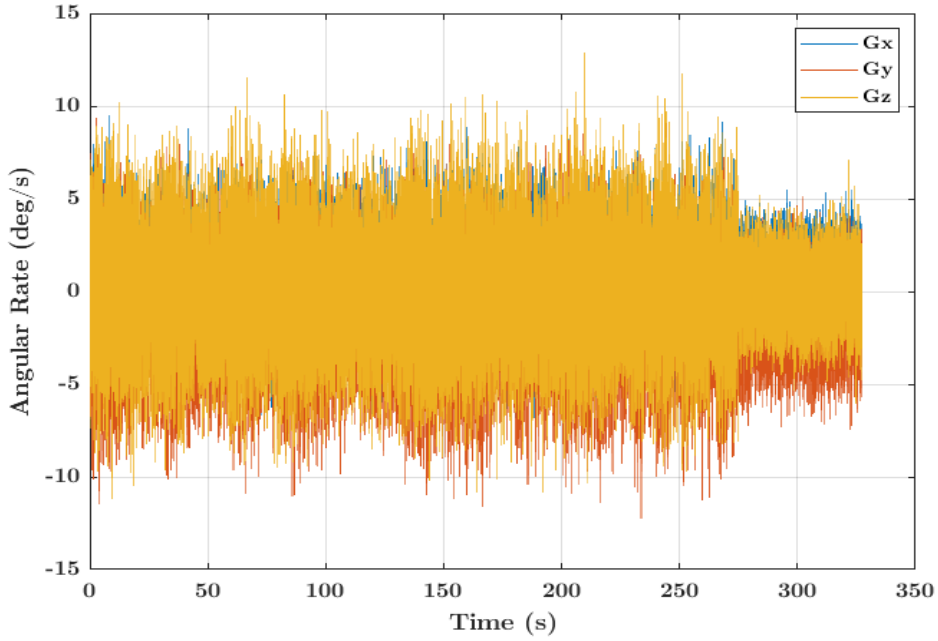

Figure 6-18: Readings from MEMS gyroscope inside the lasercom module.

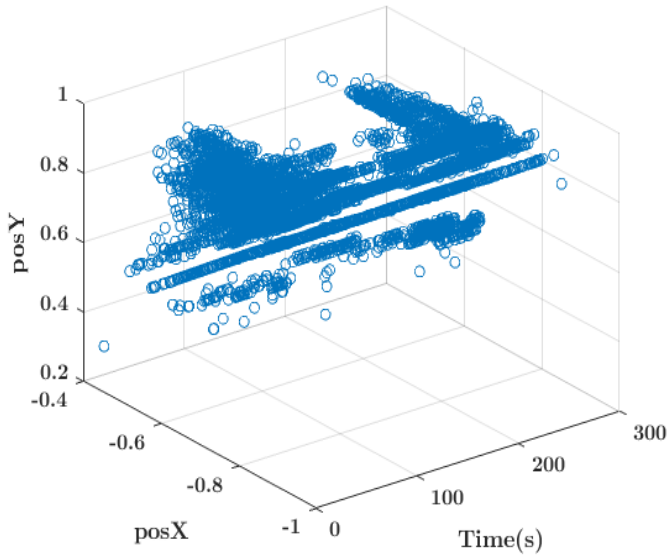

Figure 6-19: Laser beam centroid at the receiver showing the pointing instability of the beam due to the jitter produced by the Drone's propeller

7. CONCLUSION AND RECOMMENDATIONS

7.1. Conclusions

The research reported in this thesis presented the study, design, and experiments on technology development of free-space optical communications for resource-limited small satellites as detailed in the research purpose and objectives section. A feasibility study and systematic analysis of a design reference mission, conceptualizing a direct free-space optical communication link between a Moon orbiting 6U CubeSat and a compact optical ground station on Earth, downlinking mission data at 250megabits per seconds. Data return at this design rate exceed the state-of-art for small satellites and represents much greater performance than a comparable radio frequency communication system. Allocation of the satellite on-board resources, most especially power consumption by the optical module, payload and other subsystems shows that it is practicable to integrate optical communication transceivers on microsatellites. Required COTS components including ADCS and MEMS FSM associated units with desirable performance have been identified. An optical ground segment featuring a readily available and low-cost telescope adaptable to the system architecture was presented. Use of adaptive optics (deformable mirrors) helps mitigate effects of wavefront aberration and scintillation induced by atmospheric turbulence. A link availability and outage probability due to the weather conditions was estimated. The Moon is quiet accessible from the Earth, it was deduced from the analysis that the link would be maintained for averagely 50% of time each day of the year. Peak atmospheric attenuations were noticed during heavy fog events with low atmospheric visibility.

This thesis also introduced the use of a scalable Photodiode Array device as an optical feedback sensor for fine beam pointing and control. It was demonstrated by experiment using COTS components that the PDA with a much lower resolution compared to CCD cameras but having faster response can sufficiently assist a close-loop fine beam position control. MEMS Fine Steering Mirrors are critical actuators in lasercom fine beam pointing and platform disturbance suppression systems due to miniature-size, easy to drive, agile and less demand of platform resources. They are often combined with optical sensors such as quad cells (QD), position sensitive devices (PSD) and CCD cameras in close-loop automatic control of the beam position. CCD cameras generally have slow detection and processing speeds while the field-of-regard is very limited in QDs and PSDs due to their smaller aperture size. In QDs, the laser beam spot size after focusing usually are comparable to the quadrant pixel size hence restricting the beam deviation on the surface to limited amounts. The spatial size of the PDA sensor can be increased if desired depending on the specific application requirements. Much higher detection frame rates are also achievable with increased computing capacity by using faster microprocessors. The PDA sensor is attractive for use on resource-limited platforms such as small satellites, CubeSats, unmanned aerial vehicles and high altitude vehicles where size, weight, and power supply are tightly managed and distributed.

Platform micro-vibrations generated by mechanically active subsystems in a satellite are capable of perturbing the stability of the laser beam line-of-sight alignment between the satellite and an optical ground segment. This research experimentally determined the spectrum of jitter produced by a typical reaction wheel designed for CubeSats. Determination of frequency regions with the maximum power spectral density is a crucial knowledge that is very useful in the design of an active fine steering mirror based jitter mitigation system.

As an integral part of the research, a fine pointing system for 40Gbps Drone laser communication project was designed and developed. Drones share similar platform characteristics with small satellites and hence allowing a cross-platform compatibility of optical communication module. The central actuator of the fine pointing system is the dual-axis Mirrorcle MEMS Fine Steering Mirror which was successfully evaluated and integrated. An Arduino microcontroller-based Custom FSM controller was designed, programmed and tested. The Controller was independently used to display different waveforms and then adapted in the lasercom control system implementing an open-loop Beacon angular movement follower. GPS transmitter, receiver and datalogger were assembled as part of the onboard lasercom module. The full optics and control system was assembled into the lasercom module. Jitter experiment to evaluate and characterize the spectrum of vibrations produced by the Drone's propeller and how it affects the stability of the beam pointing was conducted.

7.2. Future Work

It was shown in the DRM weather induced outage analysis that attenuation due to rain and visibility followed similar pattern throughout the year considered. Heavy rainfall events would have strong impacts on the link but fog and cloud cover remains the biggest contributor. Snow and cloud cover statistics were not covered in the analysis, this should be the subject of future work.

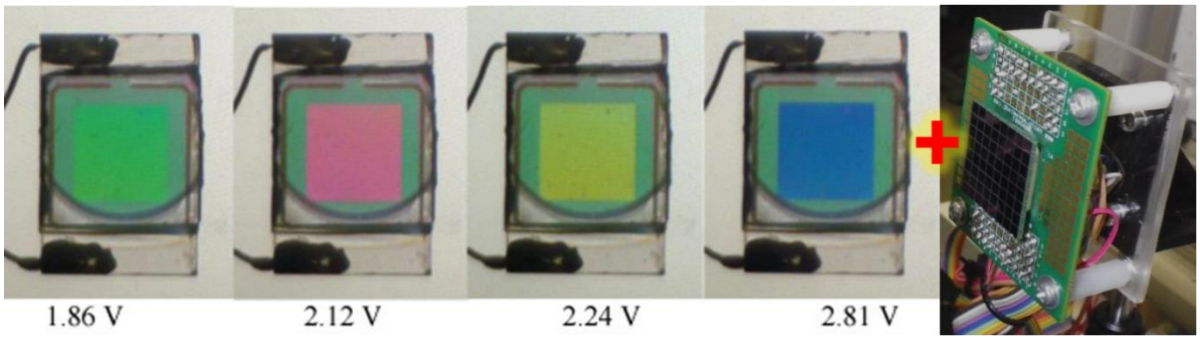

Figure 7-1: Combination of Beamco liquid crystal tunable filter with the PDA

Combination of the PDA with electrically tunable spectral filters makes the PDA a very unique sensor capable of detecting multiple wavelength lasers position in a single package. This comes with enormous advantages in applications such as DWDM and bi-directional optical communication modules that utilizes many laser beams for uplink and downlink, drastically reducing the number of optics, weight and power consumption. Future work should address minimizing effects of the narrow elemental gaps and dead zones on the precision of dynamic

laser beam centroid computation. More efficient centroiding algorithms such as the best-fit to Gaussian approach will enhance the detection accuracy of the photodiode array sensor and consequently the performance of the fine steering control system.

AUTHOR BIOGRAPHY

Born in Lagos on the 3rd of July, 1985. Femi M. Ishola attended Igbobi College Yaba, Lagos, Nigeria from 1995 to 2000, where he received rudimentary science education and inspirations on space explorations. At the high school, he showed deep interests and excelled in mathematics, electronics and science subjects. After graduation he proceeded to Ondo State Polytechnic where he became exposed to detailed studies in Electrical and Electronics Engineering. He was the best graduating student in the Department, finishing well with a distinction grade. In 2005, He worked at Life Transmissions as part of the Polytechnic industrial work experience scheme. At Life transmissions, he was tasked with uplink antenna system setup for the satellite digital video broadcasting service utilizing Eutelsat W3A. He also supported the webcasting team and acquired hands-on experience in computer hardware assembly, software programming and networking operations.

In 2006 he was admitted to the University of Lagos through direct entry to 200 level to pursue a Bachelor of Science Degree in Electrical Electronics Engineering. At the University, through intensive lectures, laboratory experiments and hands-on practical projects, he honed his analytical, engineering and scientific problem-solving skills. In 2009, he was dispatched to the 401 Aircraft Maintenance Depot of the Nigerian Air Force Logistics Command situated at the Lagos International Airport. There, he acquired profound experience in aircraft communication systems, landing support systems, radar and warning systems, guidance, navigation and control systems of the Lockheed Martin's C130-Hercules and Alenia's G222 transport aircrafts. The same year, he established his start-up enterprise Phemotron Systems, which later became an operational limited liability company. His final year thesis project was centered on microwave wireless power transmission prototype, a technology gap area crucial for the realization of the space-based solar power station concept. This earned him the first position, the best and most innovative project awards at the national universities students' project competition in 2010. He graduated from the University of Lagos in 2010, completed the compulsory national service (NYSC) in Kano, 2011, finishing with the State Government Award and Presidential honor nomination for the best Millennium Development Goals (MDGs) projects. While in Kano, he executed a long list of innovative and community development projects including installation of the orientation broadcasting service studio, solar powered street lights, automatic waste bins among others, funded through invited private companies and his personal finance He was also very active in STEM and space awareness programs among youths, serving as the Director of Student Affairs of the Space and Satellite Professionals International (SSPI) under the leadership of the Nigeria chapter President.

Between 2011 and 2013, he focused on nurturing his startup company, Phemotron Systems Ltd, serving as the CEO. Research and developments of the Aircraft Wireless Intercom System (AWIS) project. He also successfully complicated web programming and development contracts for a good number of high profile corporate clientele. Through consulting for StreetFinders Ltd, he designed and fabricated unique interactive outdoor media platforms as well as internet portal solutions targeting the Lagos Central Business District.

His interests and fascination about space exploration stimulated him to enroll for Master's degree program in Space Studies at the International Space University (ISU), located at Illkirch-Grafenstaden, Strasbourg, France in 2013. At ISU, Femi acquired an all-round perspective about space and later focused on satellite communication major. He benefited from the generous Heinlein Price Trust. He completed individual project on Satellite-based backpack telemedicine system and contributed to the One Way Mission to Mars team project. During the time, he had study visits several to space corporations and facilities in France, Germany, Luxembourg and Moscow, acquiring important knowledge and experiences. At the final phase of the ISU course in 2014, he participated in the Southern Australian Universities QB50 Collaboration Satellite project at the Institute for Telecommunications Research, University of South Australia (UniSA), Mawson Lakes, in Adelaide as an international visiting research student. He successfully designed and produced an antenna module prototype for CubeSat project. He was later a Teaching Associate at the Southern Hemisphere Space Studies Program.

In 2015, he joined the Centre for Space Transport and Propulsion, an activity center of the National Space Research and Development Agency (NASRDA), Federal Ministry of Science and Technology. At the Space Agency, he was tasked with developing communication, guidance, navigation and control systems for the Sounding Rocket and Unmanned Aerial Vehicle (UAV) projects. He pioneered and became the Project Manager of the CSTP Ground Control Station proposing, designing and leading a team of engineers to assemble the facility from ground-up.

Attracted by the space technology capabilities in Japan, he decided to progress to doctoral level research in 2018. He was accepted to pursue a PhD degree at the Kyushu Institute of Technology's (Kyutech) Laboratory of Lean Satellites and In-Orbit Experiments (LaSEINE) under Professor Mengu Cho. Within a couple of months into his research, he was selected for the Emerging Space Leaders grant award by the International Astronautical Federation in 2019 and presenting his research on laser communications at the 70th International Astronautical Congress, Washington D.C. USA. During his PhD studies, he travelled to Russia, participating in a short nanosatellite design course at the Samara National Research University, Samara Oblast. He played a critical role in the development of fine pointing system for the 40Gbps Drone Laser communication project, a collaboration between the National Institute of Information and Communications Technology (NICT), Tokyo and Kyutech. Empowered with top-notch international education, business, technical and research experiences, Femi's ultimate goal is to revolutionize the global commercial deep space exploration industry, simultaneously facilitating benefit returns and giving accessibility to non-space fairing and under-develop countries of the world.

REFERENCES

[1] History. com Editors, "Morse Code & the Telegraph," *HISTORY*, Nov. 09, 2009. https://www.history.com/topics/inventions/telegraph (accessed Sep. 21, 2021).

[2] G. Falciasecca and B. Valotti, "Guglielmo Marconi: The pioneer of wireless communications," in *2009 European Microwave Conference (EuMC)*, Sep. 2009, pp. 544–546. doi: 10.23919/EUMC.2009.5296358.

[3] G. Marconi, "Wireless telegraphic communication," *Reson*, vol. 7, no. 1, pp. 95–101, Jan. 2002, doi: 10.1007/BF02836176.

[4] R. W. Simons, "Guglielmo Marconi and Early Systems of Wireless Communication," *GEC REVIEW*, vol. 11, no. 1, p. 19, 1996.

[5] Y. Karasawa, "On physical limit of wireless digital transmission from radio wave propagation perspective: Physical Limit of Wireless Transmission," *Radio Sci.*, vol. 51, no. 9, pp. 1600–1612, Sep. 2016, doi: 10.1002/2016RS006040.

[6] C. E. Shannon, "A Mathematical Theory of Communication," *Bell System Technical Journal*, vol. 27, no. 3, pp. 379–423, Jul. 1948, doi: 10.1002/j.1538-7305.1948.tb01338.x.

[7] F. Ishola and M. Cho, "Experimental Study on Photodiode Array Sensor Aided MEMS Fine Steering Mirror Control for Laser Communication Platforms," *IEEE Access*, vol. 9, pp. 100197–100207, 2021, doi: 10.1109/ACCESS.2021.3096816.

[8] "SpaceX adds laser crosslinks to polar Starlink satellites - SpaceNews." https://spacenews.com/spacex-adds-laser-crosslinks-to-polar-starlink-satellites/ (accessed Sep. 11, 2021).

[9] Laboratory of Lean Satellite Entreprises and In-Orbit Experiments, "Kyutech Small Satellite Database." Unpublished, 2020.

[10] R. E. Hodges, N. Chahat, D. J. Hoppe, and J. D. Vacchione, "A Deployable High-Gain Antenna Bound for Mars: Developing a new folded-panel reflectarray for the first CubeSat mission to Mars.," *IEEE Antennas Propag. Mag.*, vol. 59, no. 2, pp. 39–49, Apr. 2017, doi: 10.1109/MAP.2017.2655561.

[11] O. Kegege, Y. F. Wong, and S. Altunc, "Advances in Ka-band Communication System for CubeSats and SmallSats," p. 5.

[12] Committee on Achieving Science Goals with CubeSats, Space Studies Board, Division on Engineering and Physical Sciences, and National Academies of Sciences, Engineering, and Medicine, *Achieving Science with CubeSats: Thinking Inside the Box*. Washington, D.C.: National Academies Press, 2016, p. 23503. doi: 10.17226/23503.

[13] N. Chahat, J. Sauder, M. Thomson, R. Hodges, and Y. Rahmat-Samii, "CubeSat deployable Ka-band reflector antenna for Deep Space missions," in *2015 IEEE International Symposium on Antennas and Propagation USNC/URSI National Radio Science Meeting*, Jul. 2015, pp. 2185–2186. doi: 10.1109/APS.2015.7305481.

[14] K. Nakamaru, K. Kondo, T. Katagi, H. Kitahara, and M. Tanaka, "An overview of Japan's Engineering Test Satellite VI (ETS-VI) project," in *IEEE International Conference on Communications, World Prosperity Through Communications*, Boston, MA, USA, 1989, pp. 1582–1586. doi: 10.1109/ICC.1989.49944.

[15] M. Toyoshima *et al.*, "Reduction of ETS-VI Laser Communication Equipment Optical-Downlink Telemetry Collected During GOLD," p. 9.

[16] K. E. Wilson, "An Overview of the GOLD Experiment Between the ETS-VI Satellite and the Table Mountain Facility," p. 12.

[17] T. Morio *et al.*, "Overview of the Laser Communication System for the NICT Optical Ground Station and Laser Communication Experiments on Ground-to- Satellite Links," *NICT Journal*, p. 23.

[18] M. Naoe, “Overview of the Small Optical TrAnsponder_SOTA_Project, National Institute of Information and Communications Technology,” *ITEJ*, vol. 63, no. 6, pp. 780–783, 2009, doi: 10.3169/itej.63.780.
[19] K. Yoshisada, T. Morio, T. Yoshihisa, and T. Hideki, “The Uplink Data Received by OICETS,” p. 7.
[20] K. E. Wilson, “Preparations for Planned OCTL to OICETS Optical Link Experiment (OTOOLE),” p. 12.
[21] T. JONO *et al.*, “In-orbit Experiment Result of Inter-satellite Laser Communication by OICETS.” Japanese Rocket Society, 2007. Accessed: Nov. 01, 2021. [Online]. Available: https://doi.org/10.11230/jsts.23.2_21
[22] T. Tanaka, Y. Kawamura, and T. Tanaka, “Development and operations of nano-satellite FITSAT-1 (NIWAKA),” *Acta Astronautica*, vol. 107, pp. 112–129, Feb. 2015, doi: 10.1016/j.actaastro.2014.10.023.
[23] H. Takenaka, A. Carrasco-Casado, M. Fujiwara, M. Kitamura, M. Sasaki, and M. Toyoshima, “Satellite-to-ground quantum-limited communication using a 50-kg-class microsatellite,” *Nature Photon*, vol. 11, no. 8, pp. 502–508, Aug. 2017, doi: 10.1038/nphoton.2017.107.
[24] A. Carrasco-Casado *et al.*, “LEO-to-ground optical communications using SOTA (Small Optical TrAnsponder) – Payload verification results and experiments on space quantum communications,” *Acta Astronautica*, vol. 139, pp. 377–384, Oct. 2017, doi: 10.1016/j.actaastro.2017.07.030.
[25] A. Carrasco-Casado *et al.*, “LEO-to-ground polarization measurements aiming for space QKD using Small Optical TrAnsponder (SOTA),” *Opt. Express, OE*, vol. 24, no. 11, pp. 12254–12266, May 2016, doi: 10.1364/OE.24.012254.
[26] M. Toyoshima, T. Sasaki, H. Takenaka, and Y. Takayama, “Scintillation model of laser beam propagation in satellite-to-ground bidirectional atmospheric channels,” *Acta Astronautica*, vol. 80, pp. 58–64, Nov. 2012, doi: 10.1016/j.actaastro.2012.05.009.
[27] H. Kunimori *et al.*, “Preliminary Results of Very Small Optical Transmitter (VSOTA) on Microsatellite RISESAT,” p. 5.
[28] H. Takenaka, A. Carrasco-Casado, M. Fujiwara, M. Kitamura, M. Sasaki, and M. Toyoshima, “Satellite-to-ground quantum-limited communication using a 50-kg-class microsatellite,” *Nature Photon*, vol. 11, no. 8, pp. 502–508, Aug. 2017, doi: 10.1038/nphoton.2017.107.
[29] D. R. Kolev and M. Toyoshima, “Satellite-to-ground optical communications using small optical transponder (SOTA) – received-power fluctuations,” *Opt. Express, OE*, vol. 25, no. 23, pp. 28319–28329, Nov. 2017, doi: 10.1364/OE.25.028319.
[30] “JAXA | Small Optical Link for International Space Station (SOLISS) Succeeds in Bidirectional Laser Communication Between Space and Ground Station,” *JAXA | Japan Aerospace Exploration Agency*. https://global.jaxa.jp/press/2020/04/20200423-1_e.html (accessed Nov. 01, 2021).
[31] K. Iwamoto *et al.*, “Experimental results on in-orbit technology demonstration of SOLISS,” in *Free-Space Laser Communications XXXIII*, Mar. 2021, vol. 11678, pp. 51–57. doi: 10.1117/12.2578089.
[32] H. Komatsu *et al.*, “In-orbit experimental architecture design of bi-directional communication with a small optical communication terminal attached on ISS and an optical ground station,” in *Free-Space Laser Communications XXXII*, San Francisco, United States, Mar. 2020, p. 11. doi: 10.1117/12.2551257.

[33] T. Kubo-oka *et al.*, "Development of 'HICALI': high speed optical feeder link system between GEO and ground," in *International Conference on Space Optics — ICSO 2018*, Jul. 2019, vol. 11180, pp. 2158–2165. doi: 10.1117/12.2536135.
[34] A. Carrasco-Casado *et al.*, "Intersatellite-Link Demonstration Mission between CubeSOTA (LEO CubeSat) and ETS9-HICALI (GEO Satellite)," in *2019 IEEE International Conference on Space Optical Systems and Applications (ICSOS)*, Portland, OR, USA, Oct. 2019, pp. 1–5. doi: 10.1109/ICSOS45490.2019.8978975.
[35] C. E. DeVoe *et al.*, "Optical overview and qualification of the LLCD space terminal," in *International Conference on Space Optics — ICSO 2014*, Nov. 2017, vol. 10563, p. 105630F. doi: 10.1117/12.2304194.
[36] K. E. Wilson, N. Page, J. Wu, and M. Srinivasan, "The JPL Optical Communications Telescope Laboratory Test Bed for the Future Optical Deep Space Network," p. 12.
[37] A. Biswas, S. Piazzolla, B. Moision, and D. Lisman, "Evaluation of deep-space laser communication under different mission scenarios," San Francisco, California, USA, Feb. 2012, p. 82460W. doi: 10.1117/12.913216.
[38] D. M. Cornwell, "NASA's optical communications program for 2015 and beyond," San Francisco, California, United States, Mar. 2015, p. 93540E. doi: 10.1117/12.2087132.
[39] Z. Sodnik *et al.*, "Results from a Lunar Laser Communication Experiment between NASA's LADEE Satellite and ESA's Optical Ground Station," presented at the International Conference on Space Optical Systems and Applications (ICSOS) 2014, Kobe, Japan, May 2014. Accessed: Nov. 01, 2021. [Online]. Available: http://www2.nict.go.jp/wireless/spacelab/lasersatellitetech/icsos/icsos2014/contents/program.html
[40] V. Kuroda, M. Allard, B. Lewis, and M. Lindsay, "Comm for Small Sats: The Lunar Atmosphere and Dust Environment Explorer (LADEE) Communications Subsystem," p. 11.
[41] R. Kingsbury, K. Riesing, and K. Cahoy, "Design of a Free-Space Optical Communication Module for Small Satellites," p. 10.
[42] A. Biswas, B. Oaida, K. S. Andrews, J. M. Kovalik, M. Abrahamson, and M. W. Wright, "Optical payload for lasercomm science (OPALS) link validation during operations from the ISS," in *Free-Space Laser Communication and Atmospheric Propagation XXVII*, Mar. 2015, vol. 9354, pp. 123–132. doi: 10.1117/12.2084964.
[43] T. S. Rose *et al.*, "Optical communications downlink from a 1.5U Cubesat: OCSD program," in *International Conference on Space Optics — ICSO 2018*, Chania, Greece, Jul. 2019, p. 18. doi: 10.1117/12.2535938.
[44] D. Rowen, B. Hardy, C. Coffman, D. Hinkley, R. Welle, and S. Janson, "The NASA Optical Communications and Sensor Demonstration Program: Proximity Operations," *32nd Annual AIAA/USU Conference on Small Satellites*, p. 7.
[45] S. Janson *et al.*, "The NASA Optical Communications and Sensor Demonstration Program: Initial Flight Results," p. 8.
[46] R. Morgan, "Nanosatellite Lasercom System," p. 9.
[47] L. S. Lingvay, A. P. Bowman, and A. S. Wallace, "Laser Payloads on Small Satellites," p. 10.
[48] S. Alluru and J. Y. McNair, "An Optical Payload for Cubesats," p. 13.
[49] B. Rödiger *et al.*, "High data-rate optical communication payload for CubeSats," in *Laser Communication and Propagation through the Atmosphere and Oceans IX*, Aug. 2020, vol. 11506, p. 1150604. doi: 10.1117/12.2567035.
[50] T. Tolker-Nielsen and G. Oppenhauser, "In-orbit test result of an operational optical intersatellite link between ARTEMIS and SPOT4, SILEX," in *Free-Space Laser*

Communication Technologies XIV, Apr. 2002, vol. 4635, pp. 1–15. doi: 10.1117/12.464105.
[51] T. Tolker-Nielsen and J.-C. Guillen, "SILEX: The First European Optical Communication Terminal in Orbit," p. 3.
[52] J. M. Perdigues *et al.*, "The ESA's optical ground station for the EDRS-A LCT in-orbit test campaign: upgrades and test results," in *International Conference on Space Optics — ICSO 2016*, Sep. 2017, vol. 10562, pp. 833–841. doi: 10.1117/12.2296098.
[53] R. Fields *et al.*, "5.625 Gbps bidirectional laser communications measurements between the NFIRE satellite and an Optical Ground Station," in *2011 International Conference on Space Optical Systems and Applications (ICSOS)*, May 2011, pp. 44–53. doi: 10.1109/ICSOS.2011.5783708.
[54] B. Gütlich, R. Meyer, S. Phillip-May, and A. Pagels-Kerp, "German Roadmap on Optical Communication in Space," in *Advanced Solid-State Lasers Congress*, Paris, 2013, p. LM1B.2. doi: 10.1364/LSC.2013.LM1B.2.
[55] I. Shurmer, F. Marchese, J.-M. Morales-Santiago, and P. P. Emanuelli, "Sentinels Optical Communications Payload (OCP) Operations: From Test to In-Flight Experience," presented at the 2018 SpaceOps Conference, Marseille, France, May 2018. doi: 10.2514/6.2018-2654.
[56] M. Witting *et al.*, "Status of the European Data Relay Satellite System," p. 8, 2012.
[57] B. Schlepp, R. Kahle, J. Saleppico, S. Kuhlmann, and U. Sterr, "Laser Communication with Alphasat - FD Challenges and First Flight Results," presented at the 24th International Symposium on Space Flight Dynamics (ISSFD), Laurel, MD, USA, May 2014. Accessed: Nov. 02, 2021. [Online]. Available: https://elib.dlr.de/89226/
[58] C. Fuchs and C. Schmidt, "Update on DLR's OSIRIS program," in *International Conference on Space Optics — ICSO 2018*, Jul. 2019, vol. 11180, p. 111800I. doi: 10.1117/12.2535937.
[59] C. Fuchs, F. Moll, D. Giggenbach, C. Schmidt, J. Keim, and S. Gaisser, "OSIRISv1 on Flying Laptop: Measurement Results and Outlook," in *2019 IEEE International Conference on Space Optical Systems and Applications (ICSOS)*, Portland, OR, USA, Oct. 2019, pp. 1–5. doi: 10.1109/ICSOS45490.2019.8978984.
[60] "IAA Study Group 4.18 Final Report: Definition and Requirements of Small Satellites Seeking Low-Cost and Fast-Delivery," Code ISBN/EAN IAA: 978-2-917761-59-5, Dec. 2017. Accessed: Oct. 24, 2021. [Online]. Available: https://iaaspace.org/wp-content/uploads/iaa/Scientific%20Activity/Study%20Groups/SG%20Commission%204/sg418/sg418finalreport.pdf
[61] P. Clark, "Cubesats in Cislunar Space," p. 7.
[62] Y. Kovo, "State of the Art of Small Spacecraft Technology," *NASA*, Mar. 06, 2020. http://www.nasa.gov/smallsat-institute/sst-soa (accessed Sep. 10, 2021).
[63] E. Clements, "State of the Art: Lasercom Systems Engineering and Challenges," p. 19.
[64] B. Rödiger, M.-T. Hahn, C. Fuchs, and C. Schmidt, "OSIRIS4CubeSat - System Engineering with new Space approach from the development of a high data-rate optical communication payload to the demonstrator in a quasi-operational mission," presented at the SECESA, the 9th International Systems & Concurrent Engineering for Space Applications Conference, Delft, Niederlande, Dec. 2020. Accessed: Sep. 11, 2021. [Online]. Available: https://elib.dlr.de/136602/
[65] C. Schieler *et al.*, "NASA's Terabyte Infrared Delivery (TBIRD) Program: Large-Volume Data Transfer from LEO," *Small Satellite Conference*, Aug. 2019, [Online]. Available: https://digitalcommons.usu.edu/smallsat/2019/all2019/107

[66] B. S. Robinson *et al.*, "TeraByte InfraRed Delivery (TBIRD): a demonstration of large-volume direct-to-Earth data transfer from low-Earth orbit," vol. 10524, p. 105240V, Feb. 2018, doi: 10.1117/12.2295023.
[67] A. U. Chaudhry and H. Yanikomeroglu, "Laser Intersatellite Links in a Starlink Constellation: A Classification and Analysis," *IEEE Veh. Technol. Mag.*, vol. 16, no. 2, pp. 48–56, Jun. 2021, doi: 10.1109/MVT.2021.3063706.
[68] "FITSAT." https://www.fit.ac.jp/~tanaka/fitsat.shtml (accessed Nov. 02, 2021).
[69] "An overview of optical communications for small satellites and CubeSats on the global marketplace," *satsearch blog*, Jan. 22, 2020. https://blog.satsearch.co/2020-01-22-optical-communications-for-small-satellites-and-cubesats-product-roundup (accessed Oct. 01, 2021).
[70] "AeroCube-OCSD - Satellite Missions - eoPortal Directory." https://directory.eoportal.org/web/eoportal/satellite-missions/a/aerocube-ocsd (accessed Nov. 02, 2021).
[71] "OPALS – Spaceflight101 – International Space Station." https://spaceflight101.com/iss/opals/ (accessed Nov. 02, 2021).
[72] C. Fuchs and C. Schmidt, "Update on DLR's OSIRIS program," in *International Conference on Space Optics — ICSO 2018*, Jul. 2019, vol. 11180, pp. 192–200. doi: 10.1117/12.2535937.
[73] "DLR – pioneering launch - compact satellite with terminal," *DLRARTICLE DLR Portal*. https://www.dlr.de/content/en/articles/news/2021/01/20210124_pioneering-launch-compact-satellite-with-smallest-laser-terminal.html (accessed Nov. 02, 2021).
[74] "AeroCube-OCSD-B and C - Satellite Missions - eoPortal Directory." https://eoportal.org/web/eoportal/satellite-missions/a/aerocubes-ocsd-b-and-c (accessed Nov. 02, 2021).
[75] "Optical Communication." https://www.esa.int/Applications/Telecommunications_Integrated_Applications/Alphasat/Optical_Communication (accessed Nov. 02, 2021).
[76] D. M. McIntosh, M. Field, D. M. McIntosh, J. D. Baker, J. D. Baker, and J. A. Matus, "The NASA Cubesat Missions Flying on Artemis," p. 11.
[77] M. M. Kobayashi, "Iris Deep-Space Transponder for SLS EM-1 CubeSat Missions," p. 9.
[78] J. C. Juarez, D. M. Brown, and D. W. Young, "Antenna gain of actively compensated free-space optical communication systems under strong turbulence conditions," *Opt. Express*, vol. 22, no. 10, p. 12551, May 2014, doi: 10.1364/OE.22.012551.
[79] T. Brummelaar, "Modeling atmospheric wave aberrations and astronomical instrumentation using the polynomials of Zernike," *Optics Communications*, vol. 132, no. 3–4, pp. 329–342, Dec. 1996, doi: 10.1016/0030-4018(96)00407-5.
[80] Robert J. Noll, "Zernike Polynomial and Atmospheric Turbulence," *J. Opt. Soc. Am.,* vol. 66, no. 3, 1976.
[81] H. Hemmati, A. Biswas, and I. B. Djordjevic, "Deep-Space Optical Communications: Future Perspectives and Applications," *Proc. IEEE*, vol. 99, no. 11, pp. 2020–2039, Nov. 2011, doi: 10.1109/JPROC.2011.2160609.
[82] A. Biswas and S. Piazzolla, "Deep-Space Optical Communications Downlink Budget from Mars: System Parameters," p. 38.
[83] Spectral Sciences, "MODTRAN®." http://modtran.spectral.com/modtran_home#plot (accessed Oct. 03, 2019).
[84] B. Moision and J. Hamkins, "Deep-Space Optical Communications Downlink Budget: Modulation and Coding," p. 28.

[85] B. Moision and H. Xie, "An Approximate Link Equation for the Direct-Detected Optical PPM Link," p. 14.
[86] T. Nguyen, K. Riesing, R. Kingsbury, and K. Cahoy, "Development of a pointing, acquisition, and tracking system for a CubeSat optical communication module," San Francisco, California, United States, Mar. 2015, p. 93540O. doi: 10.1117/12.2080591.
[87] H. Yoon, "Pointing System Performance Analysis for Optical Inter-satellite Communication on CubeSats," p. 181.
[88] K. M. Riesing, "Development of a Pointing, Acquisition, and Tracking System for a Nanosatellite Laser Communications Module," p. 127.
[89] C. Schmidt and J. Horwath, "Wide-Field-of-Regard Pointing, Acquisition and Tracking-System for small Laser Communication Terminals," p. 6, 2012.
[90] P. W. Young, L. M. Germann, and R. Nelson, "Pointing, Acquisition, And Tracking Subsystem For Space-Based Laser Communications," in *Optical Technologies for Communication Satellite Applications*, May 1986, vol. 0616, pp. 118–128. doi: 10.1117/12.961045.
[91] P. Grenfell, A. Aguilar, K. Cahoy, and M. Long, "Pointing, Acquisition, and Tracking for Small Satellite Laser Communications," *Small Satellite Conference*, Aug. 2018, [Online]. Available: https://digitalcommons.usu.edu/smallsat/2018/all2018/418
[92] J. Chang, C. M. Schieler, K. M. Riesing, J. W. Burnside, K. Aquino, and B. S. Robinson, "Body pointing, acquisition and tracking for small satellite laser communication," in *Free-Space Laser Communications XXXI*, San Francisco, United States, Mar. 2019, p. 23. doi: 10.1117/12.2511159.
[93] B. Epple, "Using a GPS-aided inertial system for coarse-pointing of free-space optical communication terminals," San Diego, California, USA, Aug. 2006, p. 630418. doi: 10.1117/12.680502.
[94] W. R. Leeb, "Laser Space Communications. Systems, Technologies, and Applications.: Systems, Technologies, and Applications," *rle*, vol. 28, no. 12, pp. 804–808, 2000, doi: 10.2184/lsj.28.804.
[95] H. Hemmati and J. M. Kovalik, "10-Gb/s Lasercom Terminal for Satellites," p. 7, 2012.
[96] D. Russell, H. Ansari, and C.-C. Chen, "Lasercom pointing, acquisition, and tracking control using a CCD-based tracker," in *Free-Space Laser Communication Technologies VI*, Aug. 1994, vol. 2123, pp. 294–303. doi: 10.1117/12.184655.
[97] T. C. Farrell, "The effect of atmospheric optical turbulence on laser communication systems: Part 2, practice," in *Sensors and Systems for Space Applications XII*, May 2019, vol. 11017, pp. 100–116. doi: 10.1117/12.2520059.
[98] R. L. Phillips, "Scintillation model for a satellite communication link at large zenith angles," *Opt. Eng*, vol. 39, no. 12, p. 3272, Dec. 2000, doi: 10.1117/1.1327839.
[99] J. H. Churnside, "Aperture averaging of optical scintillations in the turbulent atmosphere," *Appl. Opt., AO*, vol. 30, no. 15, pp. 1982–1994, May 1991, doi: 10.1364/AO.30.001982.
[100] J. Breidenthal and D. Abraham, "Design Reference Missions for Deep-Space Optical Communication," p. 19.
[101] D. Vicente, V. M, B. V, and S. I, "Design, Manufacturing & Qualification of 6U Deployable Solar Arrays for Deep Space Missions," presented at the 4th IAA Conference on University Satellite missions and Cubesat Workshop, Rome, Italy, Dec. 2017. [Online]. Available: https://www.gaussteam.com/wordpress/wp-content/uploads/2018/02/IAA-AAS-CU-17-09-09-VicenteDiaz.pdf
[102] "GOMspace | 6U Premium." https://gomspace.com/6u-premium.aspx (accessed Nov. 02, 2021).

[103] "GomSpace_Reference_Platforms_White_Paper_V42.pdf." Accessed: Nov. 02, 2021. [Online]. Available: https://gomspace.com/UserFiles/Customer%20Portal/White%20Papers/GomSpace_Reference_Platforms_White_Paper_V42.pdf

[104] J. P. Mason *et al.*, "MinXSS-2 CubeSat mission overview: Improvements from the successful MinXSS-1 mission," *Advances in Space Research*, Feb. 2019, doi: 10.1016/j.asr.2019.02.011.

[105] J. P. Mason *et al.*, "Miniature X-Ray Solar Spectrometer (MinXSS) –A Science-Oriented, University 3U CubeSat," p. 32.

[106] D. Hegel, "FlexCore: Low-Cost Attitude Determination and Control Enabling High-Performance Small Spacecraft," p. 8.

[107] H. Kaushal and G. Kaddoum, "Optical Communication in Space: Challenges and Mitigation Techniques," *IEEE Commun. Surv. Tutorials*, vol. 19, no. 1, pp. 57–96, 2017, doi: 10.1109/COMST.2016.2603518.

[108] M. M. Shumani, M. F. L. Abdullah, and A. Basahel, "Availability analysis of terrestrial free space optical (FSO) link using visibility data measured in tropical region," *Optik*, vol. 158, pp. 105–111, Apr. 2018, doi: 10.1016/j.ijleo.2017.11.203.

[109] "NICT / Space Communication Systems Laboratory / Satellite Laser Technology." https://www2.nict.go.jp/spacelab/hicali/lasersatellitetech/en/02center/center.html (accessed Nov. 02, 2021).

[110] "Cloud cover - Wikiwand." https://www.wikiwand.com/en/Cloud_cover (accessed Nov. 02, 2021).

[111] International Telecommunication Union, "Prediction methods required for the design of terrestial free-space optical links," Recommendation ITU-R P.1814, 2007. Accessed: Oct. 03, 2019. [Online]. Available: https://www.itu.int/dms_pubrec/itu-r/rec/p/R-REC-P.1814-0-200708-I!!PDF-E.pdf

[112] IOWA State University, *Automated Surface Observing System (ASOS)*. IOWA State University. [Online]. Available: http://mesonet.agron.iastate.edu/ASOS

[113] L. Li, L. Yuan, L. Wang, R. Zheng, Y. Wu, and X. Wang, "Recent advances in precision measurement & pointing control of spacecraft," *Chinese Journal of Aeronautics*, Jan. 2021, doi: 10.1016/j.cja.2020.11.018.

[114] C. J. Dennehy, "A Survey of Reaction Wheel Disturbance Modeling Approaches for Spacecraft Line-of-Sight Jitter Performance Analysis," *September*, p. 13, 2019.

[115] W. H. Semke and M. D. Dunlevy, "A Review of the Vibration Environment Onboard Small Unmanned Aircraft," in *Sensors and Instrumentation, Aircraft/Aerospace and Energy Harvesting , Volume 8*, Cham, 2019, pp. 155–164. doi: 10.1007/978-3-319-74642-5_18.

[116] J. Tian, W. Yang, Z. Peng, T. Tang, and Z. Li, "Application of MEMS Accelerometers and Gyroscopes in Fast Steering Mirror Control Systems," *Sensors*, vol. 16, no. 4, p. 440, Mar. 2016, doi: 10.3390/s16040440.

[117] H. Zhang, Y. Mao, J. Deng, and H. Liu, "Three Closed-Loop Feedback Control System with Dual Disturbance Observers of an Optoelectronic Stable Control Platform," *Electronics*, vol. 9, no. 2, p. 359, Feb. 2020, doi: 10.3390/electronics9020359.

[118] J. Sofka, V. V. Nikulin, V. A. Skormin, D. H. Hughes, and D. J. Legare, "Laser Communication Between Mobile Platforms," *IEEE Trans. Aerosp. Electron. Syst.*, vol. 45, no. 1, pp. 336–346, Jan. 2009, doi: 10.1109/TAES.2009.4805283.

[119] C. Deng, Y. Mao, and G. Ren, "MEMS Inertial Sensors-Based Multi-Loop Control Enhanced by Disturbance Observation and Compensation for Fast Steering Mirror System," *Sensors*, vol. 16, no. 11, p. 1920, Nov. 2016, doi: 10.3390/s16111920.

[120] B. Hou, "Charge-coupled devices combined with centroid algorithm for laser beam deviation measurements compared to a position-sensitive device," *Opt. Eng*, vol. 50, no. 3, p. 033603, Mar. 2011, doi: 10.1117/1.3554379.
[121] K. Cahoy *et al.*, "The CubeSat Laser Infrared CrosslinK Mission (CLICK)," in *International Conference on Space Optics — ICSO 2018*, Chania, Greece, Jul. 2019, p. 33. doi: 10.1117/12.2535953.
[122] G. Gunnison *et al.*, "Optical Communications Crosslink Payload Prototype Development for the Cubesat Laser Infrared CrosslinK (CLICK) Mission," p. 4.
[123] Z. Qingkun, B.-T. Pinhas, and F. Dapeng, "Design and Analysis of a Fast Steering Mirror for Precision Laser Beams Steering," *Sensors andTransducers*, vol. 5, no. Special, Mar. 2009, [Online]. Available: www.sensorsportal.com
[124] "Benefits of Photodiode Array Detection over conventional Scanning detection." https://lab-training.com/2015/07/13/benefits-of-photodiode-array-detection-over-conventional-scanning-detection/ (accessed Jun. 14, 2021).
[125] Q. Li, S. Xu, J. Yu, L. Yan, and Y. Huang, "An Improved Method for the Position Detection of a Quadrant Detector for Free Space Optical Communication," *Sensors*, vol. 19, no. 1, p. 175, Jan. 2019, doi: 10.3390/s19010175.
[126] "Scientific CCD camera, high frame rate." https://www.thorlabs.com/newgrouppage9.cfm?objectgroup_id=7485 (accessed Jun. 14, 2021).
[127] "Photodiode Sensor Physics." https://www.newport.com/n/photodiode-physics (accessed Jun. 14, 2021).
[128] A. Vyas, M. B. Roopashree, B. R. Prasad, and A. Vyas, "Performance of Centroiding Algorithms at Low Light Level Conditions in Adaptive Optics," in *2009 International Conference on Advances in Recent Technologies in Communication and Computing*, Kottayam, Kerala, India, 2009, pp. 366–369. doi: 10.1109/ARTCom.2009.30.
[129] M. Smith *et al.*, "On-Orbit Results and Lessons Learned from the ASTERIA Space Telescope Mission," p. 20.
[130] "ASTERIA - Satellite Missions - eoPortal Directory." https://directory.eoportal.org/web/eoportal/satellite-missions/a/asteria (accessed Sep. 29, 2021).
[131] G. Smet and S. Patti, "A Mechanisms Perspective on Microvibration – Good Practices and Lessons Learned," p. 14.
[132] V. A. Skormin, M. A. Tascillo, and D. J. Nicholson, "A jitter rejection technique in a satellite-based laser communication system," in *Proceedings of the IEEE 1993 National Aerospace and Electronics Conference-NAECON 1993*, Dayton, OH, USA, 1993, pp. 1107–1115. doi: 10.1109/NAECON.1993.290787.
[133] C. J. Dennehy, "A Survey of Reaction Wheel Disturbances Modelling Approaches for Spacecraft Line-of-Sight Jitter Performance Analysis," p. 13, Sep. 2019.
[134] J. Shields *et al.*, "Characterization of CubeSat Reaction Wheel Assemblies," *Journal of Small Satellites*, vol. 6, no. 1, pp. 565–580, 2017.
[135] R. A. (Rebecca A. Masterson, "Development and validation of empirical and analytical reaction wheel disturbance models," Thesis, Massachusetts Institute of Technology, 1999. Accessed: Sep. 29, 2021. [Online]. Available: https://dspace.mit.edu/handle/1721.1/80018
[136] D.-O. Lee, J.-S. Yoon, and J.-H. Han, "Development of Integrated Simulation Tool for Jitter Analysis," *International Journal of Aeronautical and Space Sciences*, vol. 13, no. 1, pp. 64–73, Mar. 2012, doi: 10.5139/IJASS.2012.13.1.64.

[137] EMIC Corporation, "EMIC Vibration Testsing System Manual." https://www.jistechsystems.com/downpdf/emic.PDF (accessed Sep. 25, 2021).